Robotic Motion Compensation for
3D Ultrasound-Guided Beating Heart Surgery

A dissertation presented

by

Shelten Gee Jao Yuen

to

The School of Engineering and Applied Sciences
in partial fulfillment of the requirements
for the degree of
Doctor of Philosophy
in the subject of

Engineering Sciences

Harvard University
Cambridge, Massachusetts
September 2009

Thesis advisor   Author

Robert D. Howe   **Shelten Gee Jao Yuen**

Robotic Motion Compensation for
3D Ultrasound-Guided Beating Heart Surgery

Abstract

Beating heart surgeries offer significant health benefits to patients by removing the need for the heart-lung machine and its attendant side effects. These surgeries are challenging to perform and only feasible in certain types of procedures because of the rapid movement of the heart. Equipping the surgeon with fast, actuated, and intelligent surgical instruments that automatically compensate for heart motion could facilitate the execution of existing beating heart procedures and enable the development of new procedures that are currently not possible. These tools have particular promise for intracardiac beating heart procedures, where passive tissue stabilization techniques are not available; however, achieving motion compensation in this setting is challenging because of the sensing and space restrictions imposed from working inside of the beating heart.

This thesis investigates 3D ultrasound-guided robotic motion compensation as an assistive technology to intracardiac beating heart surgery. A number of engineering challenges are addressed to develop a viable system for *in vivo* experimentation: heart motion prediction to counter time delays in 3D ultrasound imaging and image processing, real-time tracking of surgical targets in noisy 3D ultrasound images, and safe

iii

force control schemes for the manipulation of tissue without exciting vibratory modes in the robot. Solutions are provided in the form of a quasiperiodic extended Kalman filter, a synergistic "flashlight" tissue tracker, and a force controller with feed-forward target motion information, respectively. Integrating these components into a system, motion compensation within the beating heart is not only shown to be feasible under *in vivo* conditions, but also to provide significant performance advantages in beating heart tasks. Motion and force tracking accuracies of 1.0 mm and 0.11 N are obtained in *in vivo* surgical tasks with the system, constituting a 70% and 75% reduction in error when compared to human performance in the same tasks.

Contents

Acknowledgments

I am fortunate and honored to be surrounded by so many supportive, motivated, and brilliant people. This work would not have been possible without them and I would like to extend my heartfelt thanks for their help.

First and foremost I want to thank my advisor Professor Robert Howe. He has always pushed me toward the big problems while giving me the freedom to solve them in my own way. I could not have asked for or imagined a better guide through the Ph.D. process and I truly appreciate the time and effort that he spent teaching me. I also want to thank my committee members Dr. Pedro del Nido, Professor Pierre Dupont, and Professor Robert Wood for their insight and direction on this thesis from start to finish.

The members of the Biorobotics Lab have shared with me the joys and travails of graduate research. They have shaped my thinking and, without fail, given me those well-timed nudges of encouragement to keep me going. I give my thanks to Ryan Beasley, Aaron Dollar, Yuri Ishihara, Leif Jentoft, Amy Kerdok, Marius Linguraru, Masashi Nakatani, Riichiro Tadakuma, Mahdi Tavakoli, and Chris Wagner for their help throughout. The majority of my work was done in collaboration with members from the lab: Paul Novotny, Daniel Kettler, Samuel Kesner, Michael Yip, and Alex Dubec. It was a pleasure working with them and I am deeply grateful for their efforts and insights, without which I could not have achieved so much so quickly. Finally, I want to especially thank Petr Jordan, Peter Hammer, Douglas Perrin, and Robert Schneider for not only spending countless hours brainstorming with me, but also for their kind friendship.

I have had the privilege of working with the finest cardiac surgeons in the world

at Children's Hospital Boston. Dr. Pedro del Nido, Dr. Nikolay Vasilyev, and Dr. Mitsuhiro Kawata have all lended their time and immense medical expertise toward this thesis, to which I am thankful. In particular, Dr. Vasilyev performed all of the *in vivo* surgical experiments in this thesis and, in conjunction with Dr. Douglas Perrin, helped me to advance this project at every phase. I am indebted to both of them for their feedback, paper edits, and patience. I also want to thank Hugo Loyola for always being up to unwind over a cup of coffee with me while I worked at Children's.

I cannot stress enough the importance of my nurturing family: Allan Yuen, So San Aldridge, Stephen Aldridge, and Chris Yuen. They taught me how to think critically, work hard, live generously, and be happy. My accomplishments are a testament to their work in me.

Finally, I would like to thank my extraordinary wife Priscilla. She has contributed to every aspect of this thesis as an experimenter, test subject, and editor. I would not have survived and succeeded without her. I thank her for the wonderful gifts that she has given to me in unwavering love, support, and our beautiful daughter Elsie.

For Priscilla

Chapter 1

Introduction

Beating heart surgery is a promising and, in many cases, preferred alternative to conventional cardiac surgery. In this surgical approach, the surgeon operates on the heart while it pumps and, in doing so, circumvents many of the serious side effects for patients that occur as a result of stopping the heart and using the heart-lung machine. These side effects include increased risk of stroke [54], inflammatory response [8], and long-term neurocognitive dysfunction [43]. Beating heart procedures have shown a significant reduction of risk for these side effects [41], while also decreasing the postoperative recovery time in the hospital by 13% [3] and overall medical cost by 20–30% [41, 3]. Beating heart procedures also allow the surgeon to evaluate the surgery under physiologic loading conditions. This is useful in the repair of structures like the mitral valve that open and close in response to changing pressure gradients during the heart cycle [23].

The advantages of beating heart procedures are not obtained easily: surgical manipulation presents a significant challenge to the surgeon because cardiac motions

are too fast for humans to track by hand [18, 32]. As an example, the mitral valve annulus traverses most of its trajectory and undergoes three direction changes in about a tenth of a second [37], making it difficult for the surgeon to execute the precise surgical maneuvers required for tasks like mitral valve annuloplasty. Recent animal trials indicate that beating heart modification of the mitral valve cannot be performed reliably due to its fast motion [15].

For certain types of procedures, heart motion can be restrained with a passive mechanical stabilizer attached to the heart surface. This approach has enabled the widespread use of beating heart techniques in coronary artery bypass graft procedures (18% to 20% in the United States [41]). However, passive stabilization is an imperfect solution. Its use can damage the heart [64] and tissue constrained in this manner still exhibits significant residual motion [40]. Furthermore, stabilizers can only be used on the top surface of the heart and so are not applicable to many types of procedures, such as the broad category of those performed inside of the heart called intracardiac procedures.

The limitations of passive stabilization have inspired the development of active robotic tools that move with the heart. This is referred to as motion compensation. Current research shows a great deal of promise for this approach. In two controlled laboratory experiments, the use of a moving hand support [64] or an actuated, hand-held surgical instrument [37] increased accuracy by 80% and 50% (respectively) in simulated beating heart surgical tasks. Inside of the operating room, a robot has shown tracking accuracies on the order of 2 mm following the complex motion of the external heart wall [24]. A number of other studies have shown that heart motion can

be accurately predicted and followed by a robot *in vitro* [44, 62, 51, 6, 21, 5, 22, 4].

Previous research has focused on coronary artery bypass graft in order to improve an existing beating heart procedure. However, robotic motion compensation has the potential to act as an enabling technology for the development of new beating heart procedures that are not currently possible. It is of interest to determine if motion compensation can be achieved in the intracardiac setting, where passive stabilizers are not useful and there are stringent sensing and space restrictions. This thesis will show that motion compensation can be achieved inside the heart using standard 3D ultrasound imaging for guidance. Mitral valve annuloplasty is chosen as a specific surgical application for *in vivo* experimental validation because it is currently outside the reach of beating heart procedures. Furthermore, while previous research in motion compensation have achieved impressive position tracking results, there is no evidence that it affords any benefit to the surgeon in the operating room. This thesis will demonstrate that motion compensation enhances *in vivo* surgical task performance.

1.1   Mitral Valve Annuloplasty

The mitral valve (Figure 1.1) is a structure that is critical for the correct, uni-directional flow of oxygenated blood from the lungs to the body. An incompetent (i.e., leaky) valve can cause severe symptoms in the patient ranging from arrhythmia to heart failure. In the repair of an incompetent mitral valve, a synthetic ring is attached to the junction between the annulus and the atrial wall. This procedure, called mitral valve annuloplasty, attempts to reduce the annulus shape to that of the synthetic annuloplasty ring so that the leaflets meet properly.
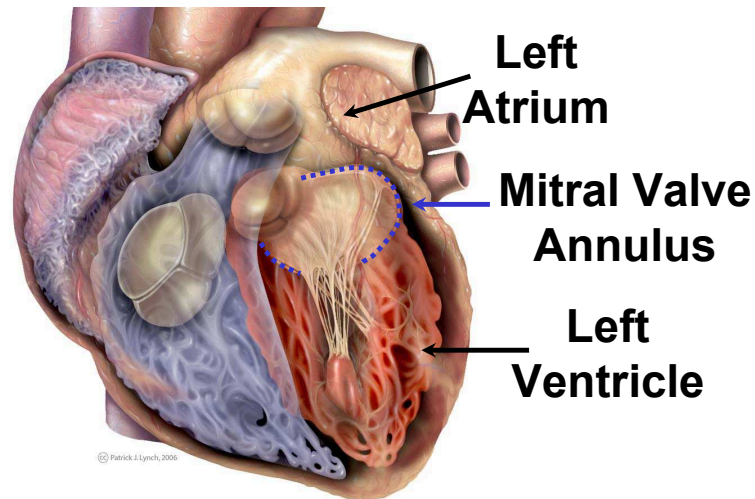
Figure 1.1: The mitral valve consists of an annulus surrounding two leaflets that are connected by chordae to the papillary muscles in the ventricle. (Image source: Patrick J. Lynch, medical illustrator; C. Carl Jaffe, MD, cardiologist)

Mitral valve annuloplasty is currently only performed on a stopped, open heart. This work considers a prototype surgical procedure that uses motion compensation for beating heart mitral valve annuloplasty (Figure 1.2). The procedure is a modification of a minimally-invasive beating heart procedure for the repair of atrial septal defects [65]. In the new procedure, the robotic instrument enters the heart from the left atrium and is actuated to compensate for annular motion. A custom annuloplastry ring is inserted through an adjacent incision and positioned over the annulus. The robotic instrument is tipped with an anchor deployment mechanism [68, 65, 66] that is used to attach the ring to the annulus.
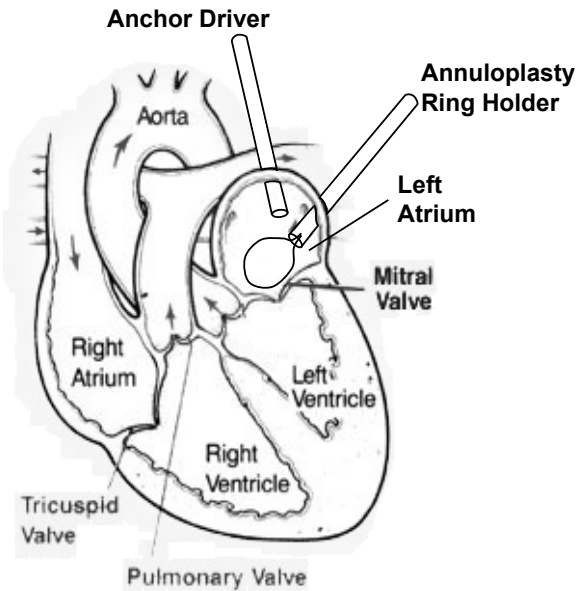
Figure 1.2: Prototype beating heart mitral valve annuloplasty procedure using robotic motion compensation instrumentation.

1.2   3D Ultrasound Guidance

A major consideration for intracardiac robot control is how the robot will be guided. The motion compensation system in this work uses 3D ultrasound imaging because it is capable of imaging through blood and it provides more spatial information to guide complex intracardiac procedures than traditional 2D ultrasound [10]. While other imaging modalities like 3D computed tomography and magnetic resonance imaging offer higher spatial resolution, they have prohibitively slow imaging speeds, require special facilities, incur high costs, and cannot be moved into the operating room. In contrast, 3D ultrasound is relatively cheap, portable, and operates in real-time (24–30 Hz). 3D ultrasound is also becoming the preferred imaging technology among cardiac surgeons for guiding intracardiac beating heart repairs [61, 60, 65, 66] and it is advantageous to use it in the system to reduce training.

Despite its advantages, there are a number of difficulties associated with using 3D ultrasound for robotic motion compensation. It has high noise, poor shape definition, and imaging artifacts that can distort the appearance of tissues and instruments [30]. Novotny *et al.* found that accurate, real-time instrument tracking could be achieved *in vivo* by exploiting the high spatial coherence of surgical instruments in 3D ultrasound [48]. Subsequently, a robot could be visually servoed to mimic heart motion *in vitro*, although with a large 130 ms temporal lag that is unacceptable for *in vivo* motion compensation [46]. The lag was attributed to delays in the acquisition, transfer, and processing of 3D ultrasound volumes as well as robot latency [46].

This previous research indicates that a number of interesting and unsolved problems must be addressed to use 3D ultrasound for robot guidance. Methods are required to automatically track *in vivo* surgical targets in noisy 3D ultrasound while compensating for the time delays present in both the imaging and the robot. In this work, solutions are provided to address these problems.

1.3   System Concept

The 3D ultrasound-guided motion compensation system proposed in this work partners the medical expertise of the surgeon with the speed of a robot to augment the capabilities of the surgeon in beating heart procedures. Figure 1.3 illustrates the general system concept. The surgeon holds a robotic instrument, navigates it to the surgical site, and designates the surgical target by pointing the instrument tip toward it. A set of automated algorithms determine the position of the surgical target in 3D ultrasound and are used to command the robot. Because the robot utilizes the
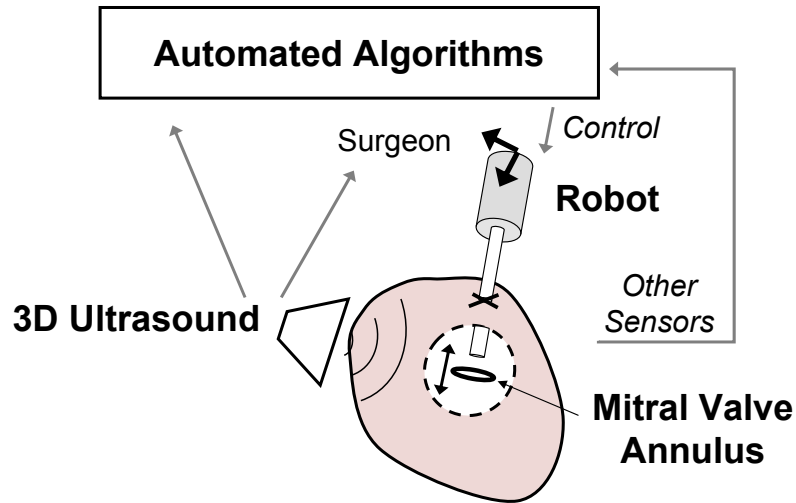
Figure 1.3: The motion compensation system consists of an actuated, handheld instrument that is controlled by a set of automated algorithms to respond to heart motion. The algorithms take input from 3D ultrasound and possibly other sensors. The surgeon views the procedure through a 3D ultrasound rendering.

judgement of the surgeon for targeting and the surgeon likewise relies on the robot to compensate for heart motion, the system may be classified as synergistic [14]. This approach places the motion compensation capabilities in the instruments that are typically used by the surgeon and should be distinguished from the teleoperation concept proposed in other work [44, 24, 51, 6].

Previous work used positional controllers to make a robot maintain a fixed distance away from the heart [44, 62, 24, 6]. A limitation of this work is that it has not yet shown that a robot can safely contact and manipulate moving heart tissue *in vivo*. When in contact, a force controller is more appropriate because any position mismatch between the robot and tissue could lead to large forces. The system developed in this work uses positional control, force control, and the combination of both in order to demonstrate *in vivo* intracardiac position tracking and contact tasks.

1.4   Thesis Contributions

This thesis demonstrates for the first time the *in vivo* feasibility and performance advantages of robotic motion compensation for intracardiac beating heart surgical tasks. To do this, a 3D ultrasound-guided robotic motion compensation system is developed. The system incorporates the robot design of Kettler *et al.* [37] and real-time 3D ultrasound instrument tracking algorithm of Novotny *et al.* [48].

There are several interesting challenges to overcome in the development of the system. The time delays and noise inherent to 3D ultrasound [46] must be addressed for the real-time guidance of a robot *in vivo*. Furthermore, the structural dynamics of the robot are an obstacle to safe control when in contact with moving tissue. This work provides solutions to these challenges by drawing on methods from the fields of estimation, image processing, and control. The major technological contributions are the development of a predictive heart motion filtering method to mitigate noise and time delay in 3D ultrasound; the development of a synergistic approach to real-time 3D ultrasound tissue tracking for *in vivo* robot guidance; and the development of a robotic force tracking system that incorporates feed-forward motion information for beating heart tissue manipulation.

1.5   Thesis Outline

This thesis is presented as a set of successive technology advancements that are needed to realize a 3D ultrasound-guided motion compensation system.

Chapter 2 addresses the challenge of accurately estimating heart motion to servo

a robotic instrument when provided noisy, time-delayed positional information by 3D ultrasound. This chapter proposes the use of an extended Kalman filter that explicitly models heart rate variability and sensor noise to increase estimate accuracy. This method is shown to provide more accurate estimates than existing techniques through computer simulation and *in vitro* experiments. Subsequent user testing in an *in vitro* surgical task demonstrates that the extended Kalman filter restores the performance benefits of motion compensation that are lost when there is uncompensated time delay.

Chapter 3 introduces a novel, real-time 3D ultrasound tissue tracking algorithm adapted for cardiac structures that undergo primarily uniaxial motion. The mitral valve annulus is an example of such a structure [37]. The algorithm is robust to imaging noise because it draws on the high spatial coherence of the instrument in 3D ultrasound to locate the tissue target. Integrating this algorithm with the filter from Chapter 2 results in a motion tracking system suitable for mitral valve annuloplasty. *In vitro* and *in vivo* experiments with this system demonstrate the positioning accuracy and task performance enhancement conferred in beating heart procedures.

Chapter 4 solves the problem of applying precise forces against a fast-moving cardiac target during surgical manipulation by incorporating a force controller into the system. Analysis and experiments are presented to show that current surgical instruments impose stringent bandwidth limitations that preclude accurate force tracking with a standard force controller. A feed-forward force control strategy is proposed that incorporates the motion filtering and tracking algorithms from Chapters 2 and 3. The resulting system is validated under *in vivo* conditions and shown to significantly

reduce force fluctuations when compared to manual attempts to maintain a constant force against the mitral valve annulus.

Chapter 5 discusses the implications of this research on motion compensation and intracardiac beating heart surgery. While the technologies developed in this work focus on mitral valve annuloplasty, they have wider applicability to other procedures both inside and outside of the heart. Future enhancements to the work are also outlined.

Chapter 2

Time Delay Compensation

Real-time 3D ultrasound is an effective imaging technology for surgical guidance within the beating heart. Cannon *et al.* demonstrated that the increased spatial information provided by 3D ultrasound enables the execution of complex tasks that are not possible with traditional 2D ultrasound [10] and recently surgeons have shown that 3D ultrasound can be used to guide the closure of atrial septal defects [61, 60, 65] and ventricular septal defects [66] in the beating heart. These studies suggest that 3D ultrasound is a good candidate for guiding a motion compensation system for beating heart surgery, both because it has the speed, fidelity, and spatial information to guide surgery on moving cardiac structures and because it is currently used by and familiar to surgeons. However, there are delays of approximately 60 ms inherent to using 3D ultrasound that can cause a motion compensation system to lag behind fast-moving heart structures [46] – in effect, not compensating for heart motion at all.

Latency is intrinsic to every robotic system and can arise from a number of sources. One fundamental source is inertia: regardless of how fast the robot moves, it takes

finite time to respond to a commanded input. When the inertia of the robot is large relative to its actuation capabilities, the associated latency will be large. This has been one of the main challenges addressed in previous research in extracardiac motion compensation for coronary artery bypass graft procedures, where relatively large, multiple degree of freedom (DOF) robots track the external surface of the heart wall [24, 6]. In that work, researchers exploited the nearly periodic motion of the heart to feed-forward a trajectory into a model predictive controller so that the effective tracking bandwidth of the robot was increased. Ginhoux *et al.* first showed that this strategy could achieve robot tracking errors of approximately 1.5 mm on a beating porcine heart using a high speed camera to observe heart motion (500 Hz sampling rate, 330 μm accuracy) and then predicting heart motion into the near future with an adaptive harmonic filter bank [24]. In independent work, Bebek and Cavusoglu demonstrated less than 1 mm robot tracking error by using ECG and the previous heart cycle trajectory to predict motion in the next heart cycle [6]. Their system used sonomicrometry sensors sutured to the surface of a porcine heart, sampling at 257 Hz with 250 μm position accuracy. These studies indicate that the predictability of heart motion can be used to overcome system latency when fast, high accuracy sensors are employed for guidance.

In this chapter, we show that a similar approach can be used to overcome delays in a 3D ultrasound-guided motion compensation system where the delays are primarily due to imaging. There are several new aspects to the problem of heart motion prediction in this setting. Unlike the sensors used in the previous work, 3D ultrasound has a relatively low sampling rate (24–30 Hz), low resolution (approximately
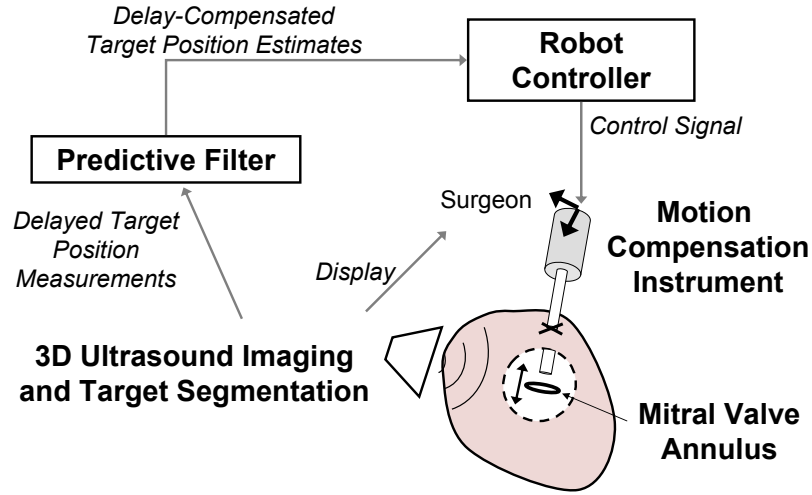
Figure 2.1: Motion compensation system. Time-delayed position measurements of the target are provided to a filter which uses prediction to compensate for delay. These are fed-forward to the controller of the one DOF motion compensation instrument to synchronize with the target motion. The surgeon holds the instrument and navigates its end effector to the target using 3D ultrasound imaging.

0.5 mm), and high noise that makes the overall surgical target localization accuracy on the order of 1 mm. In order to mitigate the disadvantages of 3D ultrasound, we propose the use of an extended Kalman filter (EKF) that explicitly models noise and quasiperiodic heart motion in order to achieve accurate target trajectory predictions. The filter feeds-forward the trajectory of the cardiac target to a robot controller to obtain accurate motion synchronization despite time delay. A small, fast, one DOF robot is used to reduce the time delay that occurs from inertia. The resulting system is illustrated in Figure 2.1. The surgeon can use this system in procedures where the motion of the cardiac tissue is largely in a single direction. As will be shown shortly, this includes the motion of the mitral valve annulus.

In the following, we first characterize the motion of the mitral valve annulus to determine the tracking performance requirements of a motion compensation system

for mitral valve annuloplasty. Next, we describe the actuated, one DOF robot that we term the motion compensation instrument. We then describe the EKF and several other predictive filtering methods and compare them in simulation. Two subsequent user studies evaluate the benefit of a motion compensation system against traditional non-tracking tools in a simulated *in vitro* surgical task. Furthermore, they validate the robustness that the EKF provides to the system in situations of high noise, time delay, and heart rate variability. Finally, we measure the position tracking accuracy of the system in a series of 3D ultrasound-guided motion synchronization experiments. The mitral valve annulus motion, motion compensation instrument, and first user study were first described in [37] and are included in this chapter for clarity and completeness.

2.1 Mitral Valve Annulus Motion

To guide the development of a motion compensation system for mitral valve annuloplasty, the motion of the mitral valve annulus was analyzed using ultrasound image data like that available in surgery for real-time guidance. A transthoracic 3D ultrasound image-volume sequence of the mitral valve annulus was acquired at 24 Hz (SONOS 7500, Philips Healthcare, Andover, MA, USA). This raw 3D ultrasound data was manually segmented to extract mitral valve annulus trajectory information. For each 3D volume sample, a minimum of 50 data points were selected from the mitral valve annulus and used to locate the annulus centroid. Repeated for each time-stamped data frame, this process generated a record of the annulus centroid position over the cycle of the heartbeat. Because this manual segmentation process
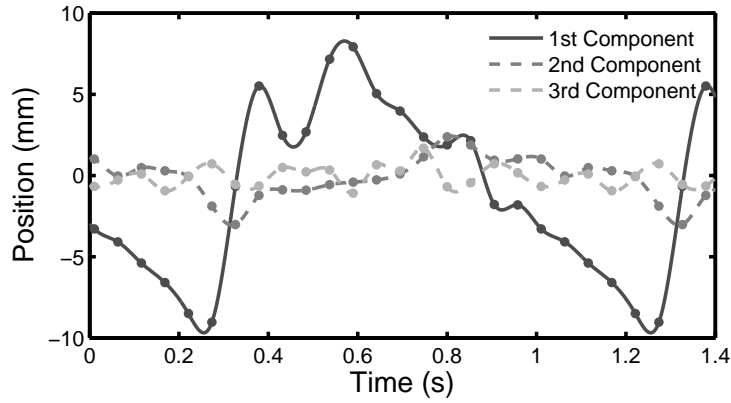
Figure 2.2: Orthogonal views of 3D ultrasound tracking data centroid positions plotted in principal component axes. Note the dominance of motion in the first component.

was extremely labor intensive, data from only two patients were analyzed.

In order to specify hardware design constraints for the motion compensation instrument, position, velocity, and acceleration along the major axis of the valve's motion were extracted from this data. Using singular value decomposition (SVD), a line was fit to each data set. The relative sizes of the singular value associated with each orthonormal basis vector generated by SVD (i.e., 21.75, 5.49, 2.97) suggest that the motion of the annulus is strongly constrained to a principal axis (Figure 2.2). Furthermore, working with sheep, Gorman *et al.* found that the that rotational movements around this primary axis are negligible [26]. Subsequent analysis presented here will therefore focus on the component of motion along the primary axis.

Velocity and acceleration were estimated by considering the relative motion between 3D ultrasound data samples. This method provided mitral valve annulus velocity and acceleration maxima of 210 mm/s and 3.8 m/s^2, respectively, with a total travel of approximately 20 mm at a heart rate of 76 beats per minute (bpm). While
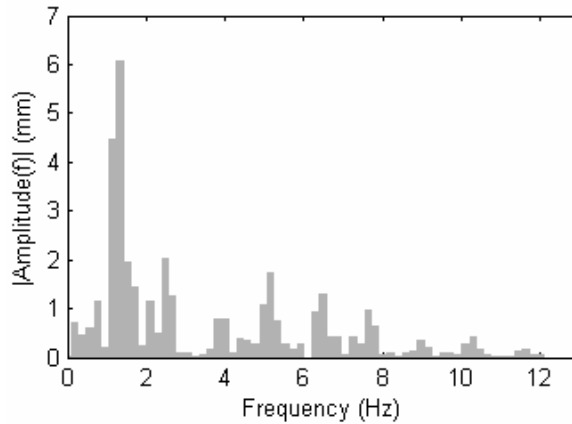
Figure 2.3: 3D ultrasound tracking data spectral decomposition. Note that the amplitudes quickly decrease with increasing frequency.

only two subjects were analyzed in this fashion, work by Kamigaki and Goldschlager on the mitral valve leaflets reports similar velocity and amplitude results [35].

Figure 2.3 shows the spectral decomposition of the major axis motion trajectory. The dominant motion components are at 1.3, 2.6, and 5.2 Hz, with further components of decreasing amplitude at higher frequencies. This is consistent with the findings of Nakamura *et al.* which show dominant frequency components of 1.5 Hz and 3.0 Hz in the motion of porcine epicardium [44]. Ginhoux *et al.* found the same major frequency components in the motion of porcine epicardium [24]. This paper also noted higher frequency transients that it deemed significant and concluded that a 25 Hz sampling rate would be insufficient to track the motion of the epicardium with high precision [24]. Bebek and Cavusoglu found similar frequency components, but concluded that the motion could be adequately characterized using lower sampling frequencies (i.e., 26 Hz) [6].

2.2   Motion Compensation Instrument

Prior work on beating heart motion compensation has largely focused on the use of multiple DOF teleoperated manipulators for extracardiac procedures. Implementing a full six DOF robot for intracardiac applications has a number of challenges, including the development of a manipulator with sufficient mechanical bandwidth, creating a wrist that can operate in the restricted workspace within the beating heart, and ensuring safety for a complex manipulator system. These requirements are far beyond the capabilities of current commercial surgical robots.

Rather than attempting to correct for motion components in all three dimensions, we propose a robot that compensates for the major component of motion and allows the surgeon and passive tissue compliance to counter the slow or relatively minor motions along the remaining two axes. The robot, called the motion compensation instrument (MCI), is an actuated, handheld instrument that aids the surgeon in working on the moving mitral valve. It is adapted for the prototype procedure described in Chapter 1. The instrument is inserted through the left atrial appendage and aimed toward the mitral valve annulus, which is also along the major motion axis of the annulus (Figure 1.2).

The selection of the mechanical mechanism to follow the linear motion component of the mitral valve annulus was guided by the clinical 3D ultrasound trajectory analysis from Section 2.1. The high velocity and acceleration requirements lead to a linear motor based design which benefits from low friction and low moving mass (Figure 2.4). This design format also produces a surgical tool similar in design and function to typical endoscopic tools, supported by a port and maneuvered by hand.
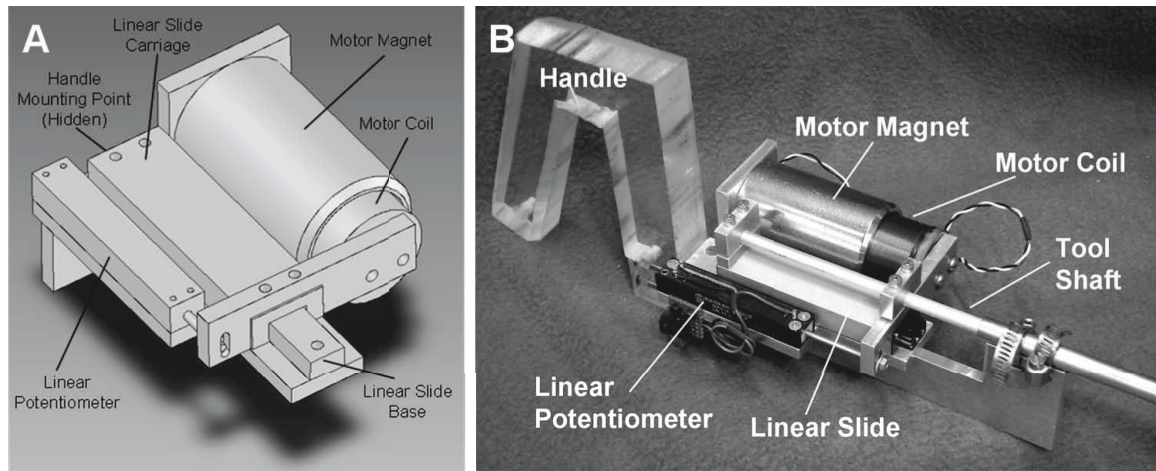
Figure 2.4: MCI design and prototype. A: MCI actuation package. The MCI may be mounted by its base (at the upper left of the image) to a robot or handle. The surgical anchor driver is mounted on the linear slide carriage. B: MCI hardware prototype.

Consequently, the MCI will be intuitive to operate for trained endoscopic surgeons.

The MCI uses a voice coil motor (NCC20-18-020-1X, H2W Technologies, Inc., Valencia, CA, USA) and a high linearity potentiometer (P3 America, San Diego, CA, USA) for position sensing. These components are mounted on a linear ball-bearing stage (BX4-3, Tusk Direct, Inc., Bethel, CT, USA). The MCI prototype has a 5.4 cm range of motion and is powered by a linear power amplifier (BTA-28V-6A, Precision MicroDynamics, Victoria, BC, Canada). PID servo control is implemented in a 1 kHz servo loop on a personal computer under Windows XP. The MCI is interfaced to this computer through a data acquisition card (PCI-60-40E, National Instruments, Corp., Austin, TX, USA).

The resulting system meets the requirements for tracking the mitral valve annulus. The MCI can attain velocities and accelerations as high as 290 mm/s and 17.5 m/s^2 respectively. Controller gains were hand tuned to achieve good stiffness and response. To avoid potentially dangerous overshoot and instability, the system is overdamped.
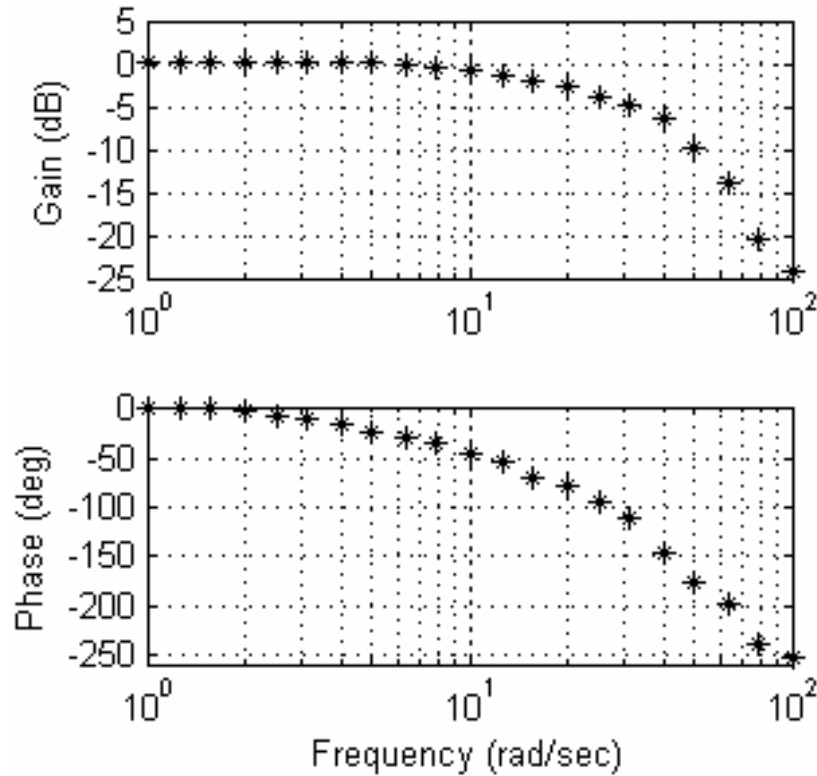
Figure 2.5: Frequency response of the MCI. Note that the system is overdamped and has a -3 dB point of 20.6 Hz.

The tool has a static stiffness of 0.23 N/mm and a friction force less than 0.009 N. The system's frequency response is similarly adequate for the tracking task (Figure 2.5). The system has a -3 dB point of 20.6 Hz and roll off rate of 40 dB per decade. The potentiometer on the MCI measures position with a root mean square (RMS) error of less than 0.01 mm. The system is capable of maintaining stationary at a commanded position with a RMS error of 0.009 mm.

  The tracking abilities of the MCI were demonstrated by commanding the system to follow the motion of a mitral valve at 60 bpm (Figure 2.6). Mitral annulus motion was determined from the 3D ultrasound data in Figure 2.2. The MCI reliably replicated the motion profile of the valve with an effective delay of 14 ms.
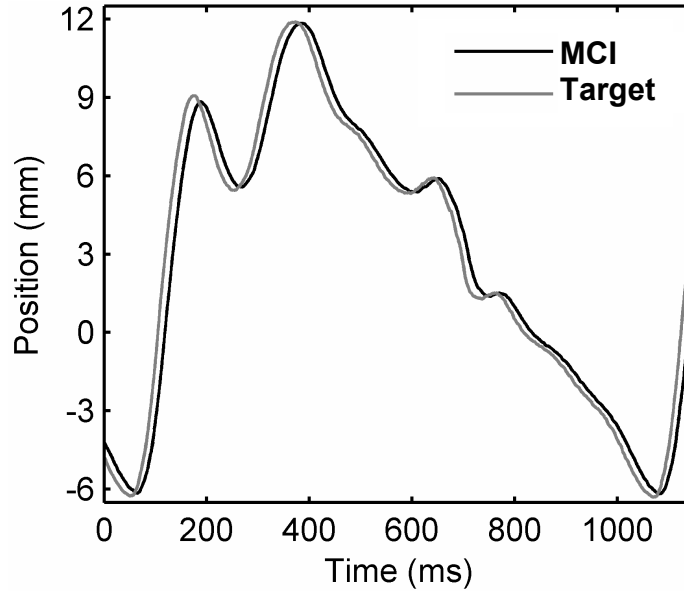
Figure 2.6: The MCI tracking a simulated mitral valve annulus trajectory. Note that the MCI motion profile closely mimics that of the target with a 14 ms delay due to the response time of the robot.

2.3   Heart Motion Prediction

The time delay that is intrinsic to 3D ultrasound makes direct servoing of the MCI from this signal potentially dangerous. A previous characterization of the acquisition, transmission, and computation times for 3D ultrasound estimated delays of approximately 70 ms, a sufficient amount of time for the mitral valve annulus to cover most of its trajectory because of high frequency components in the motion [46]. For the purposes of illustration, an example of the error for the MCI tracking a mitral valve annulus target with a 75 ms measurement delay is shown in Figure 2.7. The rapid recoil of the valve associated with ventricular relaxation (100–200 ms in Figure 2.7) results in a large 14 mm tracking error that could cause the instrument to collide with and damage the tissue target.
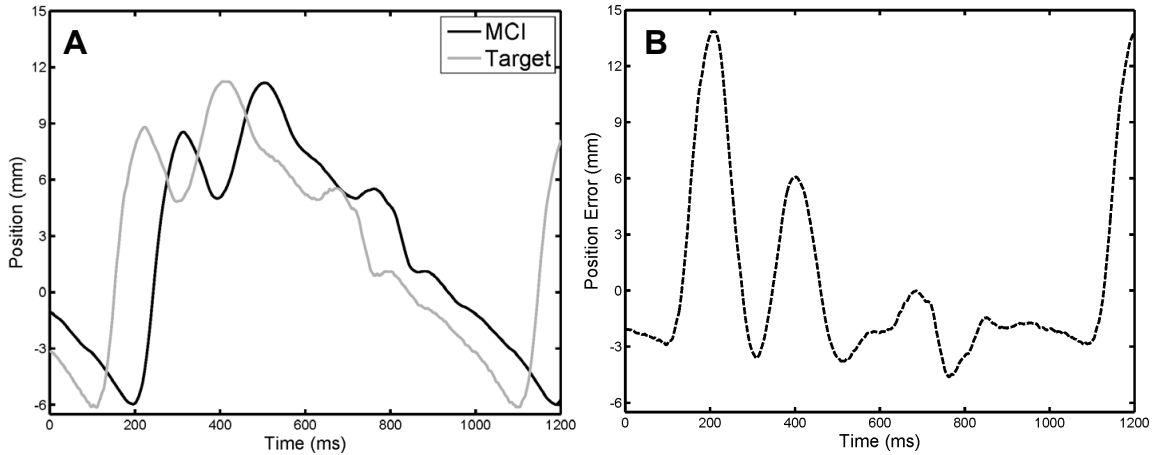
Figure 2.7: MCI tracking of a mitral valve target with 75 ms measurement delay from 3D ultrasound imaging and processing. A: MCI and target positions; B: Tracking error. Note that the additional 14 ms response time of the MCI yields an effective delay of 89 ms. Max and RMS tracking errors are 14.49 and 4.60 mm, respectively.

2.3.1 Predictive Filters

To avoid this outcome, we exploit the near periodicity of the mitral valve annulus trajectory to predict its path and hence compensate for time delay. However, such predictions must be made in the presence of measurement noise and a potentially variable heart rate. In this section we describe and evaluate several predictive filtering methods that can be employed for delay compensation in this setting: an autoregressive filter, a fading memory autoregressive filter, and an extended Kalman filter (EKF) with a quasiperiodic motion model. The autoregressive filter has previously been applied by Nakamura *et al.* in a spectral analysis of heart motion for motion compensation in coronary artery bypass graft (CABG) procedures [44]. In principle, this method is equivalent to the adaptive harmonic filter bank used by Ginhoux *et al.* for CABG [24] and has its attendant assumption of a fixed heart rate. The fading memory autoregressive filter overcomes this limitation despite using the

same model by exponentially discounting the measurements supplied to the filter, thereby allowing it to adjust to more recent information. This approach has been used for motion synchronization in CABG by Franke *et al.* [21]. In contrast, the EKF permits variations to heart rate by directly accounting for it in a time-varying Fourier series model. A similar model was employed by Riviere *et al.* in the Weighted Fourier Linear Combiner (WFLC) estimator for CABG [53]; however, unlike the EKF, this method does not explictly model noise. Ortmaier *et al.* has evaluated other nonlinear prediction techniques for CABG such as artificial neural networks and an estimator based on Takens theorem [51].

Autoregressive Filter

Fixed-rate mitral valve annulus motion can be modeled as an n-order autoregressive (AR) process

$$y[k] = \sum_{i=1}^{n} \alpha_i y[k-i], \tag{2.1}$$

where α_i, $i \in \{1, ..., n\}$ are the model coefficients and $y[k]$ is the target position at time sample k. Note that rather than explicitly assuming periodicity in the target motion, this model predicates that the kth position can be expressed as a linear combination of the previous n positions.

In order to predict the target position, the model coefficients and order must be estimated. The first can be achieved in real-time using the recursive covariance method estimator. Denoting $z[k] = y[k] + \nu[k]$ to be the noise-corrupted position measurement at time sample k with $\nu[k] \sim \mathcal{N}(0, \sigma_R^2)$, this estimator is expressed

compactly in matrix form as

$$\boldsymbol{Z}[k] = [z[k-n-1], \ldots, z[k-1]]$$

$$\boldsymbol{R}[k] = \boldsymbol{R}[k-1] + \boldsymbol{Z}[k]^{\mathrm{T}}\boldsymbol{Z}[k] \tag{2.2}$$

$$\hat{\boldsymbol{\alpha}}[k] = \hat{\boldsymbol{\alpha}}[k-1] + \boldsymbol{R}[k]^{-1}\boldsymbol{Z}[k]^{\mathrm{T}}\left(z[k] - \boldsymbol{Z}\hat{\boldsymbol{\alpha}}[k-1]\right), \tag{2.3}$$

with initial conditions $\boldsymbol{R}[0] = \boldsymbol{0}$ and $\hat{\boldsymbol{\alpha}}[0] = 0$. An appropriate autoregressive model order was determined using the Akaike Information Criteria [11] on the mitral valve annulus trajectory in Figure 2.2, yielding $n = 30$. Predicted target locations, $\hat{y}[k]$, can be obtained through evaluation of Equation 2.1. Additionally, the target trajectory can be interpolated from its inherent measurement rate (i.e., 28 Hz, a typical 3D ultrasound frame rate) to the higher control rate of the robot using the Whittaker-Shannon interpolation formula.

Fading Autoregressive Filter

Imperfect periodicity can cause the AR model coefficients to change over time. In this situation, it can be useful to preferentially weight recent measurements over those in the past – otherwise the filter becomes progressively less responsive to new data and Equation 2.3 does not update the filter coefficients $\hat{\boldsymbol{\alpha}}$ because $\boldsymbol{R}[k]^{-1}\boldsymbol{Z}^{\mathrm{T}} \to \boldsymbol{0}$ as $k \to \infty$. Exponential weighting of previous measurements in the iterative least squares estimator is achieved through modification of Equation 2.2:

$$\boldsymbol{R}[k] = f\boldsymbol{R}[k-1] + \boldsymbol{Z}[k]^{\mathrm{T}}\boldsymbol{Z}[k],$$

where $0 < f \leq 1$ is the so-called *fading* factor. Choosing $f = 1$ recovers the estimator of Section 2.3.1 while choosing $f \to 0$ increases the speed by which previous

measurements are discounted. To distinguish between the two estimators, we term the former the *AR filter* and the latter the *Fading AR filter*. Reducing the contribution of previous measurements ($f < 1$) can be desirable if the trajectory evolves through time; though doing so incurs increased estimate error when the trajectory is not time-varying.

Quasiperiodic Extended Kalman Filter

The spectral analysis of mitral valve annulus motion from Section 2.1 suggests that its motion may be approximated by a limited number of harmonics. Consider a perfectly periodic motion model obtained by an m-order Fourier series with a constant offset

$$y(t) = c + \sum_{i=1}^{m} r_i \sin(i\omega t + \phi_i), \tag{2.4}$$

where $y(t)$ is the position in ultrasound coordinates, ω is the heart rate, c is the constant offset, and r_i and ϕ_i are respectively the harmonic amplitudes and phases. Accurate modeling of quasiperiodicity requires a more flexible model in which the heart rate and signal morphology can evolve over time. Using the parameterization from [52], the trajectory can be expressed as the following time-varying Fourier series

$$y(t) = c(t) + \sum_{i=1}^{m} r_i(t) \sin \theta_i(t), \tag{2.5}$$

where $\theta_i(t) = i \int_0^t \omega(\tau) d\tau + \phi_i(t)$ and all other parameters are the time-varying equivalents to those in Equation 2.4.

Defining the state vector $\boldsymbol{x}(t) \triangleq [c(t), r_i(t), \omega(t), \theta_i(t)]^{\mathrm{T}}$, $i \in (1, \ldots, m)$ and assuming that $c(t), r_i(t), \omega(t)$, and $\phi_i(t)$ evolve through a random walk, the state space

model for this system is

$$\boldsymbol{x}(t + \Delta t) = \boldsymbol{F}(\Delta t)\boldsymbol{x}(t) + \boldsymbol{\mu}(t)$$

$$z(t) = h(\boldsymbol{x}(t)) + \nu(t),$$

where

$$\boldsymbol{F}(\Delta t) = \begin{bmatrix} \boldsymbol{I}_{m+1} & & & & & \boldsymbol{0} \\ & 1 & & & & \\ & \Delta t & 1 & & & \\ \boldsymbol{0} & 2\Delta t & 0 & 1 & & \\ & \vdots & & & \ddots & \\ & m\Delta t & & & & 1 \end{bmatrix},$$

$h(\boldsymbol{x}(t)) \triangleq y(t)$ from Equation 2.5, $\nu(t)$ is zero mean Gaussian measurement noise with variance σ_R^2, and $\boldsymbol{\mu}(t)$ is the random step of the states assumed to be drawn from a zero mean multivariate normal distribution with covariance matrix $\boldsymbol{Q}$.

Prediction with this model requires estimation of the $2m + 2$ parameters in $\boldsymbol{x}(t)$, which is a nonlinear estimation problem owing to the measurement function $h(\boldsymbol{x}(t))$. We employ the EKF, a nonlinear filtering method that approximates the Kalman filter through linearization about the current state estimate $\hat{\boldsymbol{x}}(t|t)$. The EKF can be computed in real-time using the recursion

$$\boldsymbol{P}(t + \Delta t|t) = \boldsymbol{F}\boldsymbol{P}(t|t)\boldsymbol{F}^{\mathrm{T}} + \boldsymbol{Q}$$

$$S = \sigma_R^2 + \boldsymbol{H}\boldsymbol{P}(t + \Delta t|t)\boldsymbol{H}^{\mathrm{T}}$$

$$\boldsymbol{K} = \boldsymbol{P}(t + \Delta t|t)\boldsymbol{H}^{\mathrm{T}}S^{-1}$$

$$\hat{\boldsymbol{x}}(t + \Delta t|t + \Delta t) = \boldsymbol{F}\hat{\boldsymbol{x}}(t|t) + \boldsymbol{K}(z(t + \Delta t) - h(\boldsymbol{F}\hat{\boldsymbol{x}}(t|t)))$$

$$\boldsymbol{P}(t + \Delta t|t + \Delta t) = (\boldsymbol{I} - \boldsymbol{K}\boldsymbol{H})\boldsymbol{P}(t + \Delta t|t),$$

where

$$\boldsymbol{H}^{\mathrm{T}} \triangleq \left(\frac{\partial h}{\partial \boldsymbol{x}}\right)^{\mathrm{T}}\Bigg|_{\hat{\boldsymbol{x}}(t+\Delta t|t)=\boldsymbol{F}\hat{\boldsymbol{x}}(t|t)} = \begin{bmatrix} 1 \\ \sin\hat{\theta}_1(t+\Delta t|t) \\ \vdots \\ \sin\hat{\theta}_m(t+\Delta t|t) \\ 0 \\ \hat{r}_1(t+\Delta t|t)\cos\hat{\theta}_1(t+\Delta t|t) \\ \vdots \\ \hat{r}_m(t+\Delta t|t)\cos\hat{\theta}_m(t+\Delta t|t) \end{bmatrix},$$

and $\boldsymbol{P}(\cdot) \triangleq E\left[\hat{\boldsymbol{x}}(\cdot)\hat{\boldsymbol{x}}(\cdot)^{\mathrm{T}}\right]$ denotes the state estimate covariance, whose initialization is described later in this section. Note that the time dependencies of $\boldsymbol{F}$, $\boldsymbol{K}$, S, and $\boldsymbol{H}$ have been dropped for notational convenience. The EKF as presented here is a slight variant on the one first introduced by Parker and Anderson [52].

To initialize this filter, we first assume that $y(t)$ has constant fundamental frequency yielding N noisy measurements over the interval $[0, N\Delta t]$. Observation of Figure 2.3 indicates that the dominant frequency peak is the fundamental frequency of the signal (i.e., heart rate). We apply an FFT to the data sequence with a Hamming window to obtain the power spectrum. The maximum frequency peak within a reasonable human heart rate range (0.5 to 2.5 Hz) is used to initialize the estimate of $\hat{\omega}_0 \triangleq \omega(t = N\Delta t)$.

Assuming $\hat{\omega}_0$ to be correct, the problem can be rewritten as a linear estimation problem to obtain the harmonic amplitudes and coefficients. Equation 2.4 is equivalently reparameterized as

$$y(t) = c_0 + \sum_{i=1}^{m} \left[a_i \sin(i\hat{\omega}_0 t) + b_i \cos(i\hat{\omega}_0 t)\right]. \tag{2.6}$$

Collecting the measurements $z(t)$, $t \in \{0, \Delta t, \ldots, (N-1)\Delta t\}$ we have $\tilde{\boldsymbol{z}} = \boldsymbol{A}\tilde{\boldsymbol{x}}_0 + \boldsymbol{\nu}$, where $\tilde{\boldsymbol{z}} \triangleq [z(0), z(\Delta t), \ldots, z((N-1)\Delta t)]^{\mathrm{T}}$, $\tilde{\boldsymbol{x}}_0 \triangleq [c_0, a_1, \ldots, a_m, b_1, \ldots, b_m]^{\mathrm{T}}$, $\boldsymbol{\nu}$ is a vector of measurement noise, and

$$\boldsymbol{A}^{\mathrm{T}} \triangleq \begin{bmatrix} 1 & 1 & \ldots & 1 \\ \sin(\hat{\omega}_0 0) & \sin(\hat{\omega}_0 \Delta t) & \ldots & sin(\hat{\omega}_0(N-1)\Delta t) \\ \vdots & \vdots & & \vdots \\ \sin(m\hat{\omega}_0 0) & \sin(m\hat{\omega}_0 \Delta t) & \ldots & sin(m\hat{\omega}_0(N-1)\Delta t) \\ \cos(\hat{\omega}_0 0) & \cos(\hat{\omega}_0 \Delta t) & \ldots & cos(\hat{\omega}_0(N-1)\Delta t) \\ \vdots & \vdots & & \vdots \\ \cos(m\hat{\omega}_0 0) & \cos(m\hat{\omega}_0 \Delta t) & \ldots & cos(m\hat{\omega}_0(N-1)\Delta t) \end{bmatrix},$$

to which the least squares estimate is obtained as $\hat{\tilde{\boldsymbol{x}}}_0 = (\boldsymbol{A}^T\boldsymbol{A})^{-1}\boldsymbol{A}^T\tilde{\boldsymbol{z}}$. $\hat{\boldsymbol{x}}(T|T)$ is then initialized with the values $\hat{c}(T) = \hat{c}_0$, $\hat{\omega}(T) = \hat{\omega}_0$, $\hat{r}_i(T) = (\hat{a}_i^2 + \hat{b}_i^2)^{-1/2}$, and $\hat{\theta}_i(T) = \arctan(\hat{b}_i, \hat{a}_i)$. The state estimate covariance is set to

$$\boldsymbol{P}(T|T) = \mathrm{diag}\left[\sigma_R^2/N, \sigma_1^2, \sigma_1^2/2^2, \ldots, \sigma_1^2/m^2, \sigma_\omega^2, 0.02 \text{ rad}^2, \ldots, 0.02 \text{ rad}^2\right].$$

The relationship between the amplitude uncertainties is chosen to reflect the decreasing harmonic strength seen in Figure 2.3, while the phase uncertainties follow those used in [52]. Parameters σ_1^2 and σ_ω^2 are determined through experimentation. Last, we assume that the process noise covariance $\boldsymbol{Q}$ is diagonal with all values set to 10^{-4} except for q_ω, the entry corresponding to $\omega(t)$.

2.3.2 Simulation Studies

Three simulation studies were conducted to evaluate the capabilities of the EKF, AR filter, and Fading AR filter to the primary sources of random error in the system:
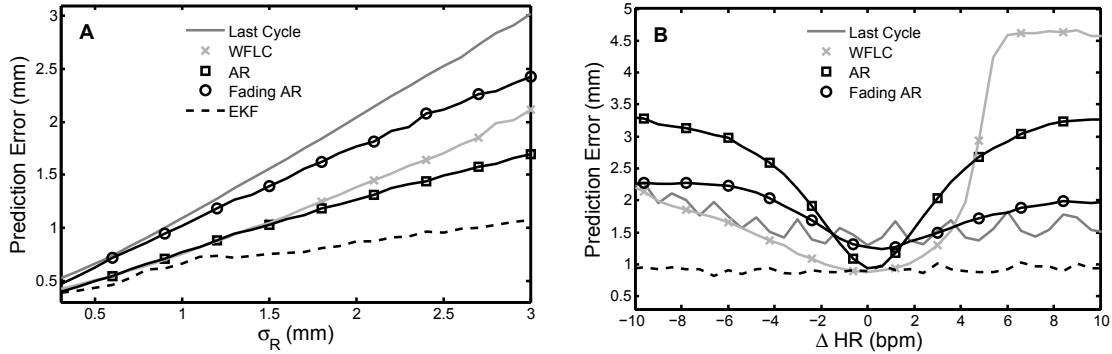
Figure 2.8: RMS prediction error results for parametric simulation studies. A: Error for varying measurement noise; B: Error for step heart rate changes.

measurement noise and heart rate variability. For illustrative purposes, the filters were also compared to the WFLC estimator [53] and a simpler method of using the previous cardiac cycle trajectory for the prediction of the next. A more sophisticated version of the latter method, termed *Last Cycle* here, was used successfully in a beating heart tracking system [6].

In the first simulation, we subjected the predictors to varying levels of measurement noise on a fixed-rate trajectory (60 bpm). The mitral valve annulus trajectory of Figure 2.2 was reinterpolated to 28 Hz and corrupted by additive zero-mean Gaussian noise with standard deviation $0.3 \leq \sigma_R \leq 3$ mm. Each predictor was then given 30 s of data to initialize and performance was judged for the following 10 s on 1-sample ahead predictions.

The RMS errors for each predictor averaged across 100 monte-carlo trials are shown in Figure 2.8A. The EKF, WFLC, AR, and Fading AR filtering methods clearly give higher accuracy predictions than the inherent uncertainty of the measurements, with the EKF doing the best. As expected, the Last Cycle method had error statistics equal to σ_R since it attempts no smoothing. It should be noted that the Fading AR

filter was tuned with $f = 0.985$ in order to achieve errors that are approximately equal to σ_R. This setting represents the lowest reasonable value for the Fading AR filter since a value lower would give performance below the Last Cycle method. The EKF was run with $m = 8$ harmonics, $N = 280$ initialization points (10 s), $\sigma_1^2 = 2$ mm^2, $\sigma_\omega^2 = 0.11$ (rad/sec)^2 (roughly twice the frequency resolution of the FFT), and $q_\omega = 10^{-3}$ (rad/sec)^2. The WFLC was initialized in the same manner as the EKF, run with $m = 8$ harmonics, and experimentally set with its adaptive gain parameters $\mu_0 = 7 \times 10^{-6}$ and $\mu_1 = 0.03$ for best performance in this and subsequent simulations.

In a second parametric simulation study, we gauged the tolerance of each predictor to a sudden change in heart rate. A trajectory was assembled by piecing together 30 s of heart motion at 60 bpm and 10 s of motion at $(60+\Delta\text{HR})$ bpm. The second portion of the trajectory was generated by compression/dilation of the target trajectory in Figure 2.2 to obtain the desired heart rate. Like before, the composite trajectory was reinterpolated to 28 Hz and corrupted with additive, Gaussian, zero-mean noise with $\sigma_R = 1.30$ mm. The last 10 s were used to evaluate performance. A reasonable range of -10 bpm $\leq \Delta\text{HR} \leq 10$ bpm was determined from clinical heart rate data (Figure 2.9), which is discussed in more detail later in this section.

Figure 2.8B shows the mean RMS errors for each predictor across 100 monte-carlo trials. The EKF provided better predictions than the other four methods. It was also the only method that yielded sub-σ_R error for the majority of heart rate changes. The WFLC had similar accuracies to the EKF at small ΔHR but showed slow convergence to the new heart rate for $\Delta\text{HR} > 4$ bpm. As expected, the accuracy of the AR filter also approached that of the EKF for small ΔHR and quickly degraded

as ΔHR increased. Exponential weighting of the measurements allowed the filter to adjust to changes in the trajectory, as demonstrated by the Fading AR filter's superior performance over the AR filter for large ΔHR. However, this adaptability lessened accuracy when the trajectory did not change significantly. Finally, the Last Cycle method showed performance comparable to the Fading AR filter. For this simulation all filter parameters were chosen the same as in the previous simulation, with the exception of $q_\omega = 5 \times 10^{-3}$ (rad/s)^2 and $\sigma_\omega^2 = 1$ (rad/s)^2 for the EKF.

Finally, to investigate the performance of each predictor to the more realistic case of a continuously changing heart rate, we modulated the period of the annulus trajectory with clinically-obtained cardiac cycle records. Annotated ECG records for five human subjects were selected from the MIT-BIH Normal Sinus Rhythm Database [25] and composite mitral valve annulus trajectories were generated in a manner similar to the previous simulation study. Noise-corrupted measurements were generated as before, with $\sigma_R = 1.30$ mm. Summary statistics for each subject are presented in Figure 2.9B and an example of the beat-to-beat heart rate for subject number 1 is shown in Figure 2.9C.

Results from this study indicate that the EKF is more suited to tracking and prediction in this application than the other four methods because it adjusts to rapid changes in heart rate through explicit modeling of quasiperiodicity (Figure 2.10). Interestingly, the AR filter showed moderately better performance than the Fading AR filter. The reason for this is that the AR filter locked on to an "average" trajectory for each subject while the Fading AR filter continuously readjusted to more recent noisy data. Ultimately, deviations from the "average" motion were less than the
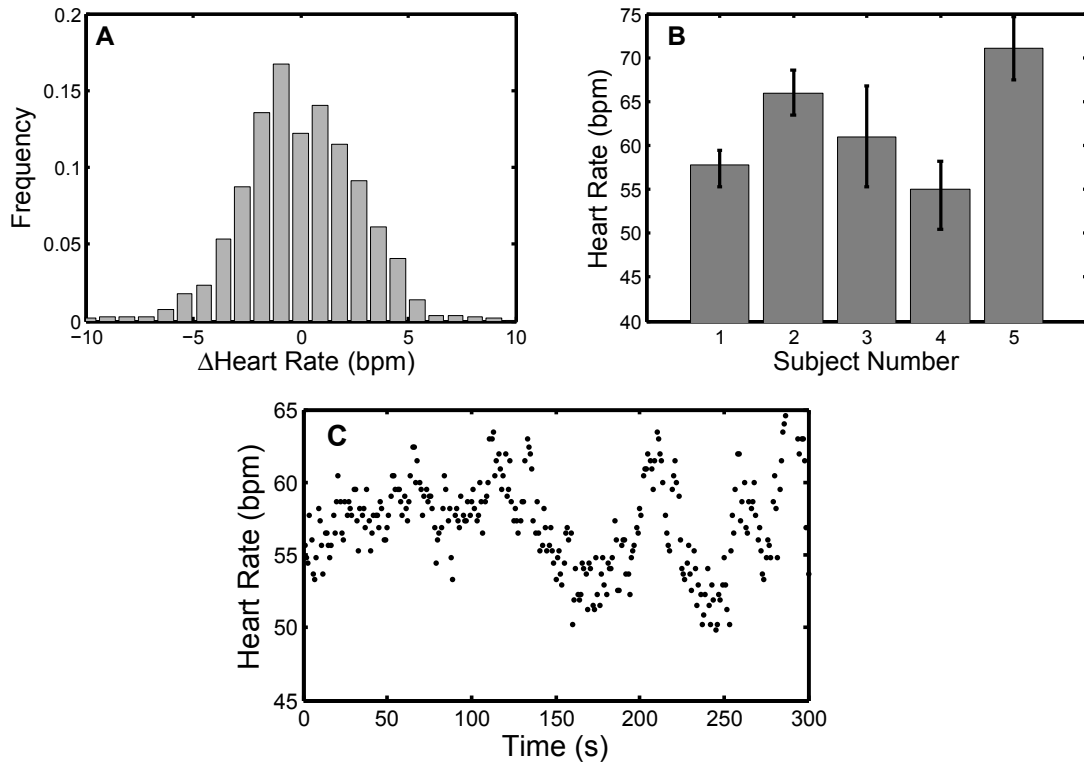
Figure 2.9: Heart rate statistics on five human subjects. A: Distribution of beat-to-beat variation; B: Subject-specific mean $\pm$ one standard deviation; C: Heart rate data for subject 1.
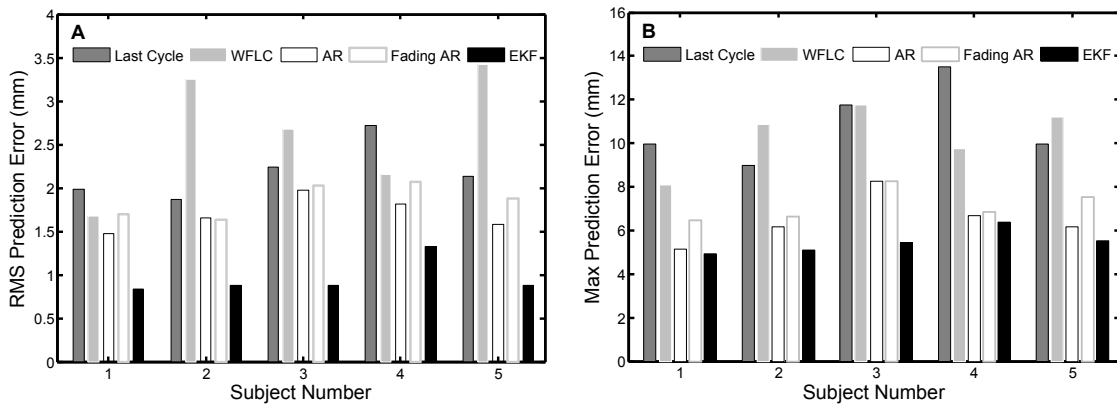

Figure 2.10: Comparison of prediction error results on clinical data using Last Cycle, WFLC, AR filter, Fading AR filter, and EKF. A: RMS error; B: Maximum absolute error.

measurement noise. The Last Cycle method performed worse for similar reasons: persistent variations in heart rate and measurement noise degraded the accuracy of the previous cycle as a predictor for the next. The slow convergence of the WFLC to changing heart rates caused it to have severely degraded performance.

2.4 Performance Evaluation in a Surgical Task

In order to quantify the amount of assistance that motion compensation provides to operators working on a moving target, we conducted two studies of user performance with the MCI in an *in vitro* setting. These studies additionally provide insight on how sensitive performance is to the shortcomings of a 3D ultrasound-guided system. Specifically, User Study 1 determined the extent to which user performance is dependent on time delay and random positional error. User Study 2 investigated user performance with EKF delay compensation on targets with both fixed and variable heart rates. Subjects performed a drawing task on a moving target using the MCI under different tracking conditions. A total of eighteen test subjects (fourteen male and four female, aged 22 to 36; eight subjects for User Study 1 and ten subjects for User Study 2) voluntarily participated following informed consent under a protocol approved by the University Institutional Review Board.

2.4.1 Experimental Setup

The tests were run on a setup that emulates the intended surgical environment. To simulate the moving mitral valve, a target platform was mounted on a cam-driven device that replicates the 1D motion of the mitral valve annulus centroid as measured

from the 3D ultrasound tracking data. During trials, a paper target was affixed to this platform to record the subject's drawing. A 0.5 cm hard foam rubber pad between the target paper and target platform provided a small measure of compliance. In combination with the pen used in the trials, the pad had a stiffness of 4.5 N/mm. For the purposes of this experiment, the cam was used to simulate a heart rate of 60 bpm. Opposite the target platform, the MCI was mounted in a gimbal allowing both angular motion and translation towards and away from the target (Figure 2.11). A rod was mounted on the MCI with a ballpoint pen affixed to one end and a force sensor incorporated along its length. The force sensor had a stiffness of 10 N/mm. In place of the 3D ultrasound-based tracking and controls algorithms that would be used in surgery, target position was directly measured at 1 kHz by a contact arm with a potentiometer attached to the target platform. This sensing method provided the robust tracking data necessary to evaluate the efficacy of MCI mitral valve annulus tracking and the performance of predictive filtering algorithms.

2.4.2   User Task

Subjects were instructed to draw a circle on the moving target platform. The circle had to be drawn between two concentric target circles with 2.29 cm and 2.92 cm diameters. Subjects started at the top of the circle and proceeded in the clockwise direction. If the pen bounced off of the target surface or outside of the target circles, the subject was instructed to continue drawing from the clockwise-most mark that they made between the target circles. Subjects could only draw around the circle once. They could not go back to draw in gaps that they originally missed. To
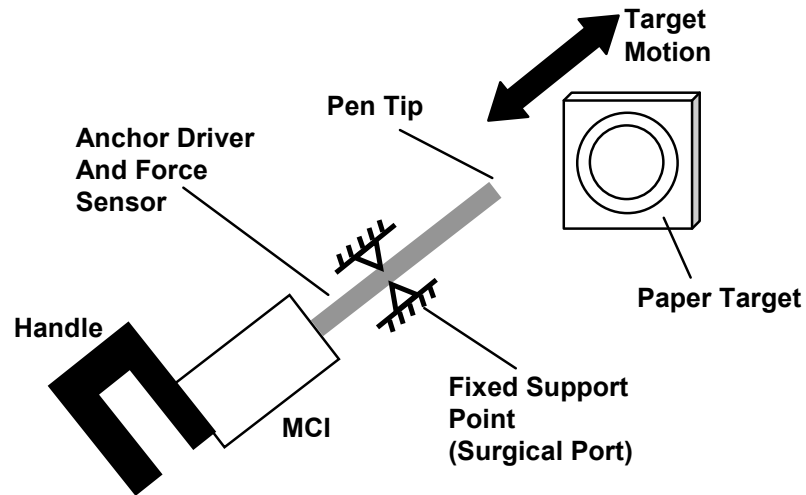
Figure 2.11: User trial setup. The bold arrow indicates the cyclical motion of the simulated valve target. The tool shaft has free rotational and sliding motion at the fixed support point.

prevent subjects from spending an inordinate amount of time on the task, a 25 s time limit was set. All subjects finished every trial before the time expired.

Both dexterity and force metrics were used to evaluate subject performance. In all trials, the quality of each circle drawn was characterized by digitally scanning the target and computing the drawn line's "angular surround" value. This value indicates what percentage of 360 discrete 1° arc segments the user's line covered between the two concentric target circles. This metric reflects positioning accuracy both in the plane of the target and in tracking the motion of the target perpendicular to this plane. If the user-drawn line strayed from the concentric target circles, it did not contribute to the angular surround metric and resulted in a lower score. Similarly, if the user and MCI were unable to track the motion of the target, the pen tended to bounce off of the target surface, producing widely spaced marks and a low angular surround score.

The axial force applied by the subject to the target was also recorded for four of the eight test subjects in User Study 1 and nine of the ten subjects in User Study 2. In all eighteen cases, subjects were informed of both evaluation metrics. They were instructed that their foremost objective was to draw continuous circles conforming to the angular surround metric and only secondly to use the minimum amount of force necessary.

This task was selected to emulate the motion requirements of placing a surgical anchor. In order to apply the surgical anchors developed for this procedure, the tip of the anchor driver, consisting of 14 gauge hypodermic tubing, must be accurately located and pressed against the target surface with a force of at least 1.5 N [68]. This contact must be maintained for several seconds as the surgeon inserts the anchor, tests whether it is properly deployed, and then releases the anchor. This process requires a combination of accuracy and prolonged contact with the surface. At the same time, forces must be minimized so as not to cause damage to the valve.

2.4.3 Independent Variables

User Study 1: Tracking with Time Delay and Positional Error

Subjects of User Study 1 completed the task in eight different tracking conditions. In the "solid" condition, the motion of the MCI was rigidly locked in order to simulate a traditional, solid endoscopic tool. For the "baseline" MCI tracking condition, the current position of the target (0.015 mm RMS error) was sent to the MCI as a position command. This baseline condition resulted in a 14 ms delay. The remaining six tracking conditions were divided into two groups of three conditions corresponding

to differing levels of the considered error.

Random positional error was simulated by the superposition of a time-varying error value with the cam position command used in the baseline tracking state. A new positional error was calculated at 8 Hz. These errors were uniformly distributed random values ($[-1, 1]$), multiplied by an amplitude factor of 0.35 mm, 0.70 mm, or 1.05 mm.

Delay error was implemented by recording the cam tracking position and holding it for a specified period before sending this position to the MCI as a motion command. For this set of trials, the three levels of added delay used were 25 ms, 35 ms, and 45 ms. Including the MCI lag time of 14 ms, the effective delay settings were 39 ms, 49 ms, and 59 ms. This range of times was chosen as representative of the imaging and transmission delays associated with real-time 3D ultrasound-guided procedures [48].

User Study 2: Delay-Compensated Tracking with Heart Rate Variation and Measurement Noise

To test the EKF under conditions similar to those seen in 3D ultrasound-guided procedures, the 1 kHz measurements of target position were downsampled to 28 Hz and corrupted by additive, zero-mean Gaussian noise with variance 1.30^2 [46]. The target was commanded to beat at 60 bpm or with a variable rate that had additive, zero-mean Gaussian beat-to-beat fluctuations with variance σ_{HR}^2. Finally, a time delay of 39 ms, 59 ms, or 89 ms was injected into the measurements to simulate the delays encountered with 3D ultrasound. Note that the 89 ms delay exceeds the delays used in User Study 1 to also account for the additional computational delays from
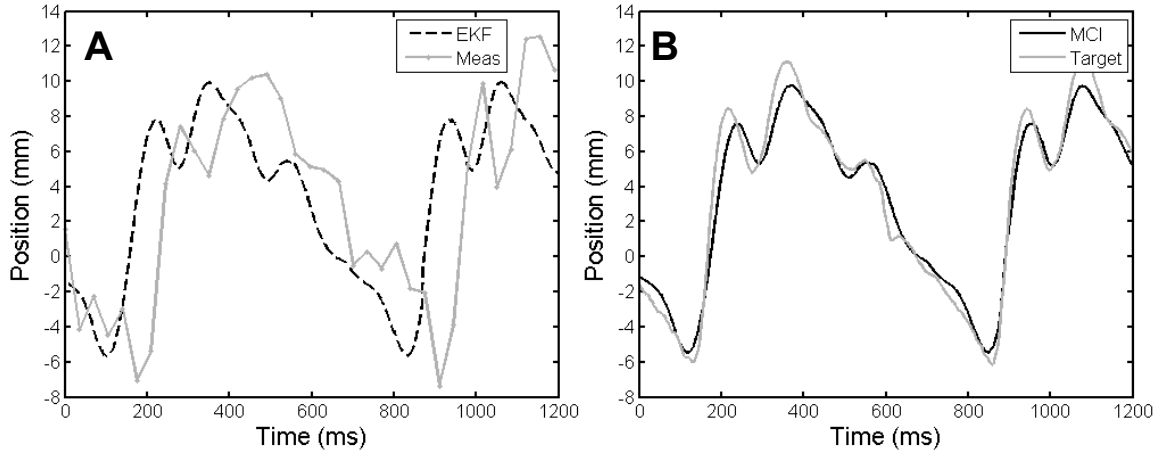
Figure 2.12: Variable heart rate tracking condition ($\sigma_{HR} = 4.0$). A: Noise-corrupted, time-delayed measurements and the resulting EKF predictions; B: MCI position and the true position of the target.

instrument and target segmentation in 3D ultrasound [46].

Overall, the subjects of this study performed the task in ten tracking conditions, all with varying amounts of time delay. Three tracking conditions evaluated user performance with EKF delay compensation against 39 ms, 59 ms, and 89 ms time-delayed, noise-corrupted measurements on a 60 bpm target. For comparison, three tracking conditions were conducted on the same set of delays but without delay compensation and without measurement noise.

The remaining four tracking conditions evaluated user performance with EKF delay compensation on a variable heart rate target. Measurements were delayed by 89 ms and noise-corrupted. The four levels of beat-to-beat variation were chosen as $\sigma_{HR} \in \{1.0, 2.0, 3.0, 4.0\}$ bpm. These values span those observed in the clinical heart rate data from Section 2.3.2. An illustrative example of this tracking condition with $\sigma_{HR} = 4.0$ bpm and the subsequent behavior of the EKF and the MCI is shown in Figure 2.12.

2.4.4   Testing Protocol

Each subject test consisted of a practice period followed by the trials corresponding to the tracking conditions of their study. Practice was intended to familiarize the test subject with the MCI and the evaluation task in order to bring subjects to a uniform level of ability and to limit learning effects during trials. Practice was divided into three one-minute segments during which the subject was free to experiment with using the MCI to draw on a target paper. During the first minute of training, the target was stationary and the tool was set in the solid condition. The second minute of training involved a moving target and a solid tool. In the third and final minute, the target was moving and the MCI was in the baseline tracking condition. Following the completion of training, each test subject ran through the trials corresponding to the tracking conditions of their study. The order in which these conditions were administered was varied between trials using a balanced Latin square to minimize the effects of between-trial carry-over and learning on collected data.

The means of collected angular surround error metric were compared for statistically significant differences using the SPSS statistical analysis software package (Version 14.0, SPSS Inc., Chicago, IL, USA). These comparisons were made using t-tests and ANOVA with an LSD post hoc test. In all cases, significance corresponds to $p < 0.05$.
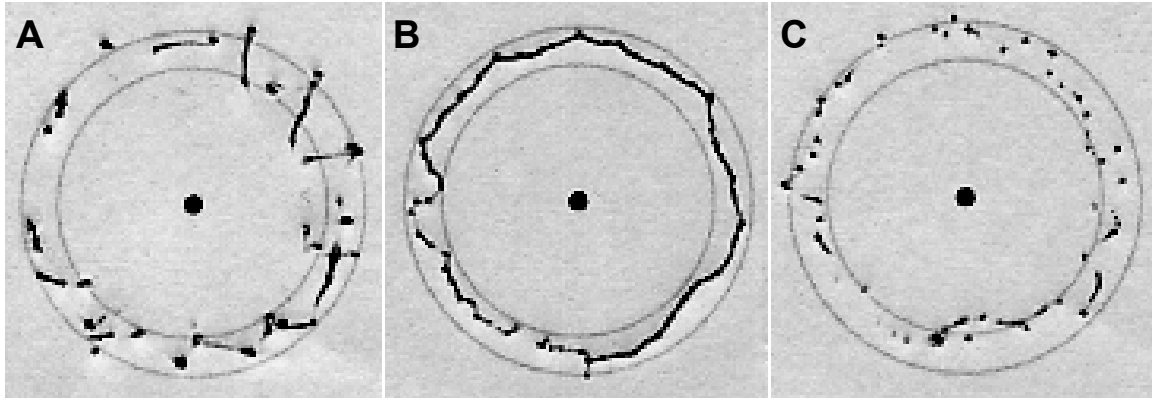
Figure 2.13: Representative trials under solid (A), baseline (B), and 59 ms time-delayed (C) tracking conditions. Note that the baseline circle is the most continuous and round. While the solid target has more continuous lines than the time-delayed target, it also has heavy dots and dimpling indicative of high forces. Trials with median angular surround scores were selected.

2.4.5   Results

User Study 1

The results of this study indicate that the MCI can provide significant assistance while operating on a moving target. Figure 2.13 shows typical target results. Mean angular surround metric scores (Figure 2.14) for the baseline tracking condition ($81.9 \pm 4.5\%$ (mean $\pm$ standard error)) were over 50% greater than for the solid condition ($53.8 \pm 5.0\%$), with clear statistical significance ($t(14) = .1987, p = 0.0009$). Similarly, axial force data indicates that subjects applied less than 50% as much force and spent less time at elevated forces under the baseline MCI tracking condition. Aggregating the data from all four subjects (Figure 2.15), the 90th percentile for force samples using the solid tool (17.5 N) is roughly double the 90th percentile for the baseline tracking condition (8.5 N).

A comparison of mean angular surround metric scores related to the amount of
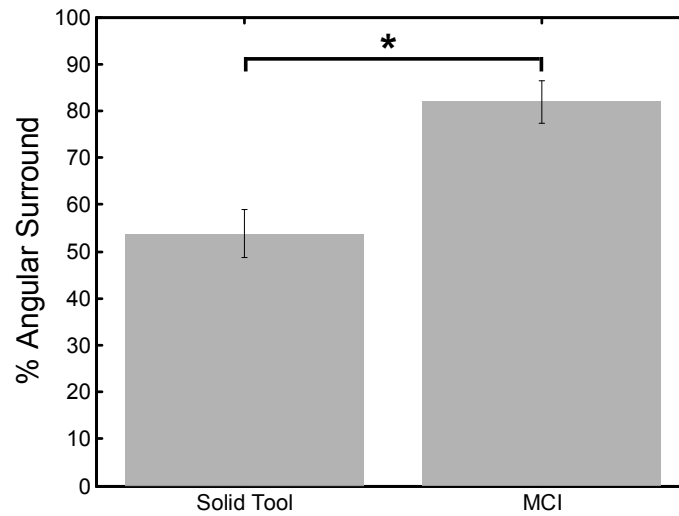
Figure 2.14: Performance under baseline MCI and solid tool tracking conditions. Error bars indicate standard error. The asterisk marks statistical significance.
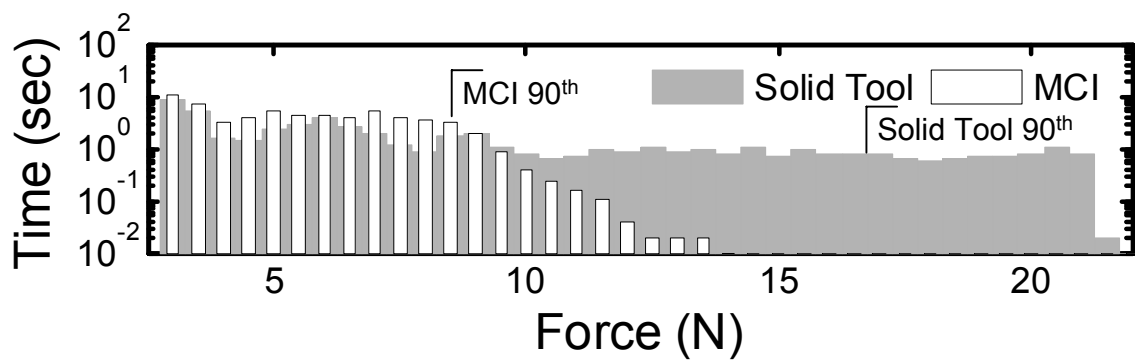

Figure 2.15: Histogram of applied force samples under baseline MCI and solid tool tracking conditions. Note that smaller forces are consistently applied under the baseline condition. 90th percentiles are marked. The zero force bin is not shown.
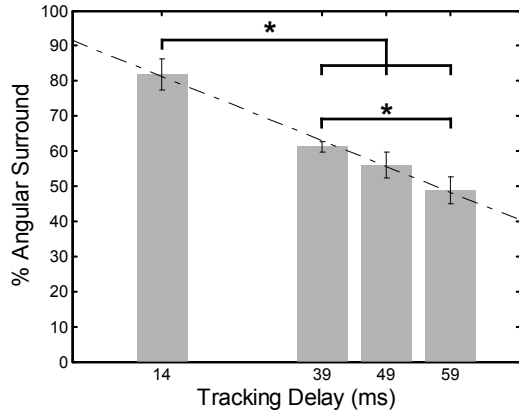
Figure 2.16: Performance under delay tracking conditions. Error bars indicate standard error. Asterisks indicate statistical significance. Dotted line shows fitted linear model ($R^2 = 0.9937$).
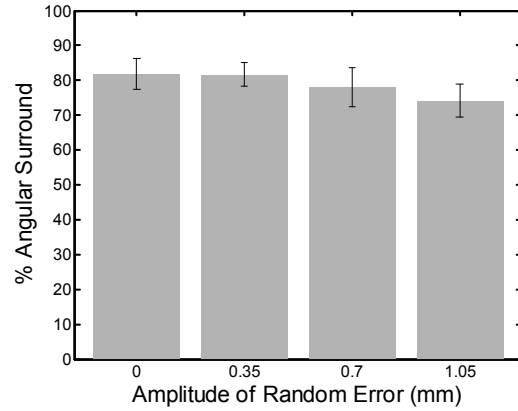
Figure 2.17: Performance under positional error tracking conditions. Error bars indicate standard error.

delay error (Figure 2.16) demonstrates decreases in performance ranging from 67% to 33% with increasing delay ($f(3, 28) = 16.005$, $p < .001$). Statistically significant differences were indicated between the baseline condition and tracking with delays of 39 ms ($61.2 \pm 1.5\%$), 49 ms ($56.0 \pm 3.7\%$), and 59 ms ($48.8 \pm 3.8\%$). A significant difference also exists between the means of the 39 ms and 59 ms tracking conditions ($p = 0.02$). Trend analysis indicates that the data is well fit by a linear model ($p < 0.001$).

An analysis of mean angular surround metric scores related to positional error did not demonstrate significant differences under ANOVA analysis ($f(3, 28) = 0.638$, $p = 0.597$). As seen in Figure 2.17, the mean score under the baseline condition differed very little from those with error amplitude factors of 0.35 mm ($81.7 \pm 3.3\%$), 0.70 mm ($78.0 \pm 5.5\%$), and 1.05 mm ($74.2 \pm 4.6\%$).

User Study 2

Results from this study demonstrate that the EKF is an effective approach for compensating time delay. Figure 2.18 shows typical target results. Mean angular surround scores for EKF delay-compensated tracking (Figure 2.19) were similar to the baseline tracking condition from User Study 1 for all three conditions of 39 ms (83.1 ± 3.7%), 59 ms (85.2 ± 2.6%), and 89 ms (84.4 ± 3.8%). Likewise, delay-compensated tracking showed performance increases over delayed tracking ranging from 13% to 24%. The mean angular scores for delayed tracking were 70.4 ± 4.8%, 61.1 ± 4.6%, and 61.0 ± 5.2% for 39, 59, and 89 ms delays, respectively. Statistically significant differences at $p < 0.05$ were observed between the mean scores of each delay-compensated tracking condition to each delayed tracking condition. Delay-compensated tracking also yielded smaller axial forces than those observed for delayed tracking (Figure 2.20).

An analysis of mean angular surround metric scores related to heart rate variability did not demonstrate significant differences under ANOVA analysis ($f(3, 36) = 0.705$, $p = 0.555$). As seen in Figure 2.21, the performance against a fixed-rate target was comparable to that against a variable rate target with σ_{HR} equal to 1.0 bpm (85.9 ± 2.6%), 2.0 bpm (84.1 ± 2.9%), 3.0 bpm (80.5 ± 3.6%), and 4.0 bpm (81.5 ± 2.5%).
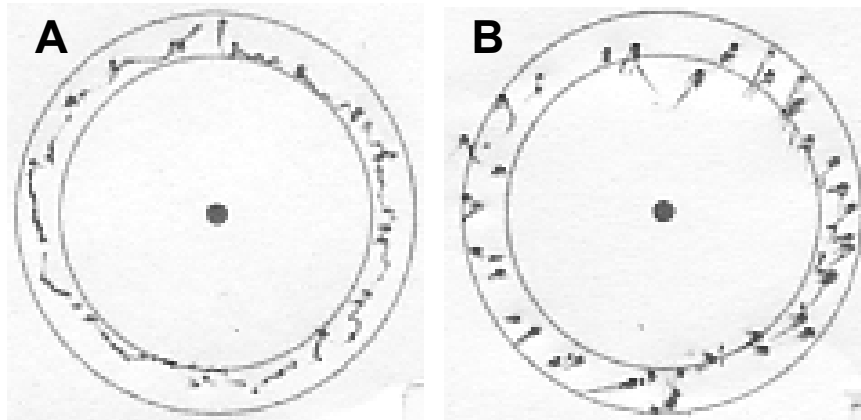
Figure 2.18: Representative trials under 89 ms EKF delay-compensated (A) and time-delayed (B) tracking conditions. Note that the delay-compensated example is more continuous and round than the time-delayed example. The latter is fragmented and has heavy dots and dimpling that are indicative of high forces. Trials with median angular surround scores were selected.
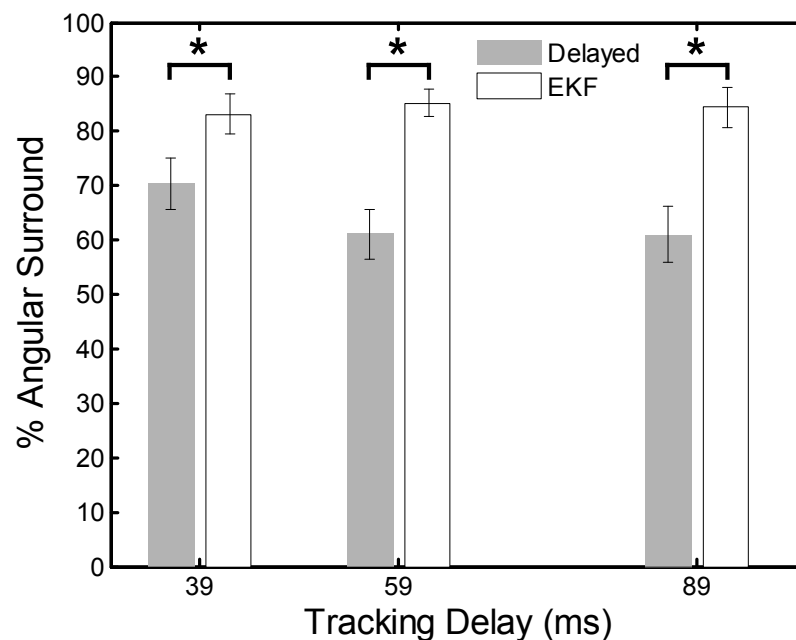
Figure 2.19: Performance with EKF delay compensation and without. Error bars indicate standard error. Asterisks indicate statistical significance.
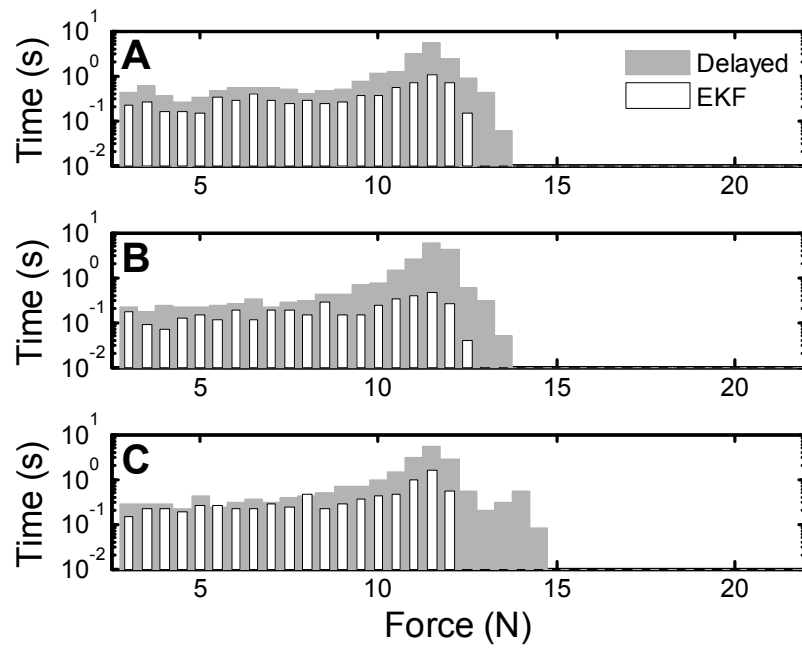
Figure 2.20: Force application with and without delay compensation for delays of 39 ms (A), 59 ms (B), and 89 ms (C). Note that smaller forces are consistently applied under the delay-compensated tracking conditions. The zero force bin is not shown.
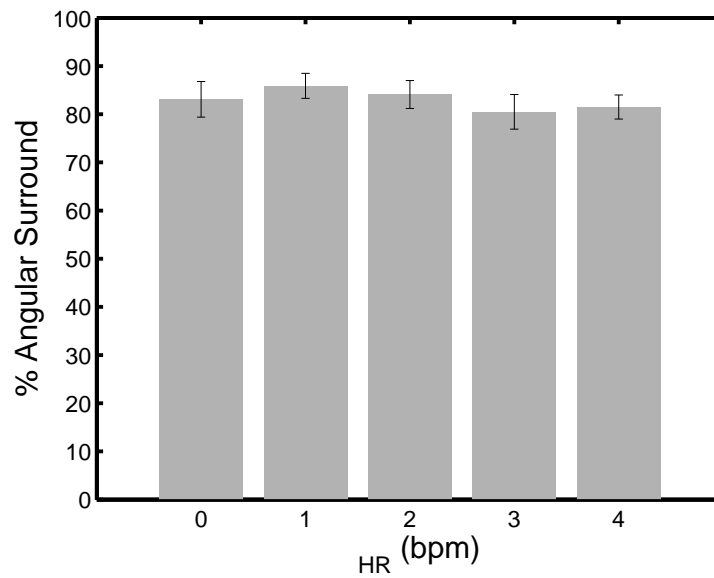
Figure 2.21: Performance under variable heart rate tracking conditions. Error bars indicate standard error.

2.5   System Accuracy Under 3D Ultrasound Guidance

Water tank experiments were conducted to measure the motion synchronization accuracy of the system under 3D ultrasound guidance. To do these, a real-time 3D ultrasound target segmentation algorithm was first incorporated into the system to provide position measurements to the EKF. The target was set to be an X-shaped fiducial that can be easily mounted to an annuloplasty ring (Figure 2.22B). This fiducial was specifically chosen because detecting two intersecting lines is suited for an existing real-time 3D ultrasound segmentation algorithm based on the modified Radon transform [46]. This algorithm is known to provide target position measurements with 1.30 mm RMS accuracy under *in vitro* conditions. Because higher noise is present *in vivo*, we also tested this system in two other noise conditions in which large, zero mean Gaussian terms with standard deviations of 2.0 mm or 3.0 mm were added to the segmented target positions. This yielded three noise conditions with overall RMS accuracies of $\sigma_R \in \{1.30, 3.30, 4.30\}$ mm.

2.5.1   Experimental Setup

The target and instrument were imaged by a real-time 3D ultrasound probe in a water tank at 28 Hz (Figure 2.22A). Data was streamed from the ultrasound machine (SONOS 7500, Philips Healthcare, Andover, MA) to a computer over an ethernet connection. The stream was captured by the computer and passed to a graphics processing unit (8800GTS, nVidia Corp, Santa Clara, CA) where the volumes were auto-
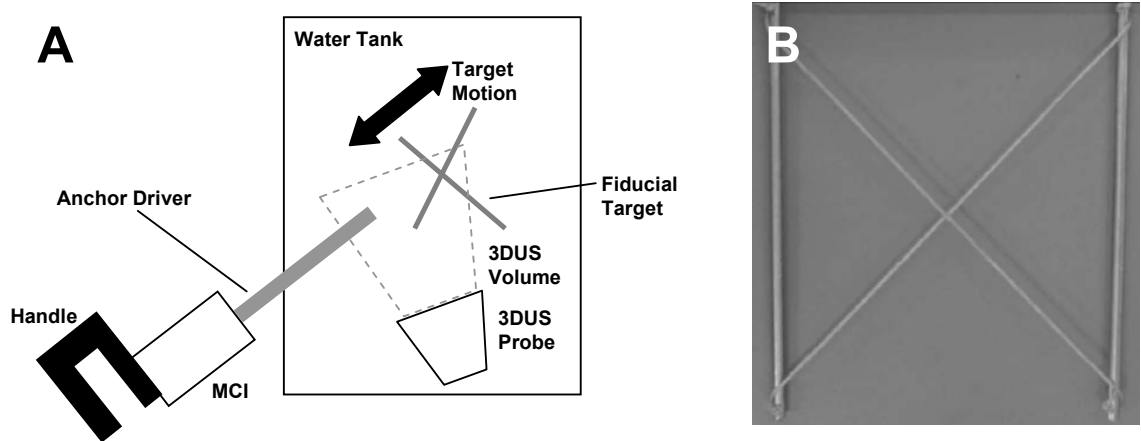
Figure 2.22: Setup for motion synchronization experiments (A) and X-shaped fiducial target (B).

matically segmented using the modified Radon transform segmentation algorithm [46] to obtain target position measurements. The measurements were corrupted with additive Gaussian noise (depending on the noise condition), then passed to a third thread for EKF processing. This returned predicted target positions 82 ms in the future (68 ms from imaging and segmentation, 14 ms from instrument lag time) and were sent to the 1 kHz PID control loop for the robot.

Five motion synchronization trials were conducted per noise condition. The target simulated mitral valve motion at 60 bpm with the cam-driven mechanism described in Section 2.4.1. MCI position and true target position were measured at 1 kHz with potentiometers and stored for offline processing. Target measurements and EKF predictions were acquired at the 3D ultrasound sampling rate (28 Hz) and stored as well. Accuracy evaluation was done on the 20 s of tracking data following 20 s of EKF initialization.

2.5.2 Results

Typical data and results for each noise condition are shown in Figure 2.23 and overall performance is summarized in Figure 2.24. Mean RMS accuracies for EKF predictions were 1.01 ± 0.02 mm, 1.08 ± 0.03 mm, and 1.22 ± 0.05 mm for noise levels of 1.30 mm, 3.30 mm, and 4.30 mm (respectively) and showed statistically significant reductions in measurement error ($p < 0.0001$ for each case). Mean MCI synchronization errors were 1.15 ± 0.04 mm, 1.23 ± 0.06 mm, and 1.28 ± 0.10 mm RMS for the three noise conditions. The mean RMS error added to the system from the MCI following the prescribed EKF trajectory was 0.14 ± 0.01 mm and this difference was statistically significant ($p = 0.002$). The RMS noise accuracy for the X-tracking algorithm observed across all 15 trials was 1.30 ± 0.01 mm, in agreement with previous reports [46].

2.6   Discussion

In vitro user trials demonstrate that a motion compensation system is an effective aid for surgical tasks on the beating mitral valve annulus. Motion synchronization allowed users to operate with both increased dexterity and reduced forces. In User Study 1, the angular surround scores indicative of dexterity increased by approximately 50% between the solid tool and baseline tracking conditions while the 90th percentile for force decreased by a similar ratio. These performance gains were maintained when increasing levels of positional error were inserted into the system, but disappeared when uncompensated time delays were added to the tracking data.
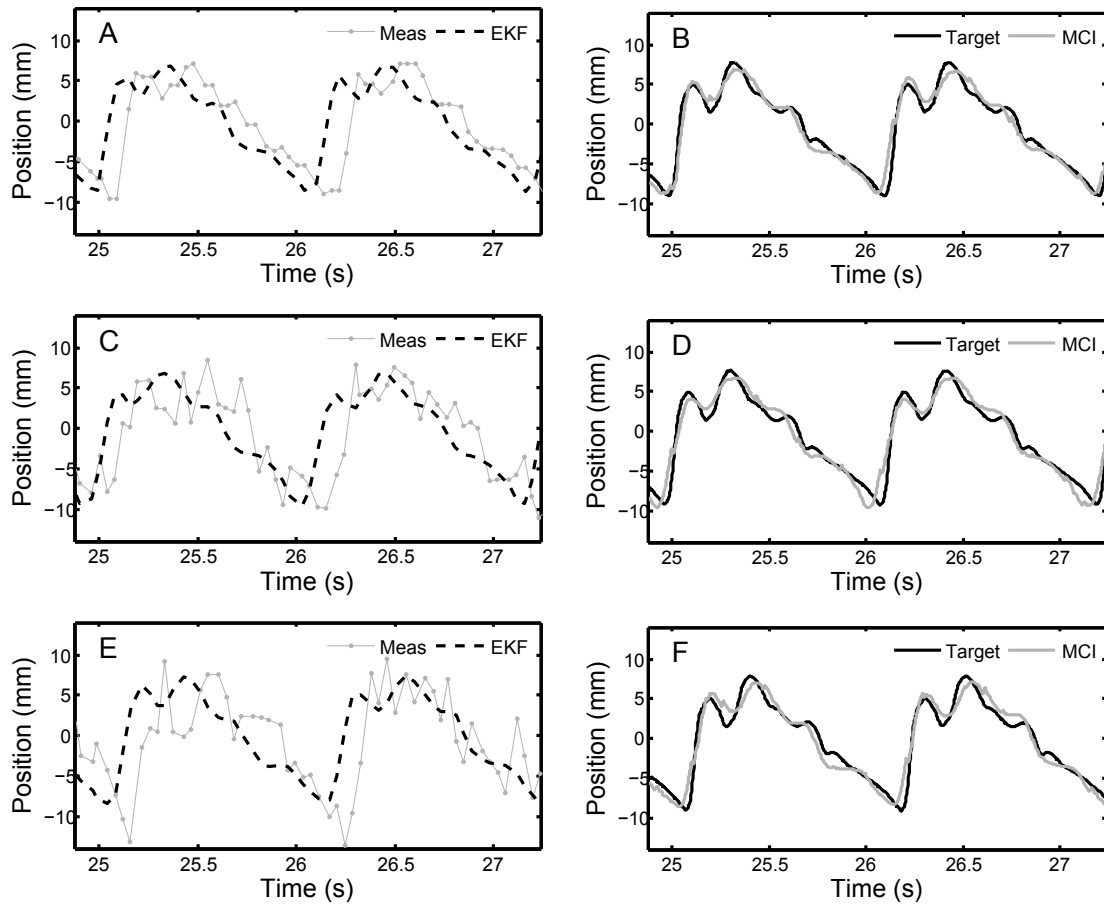
Figure 2.23: Examples of data, filtering, and motion tracking results. Left column shows measurements from 3D ultrasound target segmentation and EKF predicted target trajectories for each noise condition ($\sigma_R = 1.30$ mm (A), 3.30 mm (C), and 4.30 mm (E)). Corresponding MCI and true target trajectories for each noise condition ($\sigma_R = 1.30$ mm (B), 3.30 mm (D), 4.30 mm (F)) are shown in the right column.
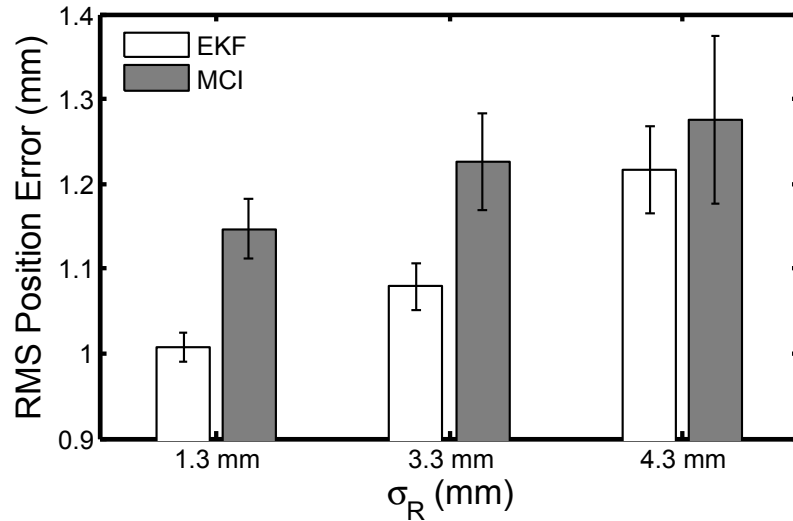
Figure 2.24: EKF prediction performance and MCI tracking performance over three increasing noise conditions. Error bars indicate standard error.

The strong dependence of user performance on delay emphasizes that precise timing is essential for successful motion compensation. Left uncompensated, tracking delays produced serious errors during the rapid recoil of the target associated with the relaxation of the left ventricle. During this motion the valve moves towards the operator, nearly covering its entire 18 mm range of motion. Because of the delay, the MCI continued to servo towards the oncoming target and abruptly collided with it. Qualitatively, while subjects did not always notice added positional error, they universally correctly identified and expressed dismay over tracking delay.

The introduction of a predictive EKF into the system effectively removed the performance decrease associated with tracking delays. The angular surround scores for delay-compensated tracking conditions exceeded their respective delayed tracking conditions by 13% to 24%, depending on the degree of delay. The forces applied in the delay-compensated conditions also decreased relative to the delayed conditions,

although to a lesser extent than seen between baseline tracking and the solid tool. The delay-compensated scores of User Study 2 marginally exceeded the baseline scores of User Study 1 by an amount that is consistent with the removal of the MCI's 14 ms lag time (as predicted by the linear model from User Study 1). However, caution must be taken when making a direct comparison of the angular surround scores between User Studies 1 and 2 because of differing amounts of in-trial training (eight trials in User Study 1 and ten trials in User Study 2). It is reasonable to conclude that EKF delay compensation restored the MCI tracking performance to at least baseline tracking conditions in cases of delay. Moreover, the performance increases observed for delay-compensated tracking showed no degradation across the range of time delays expected for 3D ultrasound-guided procedures.

The levels of random positional error explored in the user studies had a negligible effect on the benefits of MCI tracking. No statistically significant differences were found between user performance under all three positional error conditions and the baseline condition. This result suggests that if the timing with the valve's sudden recoil is maintained, the value of the MCI's tracking is robust in the face of positional errors as high as ± 1 mm. This may be attributed, in part, to compliance in the system: in the MCI's mechanism and in the foam pad on the target platform, which introduce compliance similar in nature to that in the heart.

Heart rate variations in the target motion also provided no significant degradation in user performance over the clinically-obtained beat-to-beat statistics (Figure 2.9). This is not surprising given that the EKF estimates did not degrade on these levels of heart rate variation. In some respects, tracking a variable rate target was another

approach to injecting positional error into the system since the filter remained in phase with the target (see, for instance, Figure 2.12). Extremely large beat-to-beat variations would cause the EKF to break synchronization with the target because the linearization of the measurement function $h(\boldsymbol{x}(t))$ would become inappropriate. There are several potential routes for improvement if more aggressive heart rate variations than those explored here are encountered. First, heart rate variability could be reduced through drug treatment and electrical pacing of the heart to a fixed rate. Second, following [51, 6], ECG information could be used to obtain direct measurements of heart rate. This could reduce the effect of the nonlinearity in $h(\boldsymbol{x}(t))$ since, as mentioned in Section 2.3.1, perfect knowledge of $\omega(t)$ turns this into a linear estimation problem. Note that the EKF, a nonlinear filtering approach, would still be useful with these measurements because they are sampled at discrete intervals but $\omega(t)$ is continuous.

The efficacy of this motion compensation system is based on the assumption that the motion that must be tracked is modeled well by a 1D approximation. Previous research on augmenting surgical procedures with robotic tracking have focused on coronary artery bypass grafting, requiring a 3D model of target motion [44, 51, 24, 6]. The characterization of mitral valve annulus motion in Section 2.1 shows that the annulus undergoes fast motion primarily along one axis; however, there is also about 2 mm of off-axis motion (Figure 2.2). Our tests suggest that the passive compliance of the mitral valve annulus assists with these minor off-axis deviations.

In this chapter, particular emphasis has been placed on predictive filtering to mitigate the dominant sources of tracking error in the system: 3D ultrasound delay

and noise. Using this approach with the MCI in a 3D ultrasound-guided servoing task, tracking errors within 1.3 mm RMS were achieved in the presence of large measurement noise (1.3–4.3 mm RMS) and 82 ms of system delay. This is a significant improvement over the 4.6 mm RMS errors that would be incurred in a time-delayed but otherwise noiseless tracking system. Although the tracking errors shown here are low, there is the potential for further lowering error through a more sophisticated controller. Repetitive control methods are well suited for quasiperiodic servoing tasks [27, 12, 36, 29] and model predictive control has shown promising results in external beating heart tracking [24, 6]. These techniques may reduce the 0.14 mm tracking error that is attributable to the PID controller used in the current system.

Chapter 3

Real-Time Tissue Tracking

In the previous chapter, we showed that a motion compensation system can enhance surgical task performance for beating heart mitral valve annuloplasty. However, the system that was used was limited to tracking X-shaped fiducial targets. A system suitable for intracardiac surgery must have real-time tissue tracking capabilities to guide the surgical instrument. Segmenting and tracking the mitral valve annulus in 3D ultrasound is difficult due to noisy imaging and poor shape definition [45]. Furthermore, the requirement for real-time (24–30 Hz) processing constrains the computation time available per volume. Rather than track the entire annular structure, we propose to track the tissue that the instrument is pointed toward. This simplification is clinically motivated: at any given moment, the surgeon only interacts with the small region of annulus directly in front of the instrument. This approach allows the tracker to take advantage of the high spatial coherence of the instrument, which appears as a bright and straight object in the volume, to locate an otherwise poorly defined anatomical target. In this way the instrument is similar to a flashlight that
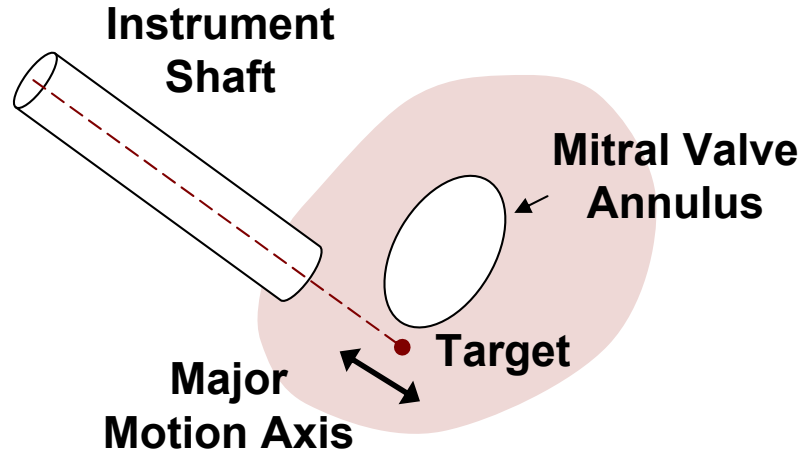
Figure 3.1: Real-time tracking of the surgical target is achieved by projecting along the instrument shaft until it intersects tissue.

highlights the tissue target (Figure 3.1).

In this chapter, we present a new, synergistic 3D ultrasound-guided motion compensation system for use in beating heart intracardiac procedures. The principle behind the system is to leverage the surgeon's proficiency at identifying and aiming the instrument toward the desired surgical site, then to automatically track the tissue in front of the instrument under 3D ultrasound guidance. This approach is suited to tracking the mitral valve annulus because it has a predominantly uniaxial motion trajectory. This enables the development of a novel, real-time tissue tracker that is robust to ultrasound noise because it draws on the high spatial coherence of the instrument to locate the tissue target. In the following, we describe the motion compensation system and its components, then validate its performance in experiments conducted in a water tank and an *in vivo* Yorkshire pig beating heart model.
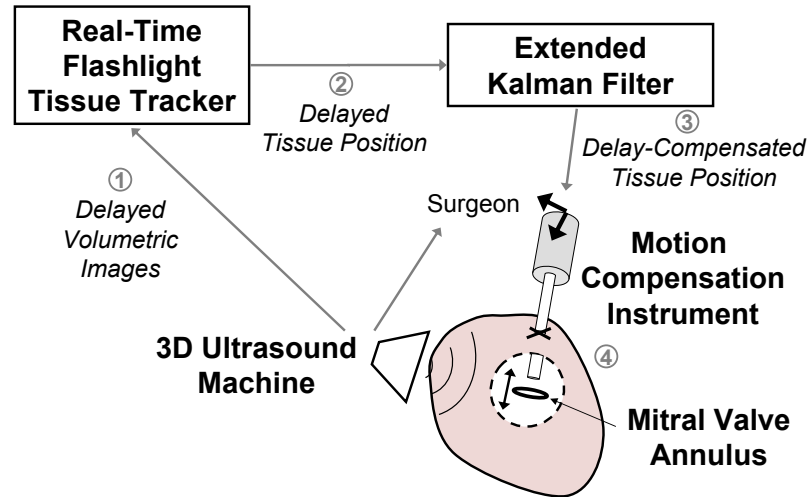
Figure 3.2: The motion compensation system uses 3D ultrasound imaging to automatically synchronize the motion of an actuated, handheld surgical instrument with a tissue target. Circled numbers indicate the order of data flow through the system (1–3) and the resultant tracking position of the motion compensation instrument (4).

3.1   3D Ultrasound-Guided Motion Compensation System

The motion compensation system assists the surgeon by following intracardiac structures that undergo rapid translational movement primarily along one axis, like the mitral valve annulus. It incorporates a new, real-time 3D ultrasound tissue tracker that we term the "flashlight" tracker. We integrate it with a miniaturized version of the actuated, handheld 1 degree of freedom (DOF) motion compensation instrument (MCI) and predictive extended Kalman filter used in Chapter 2 to compose the system shown in Figure 3.2. The flashlight tissue tracker supplies measurements to the filter which, in turn, commands the instrument. The surgeon designates the desired surgical site by aiming the tip of the instrument toward it.
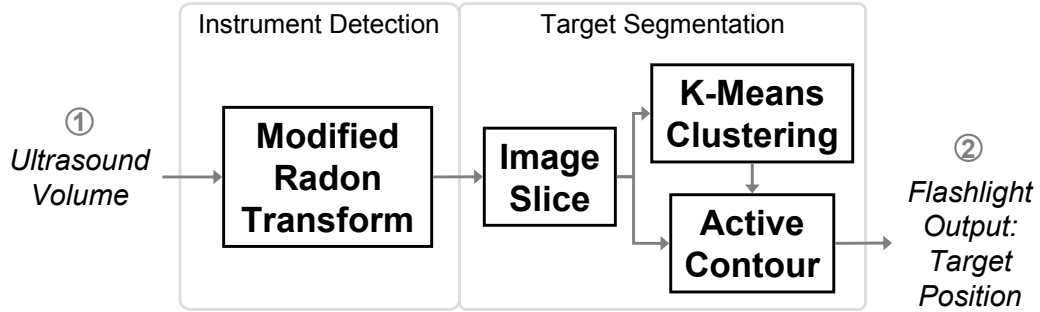
Figure 3.3: Data processing chain in the flashlight real-time tissue tracker. Circled numbers correspond to those shown in Figure 3.2.

3.1.1 Real-Time 3D Ultrasound "Flashlight" Tissue Tracker

Figure 3.3 charts the data flow in the flashlight tracker. It consists of two consecutive operations: instrument detection followed by target segmentation. We employ the modified Radon transform for real-time detection of the ray that passes through the central axis of the instrument shaft [48]. Next, we distinguish between the target and instrument along this ray. We construct an image slice through the ultrasound volume that contains the instrument shaft. Pixels in the slice that exceed a grayscale intensity threshold I_t are grouped into two clusters based on Euclidean distance using the K-means algorithm [1]. The value of I_t is empirically chosen to remove noise and the mitral leaflets from the clustering. The resulting clusters roughly coincide with the locations of the instrument and tissue target. *A priori* knowledge of the ultrasound probe placement relative to the instrument and the tissue allows us to designate the more distal cluster as the target.

Finally, an active contour is placed on the target cluster to segment its surface. The active contour is governed by the minimization of the energy equation

$$E = \int_S (\alpha E_{\text{elastic}} + \beta E_{\text{bending}} + \gamma E_{\text{image}}) dS. \qquad (3.1)$$

The energy consists of an elastic term that encourages uniform point spacing on the contour, a bending term that penalizes high curvature, and an image gradient term that forces the active contour toward edges. The parameters α, β, and γ are chosen to balance the relative contributions of each term. The active contour is initialized by radially projecting n points from the center of the K-means target cluster until they reach a pixel intensity lower than I_t. Real-time minimization of Equation 3.1 is achieved through a greedy algorithm with point neighborhoods based on 8-connectivity [73]. The first intersection point of the contour with the ray along the instrument shaft is taken as the target position.

Examples of the tissue segmentation steps are shown in Figure 3.4 for two cases where the instrument is far and close to the target. Note that the use of an active contour enables target segmentation when the instrument is near the target.

3.1.2 Time Delay Compensation

Although the flashlight tissue tracker operates in real-time, there are latencies in the system that must be removed prior to commanding the motion compensation instrument. The acquisition and transfer of ultrasound volumes requires approximately 30 ms and the subsequent detection of the instrument takes an additional 30 ms [48]. The mitral valve annulus traverses over half of its trajectory in 60 ms at the onset of ventricular relaxation.

As in Chapter 2, we compensate for time delay by exploiting the nearly periodic motion of the heart to predict the tissue trajectory into the near future. Briefly, we model the target trajectory as a time-varying Fourier series with an offset (Equa-
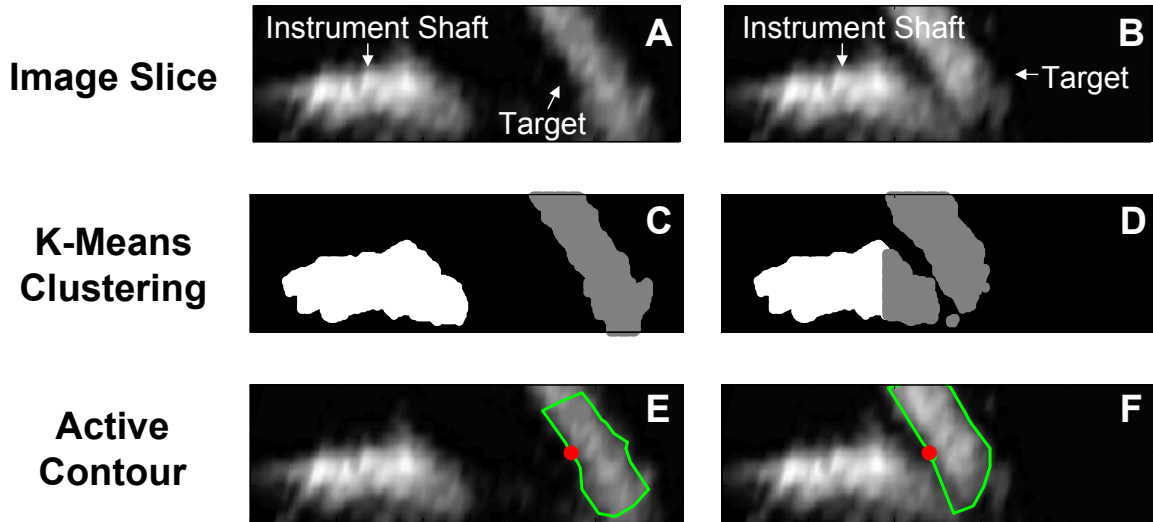
Figure 3.4: Outputs from each tissue segmentation step for examples where the instrument is far and near the target (left and right columns, respectively). The image slice through the instrument is shown in the top row. K-means clusters are shown as white and gray objects in the middle row. The segmented target shape (line) and tracking point (dot) are shown in the bottom row.

tion 2.5). We estimate the parameters of this model using an extended Kalman filter (EKF). Because it is recursive, it is amenable to a real-time implementation. It has the added benefit of providing noise reduction to the estimated target trajectory through the regularization of the flashlight tracker measurements against the motion model.

3.1.3   Motion Compensation Instrument

The motion compensation instrument (MCI) is a handheld surgical anchor deployment device that actively cancels the dominant 1D motion component of the mitral valve annulus. Figure 3.5 shows the instrument, which is a miniaturized version of the prototype from Chapter 2 that is compatible with the space limitations inside of the operating room. It incorporates a voice coil linear motor (NCC10-15-023-1X, H2W
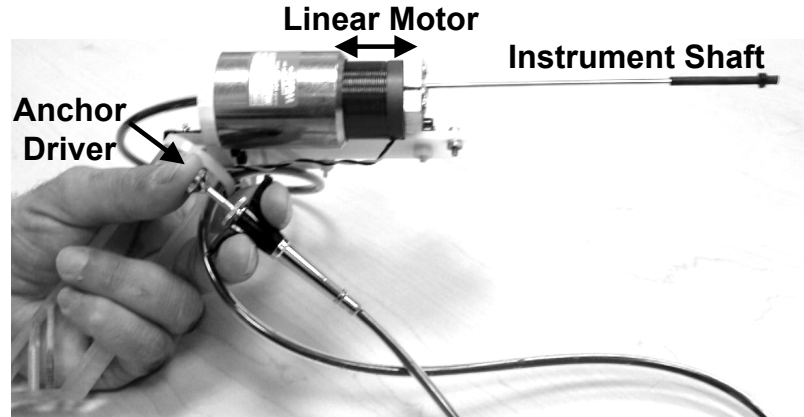
Figure 3.5: The motion compensation instrument is a 1 DOF actuated anchor driver instrument that is capable of tracking fast intracardiac structures.

Technologies, Valencia, CA, USA) for actuation of the anchor deployment stage up to speeds and accelerations of 1.49 m/s and 103 m/s^2 with a 25 mm range of motion. A high linearity potentiometer (P3 America, San Diego, CA, USA) provides position sensing. The instrument position is controlled with a slightly overdamped response by a 1 kHz PID servo loop and has a -3 dB point of 35.0 Hz (-40 dB per decade roll off rate). The overall weight of the instrument is 0.76 kg, which is less than 50% of the weight of the original. Because of the reduced moving mass, the latency of the instrument is lowered from 14 ms to 10 ms from the instrument in Chapter 2. Weight reduction is achieved by using a smaller motor and light plastic materials for construction.

3.1.4   System Implementation

The motion compensation system uses a dual CPU AMD Opteron 285 2.6 GHz PC with 4 GB of RAM to process the ultrasound data and control the motion compensation instrument. A 3D ultrasound machine (Sonos 7500, Philips Healthcare,

Andover, MA, USA) streams volumes at 28 Hz to the PC over a 1 Gb LAN using TCP/IP. A program written in C++ retrieves the ultrasound volumes and loads them onto a GPU (7800GT, nVidia Corp, Santa Clara, CA, USA) for real-time instrument axis detection. The GPU renders image slices through the instrument shaft that are rotated to be horizontal through a trilinear interpolation. Subsequent flashlight tissue tracking operations are done with a pixel intensity threshold of $I_t = 50$ and active contour parameters $n = 10$, $\alpha = 0.5$, $\beta = 0.5$, and $\gamma = 1.0$. Preliminary water tank experiments indicate that the flashlight tracker is robust to changes in I_t and the ratios between α, β, and γ up to or exceeding a factor of two. The EKF trains on 5 s of flashlight position data and feeds-forward a tissue trajectory 78 ms ahead (68 ms from image acquisition, transfer, and processing; 10 ms from instrument latency) to the PID servo loop controlling the MCI. The instrument is powered by a BOP36-1.5 M linear power amplifier (Kepco, Flushing, NY, USA). Real-time tissue tracking, predictive filtering, and control algorithms are executed on the CPU.

3.2 Water Tank Validation

The accuracy and benefits of the motion compensation system were assessed through a study of user performance in an *in vitro* beating heart surgical task. Ten subjects (seven male, three female, aged 20–34) were instructed to use the MCI to drive surgical anchors into a tissue phantom that simulated the motion of the mitral valve annulus in a water tank. The MCI either provided motion compensation through the system described in Section 3.1 or the MCI was set to act as a solid, noncompensating instrument.

3.2.1   Experimental Setup

The user trials were conducted in conditions that emulate those expected in a beating heart mitral valve annuloplasty procedure. Figure 3.6 depicts the setup. Valve motion was simulated by a cam follower mechanism that replicates the dominant 1D motion component of the human mitral valve annulus that was determined in Chapter 2 (Figure 2.2). A tissue phantom of 2 cm thick polyethylene foam was affixed to a load cell (Kistler, Spartanburg, SC, USA) that measured the forces applied by the MCI during the task, then mounted to the cam and positioned in a water tank. The cam simulated a heart beat of 60 beats per minute. The MCI was aligned at roughly 15 deg to the motion axis of the target and contrained to move in 1 DOF by a linear bearing guide rail. Subjects viewed the task through the monitor of the 3D ultrasound machine (SONOS 7500, Philips Medical, Andover, MA, USA). The ultrasound probe was positioned to simultaneously image the target and instrument and set approximately perpendicular to the target motion axis to mimic the probe placement conditions *in vivo*. A potentiometer measured target position for off-line assessment of system accuracy.

3.2.2   Testing Protocol

The subjects were instructed to deploy anchors into the moving tissue phantom with the MCI in a series of trials. They were informed that the dual criteria for a successful trial were that the anchor be securely deployed in the target and that the forces
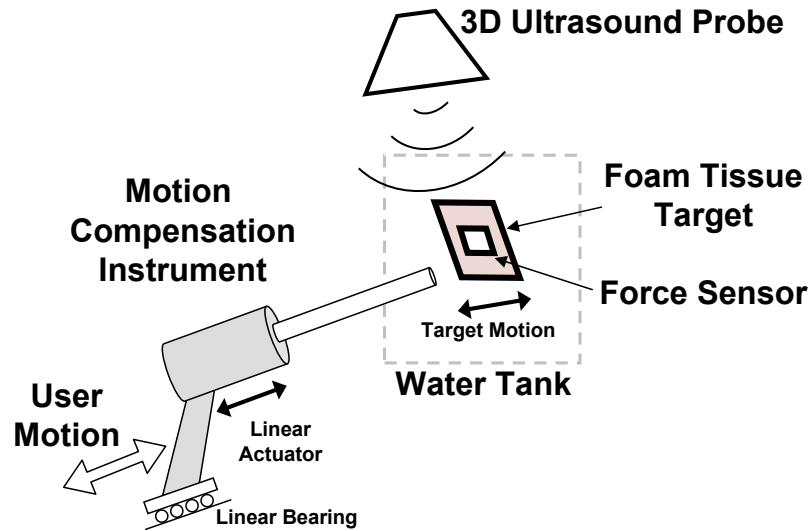
Figure 3.6: Water tank setup for user trials

applied to the target by the MCI during the task not exceed 15 N[1]. As a secondary

goal, subjects were also told to try to minimize the contact forces experienced while

deploying the anchor. The subjects were taught to use the anchor driver mechanism

on the MCI and trained to recognize the "feeling" of forces up to 15 N when pushing

the MCI into a stationary target. When the subjects became confident in their sense

of the forces applied, they were given six practice anchoring trials with the moving

target: three with motion compensation and three with a solid instrument. After

training, the subjects proceeded to perform the task in ten trials (five with motion

compensation and five with a solid instrument) in randomized order. The outcome

of each anchor driving attempt and the amount of force applied was shared with the

subject directly after each trial.

---

[1]15 N is the puncture force as determined in pilot studies on excised porcine mitral valve annulus
using the MCI's anchor driver mechanism. Puncture force will vary according to tissue properties
as well as the geometry of the instrument tip.
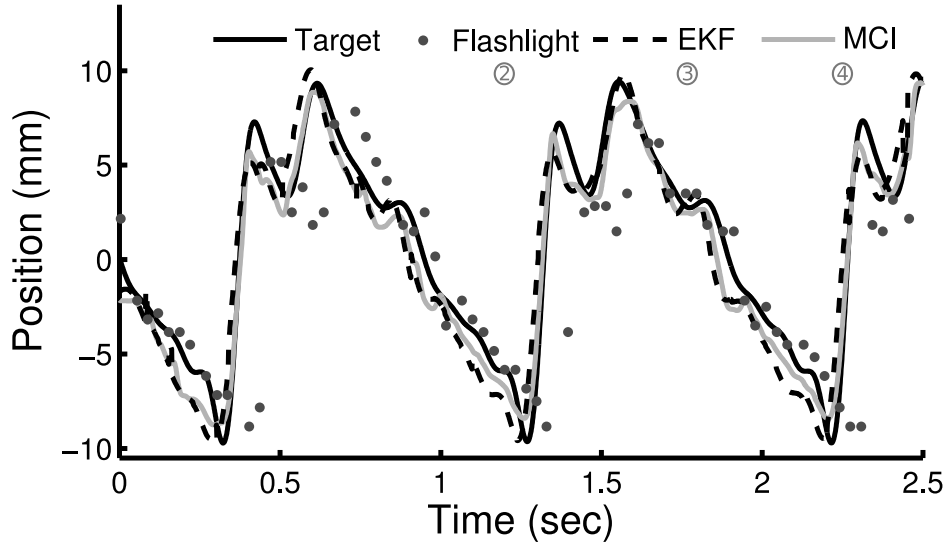
Figure 3.7: Water tank example of the system tracking a simulated mitral valve annulus target with the MCI. Intermediate outputs from the flashlight tracker and the EKF are also shown. Flashlight tracker positions are delayed by 68 ms because of latencies in 3D ultrasound and image processing. Relative position offsets are removed for clarity. Circled numbers correspond to those shown in Figure 3.2.

3.2.3   Results

Figure 3.7 shows a representative water tank tracking example. Intermediate system outputs from the flashlight tracker and EKF are also overlaid and labeled with circled numbers that match those in Figure 3.2. The motion compensation system provided instrument synchronization to the target with 1.8 mm RMS error (MCI vs. target traces in Figure 3.7). Position measurements from the flashlight tracker had RMS errors of 2.5 mm and were delayed by a total of 68 ms due to 3D ultrasound volume acquisition and transfer time and instrument detection latency. Tissue segmentation in the tracker required less than 1 ms. The error and time delay in the flashlight measurements were mitigated by the EKF, yielding a feed-forward target trajectory with 1.7 mm RMS error.
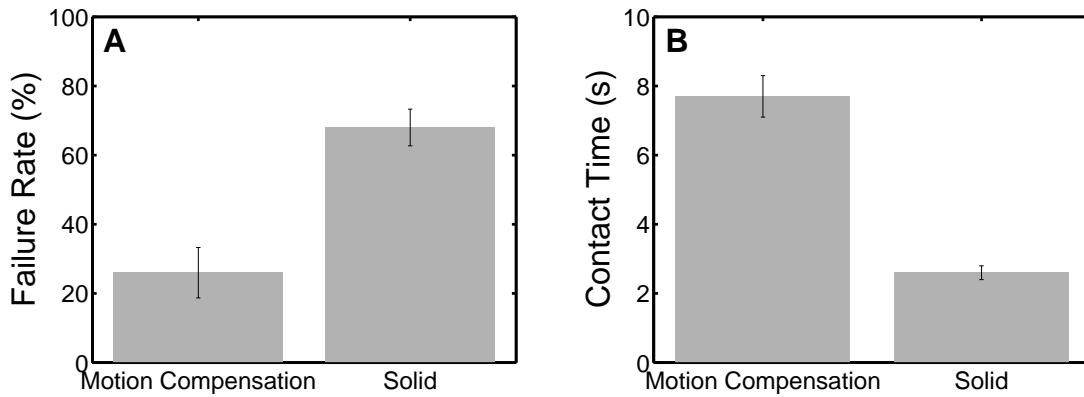
Figure 3.8: Mean failure rates (A) and mean continuous contact time (B) with motion compensation and with a solid instrument. Error bars indicate standard error.

Motion compensated anchor driving provided a mean failure rate that was roughly 60% less than that observed for a solid instrument (Figure 3.8A). A statistically significant difference between the means ($26.0 \pm 7.3\%$ for motion compensation and $68.0 \pm 5.3\%$ for a solid instrument, mean $\pm$ standard error) was apparent using a two-sided t-test ($p = 0.0002$). It should be noted that a subset of four subjects obtained 0% failure rates with motion compensation and $70.0 \pm 12.9\%$ without. The three engineers participating in the study belonged to this subset.

Motion compensation enabled the subjects to place the instrument in continuous contact with the target for nearly three times longer than with a solid instrument (Figure 3.8B). On average, subjects kept constant contact on the target for 7.7 ± 0.6 sec with motion compensation and 2.6 ± 0.2 sec without. This difference between the means is statistically significant ($p < 0.0001$). The range of continuous contact times observed over all motion compensation trials was 2.0–17.5 sec while the range for the solid instrument was 0.7–7.9 sec.

The forces applied to the target were reduced for trials using motion compensation.
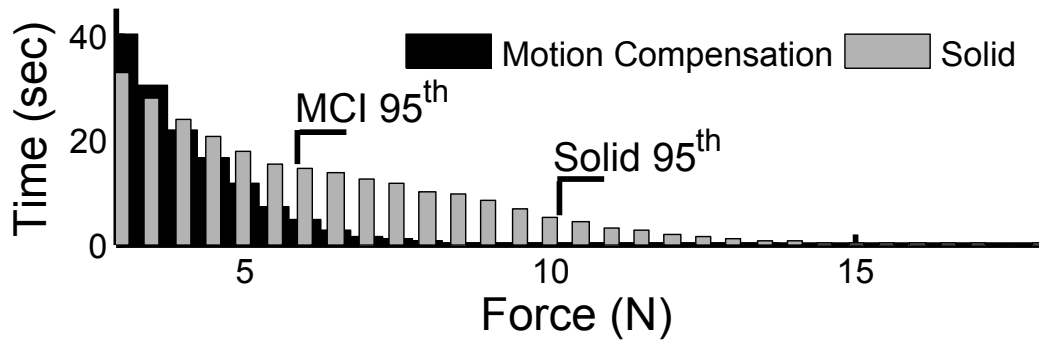
Figure 3.9: Histogram of applied forces over all user trials. 95th percentiles are shown.

Figure 3.9 shows a histogram of force samples for all trials for the motion compensated and solid instrument cases. The 95th percentile of forces for the solid instrument (10.2 N) is nearly twice that seen for motion compensation (5.8 N).

3.3 *In Vivo* Animal Study

3.3.1 Experimental Setup

In vivo validation of the tracking performance of the system was performed in a porcine beating heart model (Figure 3.10). Motion tracking was conducted in two Yorkshire pigs during open chest, beating heart procedures. In each trial, the tip of the MCI was inserted into the left atrial appendage and secured by a purse-string suture. The ultrasound probe was positioned epicardially on the left side of the heart to image the mitral valve and instrument. The surgeon was instructed to aim the instrument tip toward a point on the mitral valve annulus and orient the instrument shaft to align with the major motion axis of the annulus. Additionally, during the second animal trial the surgeon attempted to manually track the annulus
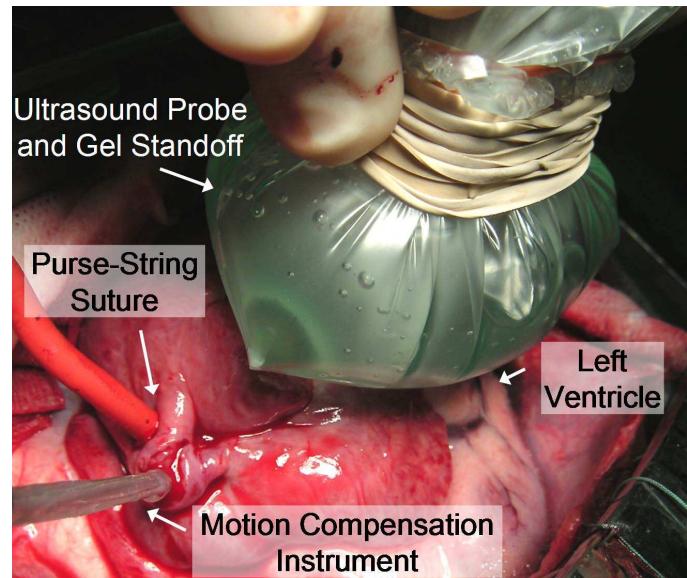
Figure 3.10: *In vivo* experiment setup.

with a stationary, noncompensating instrument. The surgeon was given three practice attempts, followed by the actual trial. Motion tracking occurred for 20 s in each trial.

The 3D ultrasound images from the trials were recorded and manually segmented to evaluate tracking performance. For each time-stamped volume, at least ten points were selected for the cardiac tissue along the instrument axis. These were used to calculate the centroid of the tissue target over time. Points in the left ventricle and on the mitral leaflets were excluded. Segmentations were verified by a cardiac surgeon with expertise in 3D ultrasound imaging and beating heart surgery.

The experimental protocol was approved by the Children's Hospital Boston Institutional Animal Care and Use Committee. All animals received humane care in accordance with the 1996 *Guide for the Care and Use of Laboratory Animals*, recommended by the US National Institute of Health.

Animal Trial No.	Tracking Condition	Heart Rate (bpm)	RMS Tracking Error (mm)
1	System	100	0.8
2	System	113	1.0
2	Manual	116	3.2

Table 3.1: *In vivo* tracking results for both animal trials. The second trial included tracking with and without the motion compensation system.

3.3.2   Results

In vivo results indicate that the system provides accurate motion tracking under surgical conditions. Figure 3.11A shows the tracking results for one of the *in vivo* trials. Both the positions of the tissue target and instrument are shown. The system tracked the target with a 1.0 mm RMS error while it beat at a spontaneous heart rate of 113 bpm. Qualitatively, the tracking does not mimic the target trajectory as faithfully as in the water tank case. A major contributor to this is the reduced imaging quality *in vivo*. Figure 3.12 depicts the imaging conditions while tracking over one heart cycle. Imaging artifacts and dropout are evident.

The system provided RMS tracking errors less than or equal to 1.0 mm in both *in vivo* trials (Table 3.3.2). In contrast, manual tracking (Figure 3.11B) yielded RMS errors of 3.2 mm on a slightly faster 116 bpm heart rate. The cross-correlation between the trajectories of the target and instrument in this case suggests that the surgeon lagged behind the target by approximately 339 ms. The RMS tracking error with this delay removed would be 1.3 mm.
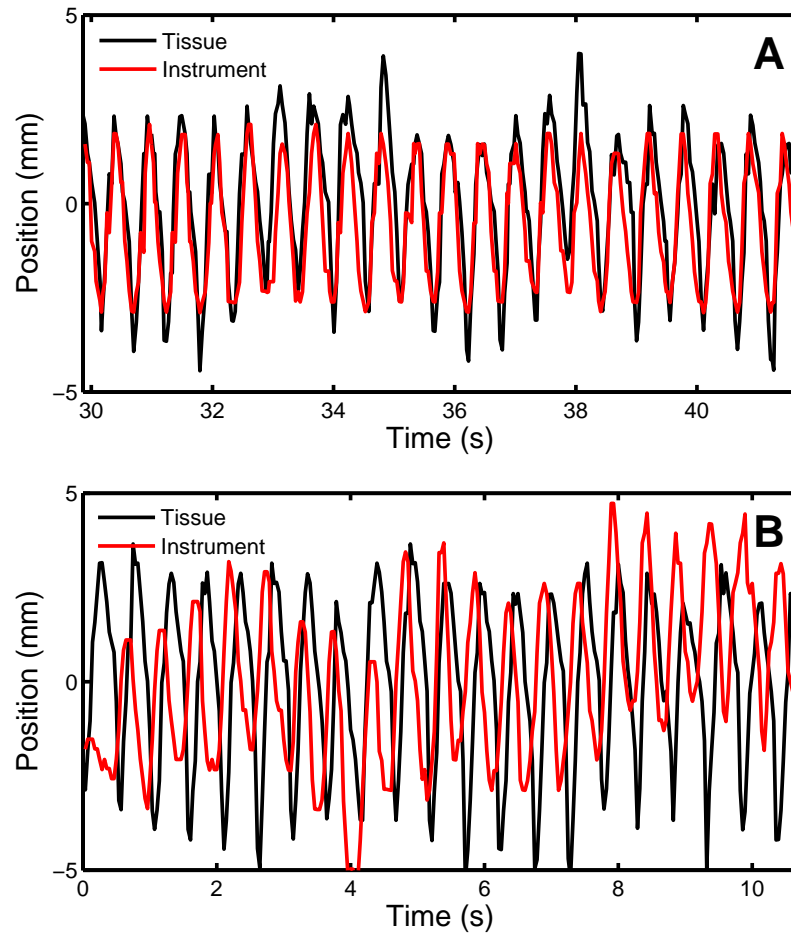
Figure 3.11: *In vivo* tracking examples conducted with the motion compensation system (A) and manually (B). The manual tracking example is the last and best attempt, after the surgeon had two training trials. The relative positional offsets between the instrument and tissue target are removed for clarity.
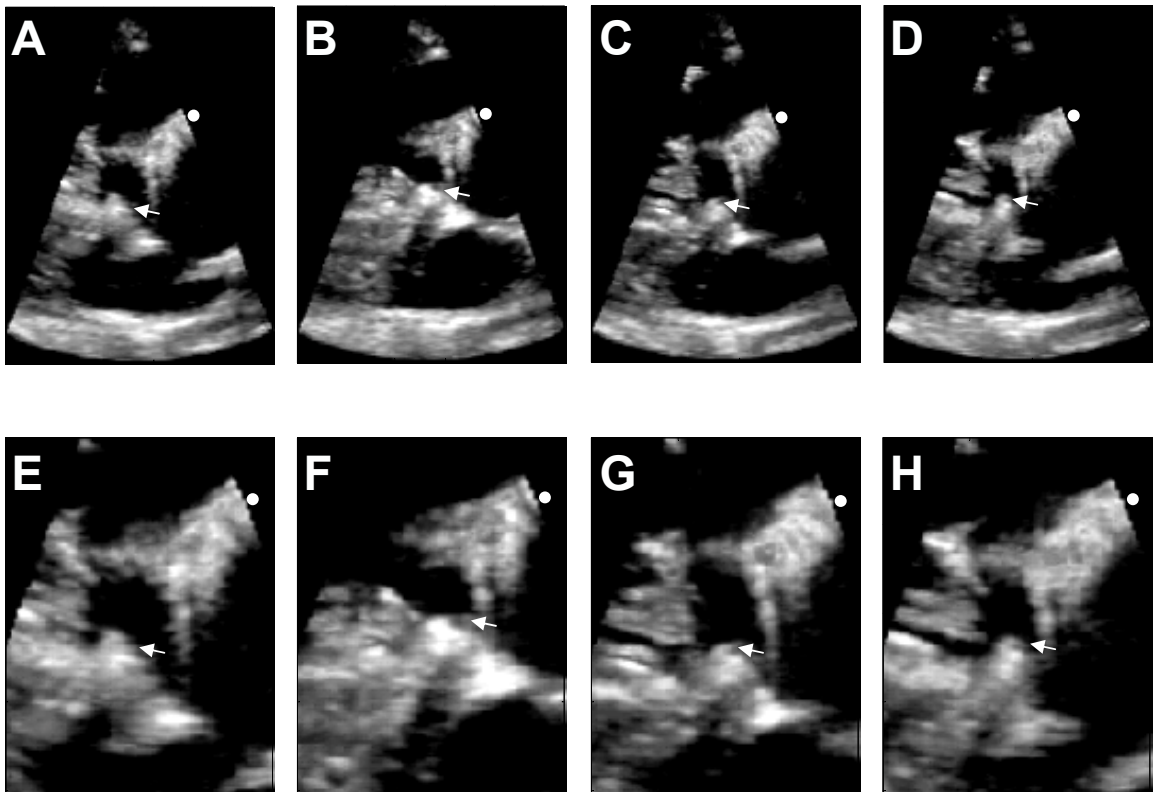
Figure 3.12: 3D ultrasound images of the motion compensation instrument tracking a region of the mitral valve annulus (arrows) in a beating porcine heart over one heart cycle. The base of the instrument shaft is denoted by a dot. Panels A–D (top row) show the entire field of view and panels E–H (bottom row) show corresponding magnified views of the instrument tip and target. The instrument tip is a cylindrical rod; however, the presence of ultrasound imaging artifacts distorts its appearance [30].

3.4   Discussion

These experiments show that robotic motion tracking of beating, intracardiac tissue is feasible in the surgical setting. Results from the *in vivo* study demonstrate that robotic tracking of the mitral valve annulus can be achieved with low 1.0 mm RMS error using standard 3D ultrasound imaging. This constitutes a 70% error reduction when compared to manual attempts. The flashlight tissue tracker proved to be robust to *in vivo* imaging artifacts, dropout, and noise by exploiting the spatial coherence of the instrument in ultrasound to pinpoint the tissue target. High accuracy motion tracking was achieved in the presence of significant delay and noise by regularizing position measurements against the cyclic motion of the heart with a predictive extended Kalman filter. Water tank results show that the filter reduces noise by 30% while simultaneously removing the overall system delay of 78 ms.

Using the system in an *in vitro* surgical anchor deployment task, subjects achieved success rates that were more than double those achieved with a non-compensated instrument. Furthermore, the system permitted more careful placement of the anchors by reducing the forces applied and extending the continuous contact time between the instrument and the target. While motion compensated anchor driving had relatively low failure rates, we anticipate that it can be driven to nearly zero with additional user training and a small modification to the instrument. The perfect performance of users with technology experience (e.g., engineers) suggests that the other users could benefit from more practice. Indeed, several users were confused by ultrasound visualization and impaired by the inertial forces resulting from the actuator's moving mass, which could be difficult to distinguish from contact forces. This led to cases

where the user would not push the instrument firmly into contact with the target. Modification of the instrument to include a counterbalancing mass may mitigate the loss in haptic feedback that results from inertial effects.

Prior research has shown that humans cannot track the heart when it is beating faster than 60 bpm [18, 32]. The preliminary *in vivo* manual tracking results of this chapter suggest that the main reason for this is the presence of a large lag that puts the instrument motion out of phase with the heart. For the cardiac surgeon in this study, we estimate this lag to be 339 ms on a heart beating at 116 bpm. This is consistent with the lags measured by Jacobs *et al.* for tasks against simulated heart motion at 35 and 60 bpm [32]. A retrospective analysis of the manual tracking trial suggests that the surgeon was able to match the frequency and amplitude of the annular trajectory reasonably well – to 1.3 mm RMS error when corrected for the 339 ms lag. It is unlikely that training will reduce the lag to levels low enough to achieve accurate manual tracking: human visual processing requires roughly 150 ms [63] and, as discussed above, even a 60 ms delay is intolerable for motion compensation. The surgeon could conceivably predict the tissue trajectory and feed-forward its motion like the strategy with the extended Kalman filter. However, even if possible, this would not be a clinically viable approach because it would severely limit the surgeon's ability to attend to the other aspects of the procedure.

The difficulty with manual heart tracking has inspired a number of parallel efforts in motion compensation for external heart procedures like coronary artery bypass graft. Nakamura *et al.* demonstrated automatic tracking of a laser point moving like the external heart wall with a 4 DOF robot guided by two high speed cameras [44].

Later, Ginhoux *et al.* provided an *in vivo* demonstration with a modified 6 DOF AESOP robot guided by a high-speed camera to track LEDs affixed to a beating porcine heart [24]. Similarly, Bebek and Cavusolgu used a 6 DOF PHANTOM robot to track sonomicrometry sensors sutured to the heart surface [6]. Because these systems function outside of the heart, they are able to achieve excellent results by using relatively large robots with fast (257–955 Hz) and accurate (250–330 μm) positioning sensors that either track fiducials or are placed onto the surgical target.

Limited by the constraints of operating inside the heart, the system in this work uses relatively low-frequency (28 Hz) and noisy (0.5 mm) 3D ultrasound imaging to directly track heart tissue. We also adopt a simplified 1 DOF robot that can function within the restricted space of the heart. Using this system in a beating porcine heart, we show a 70% decrease in error compared to manual tracking. We anticipate a larger benefit in the human heart because the human mitral valve annulus undergoes a larger excursion (10–18 mm) [70, 20] than was seen in the porcine model here (6 mm). However, the *in vivo* and *in vitro* studies suggest two potential improvements to the system. First, adding a low frequency term to the motion model in the filter would improve tracking the small, slowly-varying motion component seen in the *in vivo* result (Figure 3.11A) that is due to respiration. A second improvement, and the subject of the next chapter, is the modification of the robot controller to explicitly regulate the interaction forces between the robot and tissue to increase the saftey of the system. Although the forces measured in the *in vitro* anchor deployment task of Section 3.2 were roughly half those seen with a non-compensated instrument, large force excursions in excess of 5 N were still present (Figure 3.9). The tearing force for

in vivo heart tissue while deploying a surgical anchor is approximately 8 N[2] and for

safety the surgeon tries to maintain forces that are below 3 N.

---

[2]This force was determined using the MCI anchor driver mechanism on freshly excised porcine heart. The force will vary according to the tissue properties as well as the geometry of the instrument tip.

Chapter 4

Force Tracking with Feed-Forward Motion Estimation

The motion of the heart during beating heart surgery makes it difficult to apply precise forces for procedures like mitral valve annuloplasty. Anchor deployment trials from Chapter 3 demonstrate that this is the case even when using a position tracking motion compensation system: the system helps reduce contact forces but there are still fluctuations that can reach dangerous levels. There are a number of difficulties associated with using a positional controller during sustained contact against moving tissue. First, small errors in the estimated target position can cause the robot to interact with the tissue at high forces. Second, when in contact, the surgical target is shadowed by the instrument in 3D ultrasound and identifying its position accurately is challenging. Finally, because the robot is much stiffer than the heart, contact causes the tissue to comply with the location of the robotic instrument tip. Having the robot follow the position of the tissue in this state would not provide good motion

compensation because the tissue location is forced by the robot. As an extreme illustration of this point, consider the case of the robot pushing the tissue until it is fully restrained from moving. Tracking the stationary position of the tissue in this case would not have the desired effect from motion compensation.

A force control approach is more appropriate when attempting to manipulate beating heart tissue. Previous work on surgical force control has largely focused on force feedback for teleoperation of surgical instruments and robots (reviewed in [50]). Force feedback has demonstrated a number of performance benefits in the execution of remote surgical tasks [55, 38, 69] and can enhance safety when used to implement virtual workspace limits [28, 67]. In this setting, the primary role of the force controller is to provide haptic information to the user while the user commands the robot to interact with the surgical target.

In contrast, beating heart applications require the robot controller to autonomously maintain prescribed forces of the instrument against the target tissue despite its fast motion. One major concern is safety, given the well-documented occurrence of instability in force control [72, 16, 17, 2, 13]. A robotic system for beating heart surgery must be damped and stable to ensure that it will not overshoot or oscillate in response to changes in the desired force trajectory or sudden target motions. Furthermore, the system must have sufficient bandwidth to reject the disturbance caused by heart motion. Previous research indicates that standard force control strategies can only achieve stability for low closed-loop bandwidths due to vibratory modes in the robot structure [16, 17, 2, 13]. These findings were obtained in the context of large industrial robots interacting with stiff targets. To ensure adequate robot performance and
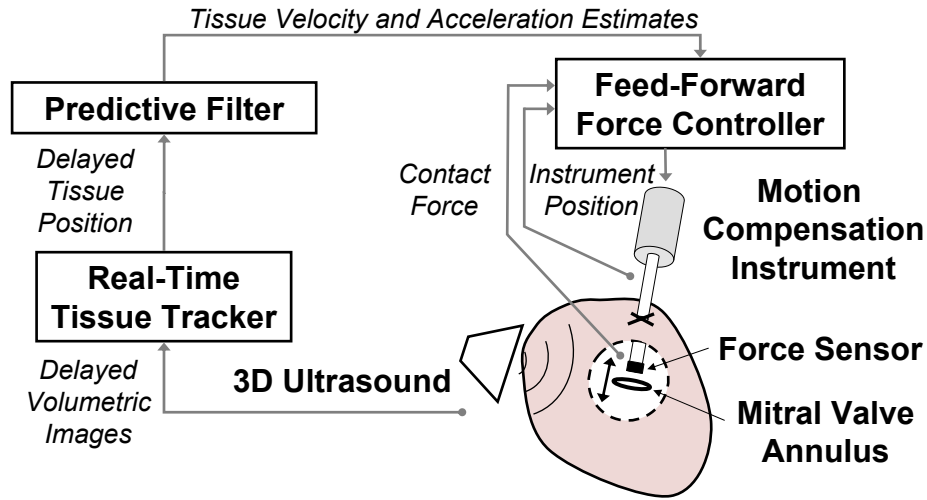
Figure 4.1: The surgical system actuates an instrument to apply precise forces against beating heart structures. The controller uses both force measurements and feed-forward tissue motion estimates that are derived from a 3D ultrasound tissue tracker and predictive filter.

safety, it is essential to determine whether the same limitations exist in beating heart surgery where the target is soft but rapidly moving.

In this chapter, we study force control in the context of beating heart surgery and find that the standard force controller does indeed suffer from bandwidth restrictions due to the vibratory modes present in long surgical instruments. However, by incorporating feed-forward tissue motion information into the controller, safe and accurate force tracking can be achieved at low bandwidth. In the first part of this chapter we show that simultaneously achieving an adequately damped system with good disturbance rejection is challenging because it requires a closed-loop bandwidth that would excite undesired vibratory modes in the robot. Subsequently, we describe a force tracking system that bypasses these bandwidth limitations by using feed-forward heart motion information derived from 3D ultrasound to augment the controller. The system, shown in Figure 4.1, is adapted for beating heart mitral valve
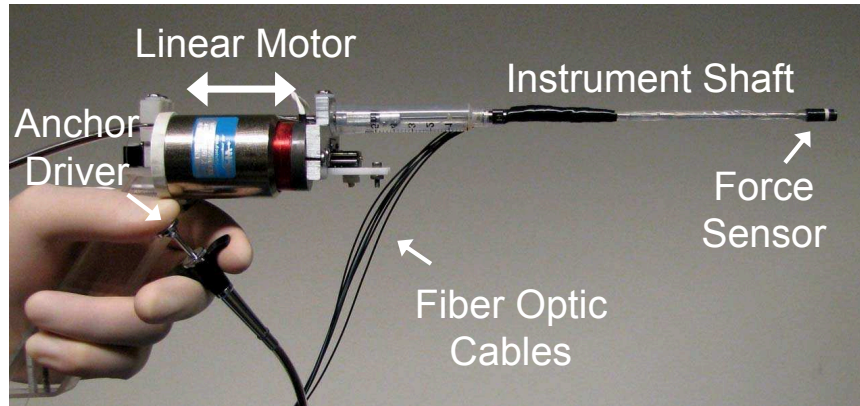
Figure 4.2: The motion compensation instrument (MCI) is a handheld surgical anchor deployment device. It is actuated in one degree of freedom to cancel the dominant 1D motion component of the mitral valve annulus. A tip-mounted optical force sensor [74] measures contact forces against beating heart tissue.

annuloplasty. It uses the motion compensation instrument (MCI) from Chapter 3 that can follow the rapid, nearly uniaxial motion of the mitral valve annulus. An optical force sensor [74] is integrated into the tip of the instrument (Figure 4.2) to provide measurements of the interaction forces with the surgical target. We validate the system and demonstrate its utility to the surgeon in an *in vivo* experiment in a large animal model.

4.1   Rigid Body Analysis

To gain some insight into the use of force control in beating heart surgery, we first consider the case of a perfectly rigid robotic instrument. The robot is modeled as a mass m and damper b subjected to a commanded actuator force f_a and environment contact force f_e. The damper b captures the effects of friction in the robot, friction at the insertion point to the heart, and fluid motion. Approximating the environment
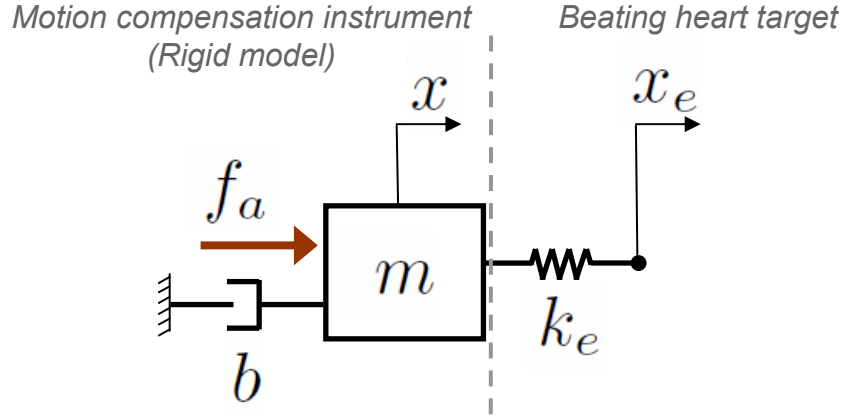
Figure 4.3: Rigid body robot model in contact with an actively moving, compliant environment.

as a spring of stiffness k_e yields the system dynamics

$$m\ddot{x} + b\dot{x} = f_a - k_e(x - x_e), \tag{4.1}$$

where x is the instrument tip position and x_e is the desired tissue target position (i.e., its position if it were not deformed by contact). The model is illustrated in Figure 4.3. For simplicity, we neglect force sensor compliance in the model because it is significantly stiffer than the tissue environment.

Now consider a standard force regulator control law [58]

$$f_a = f_d + K_f(f_d - f_e) - K_v\dot{x}, \tag{4.2}$$

where K_f and K_v are controller gains and f_d is the desired force. Combining Equations 4.1 and 4.2 and applying the Laplace transform gives the closed-loop contact force relationship

$$F_e(s) = \boldsymbol{T}(s)F_d(s) + \boldsymbol{Z}(s)X_e(s), \tag{4.3}$$

where the force tracking transfer function $\boldsymbol{T}(s)$ and robot impedance transfer function

$\boldsymbol{Z}(s)$ are

$$\boldsymbol{T}(s) \triangleq \frac{F_e(s)}{F_d(s)} = \frac{\frac{k_e}{m}(1 + K_f)}{C(s)}, \tag{4.4}$$

$$\boldsymbol{Z}(s) \triangleq \frac{F_e(s)}{X_e(s)} = -\frac{k_e s(s + \frac{K_v + b}{m})}{C(s)}, \tag{4.5}$$

$$C(s) = s^2 + \frac{K_v + b}{m}s + \frac{k_e}{m}(1 + K_f). \tag{4.6}$$

Equation 4.3 makes explicit that the target motion x_e is a disturbance that perturbs f_e from f_d.

Controller gains K_f and K_v are chosen to ensure system stability, sufficient damping, and good rejection of x_e. The last is achieved by designing $\boldsymbol{Z}(s)$ to have small magnitude in the bandwidth of $X_e(s)$. For the mitral valve annulus, which is essentially bandlimited to approximately 15 Hz (Figure 2.3), this is equivalent to setting the impedance corner frequency f_z greater than or equal to 15 Hz. Figure 4.4 depicts typical mitral valve annulus motion and its effect on the contact force for various f_z based on simulations of Equations 4.3–4.5 with $f_d = 0$. Parameter values of $m = 0.27$ kg, $b = 18.0$ Ns/m, and $k_e = 133$ N/m are assumed based on system identification of the MCI and preliminary estimates of the mitral valve annulus stiffness. As will be shown shortly, obtaining a large impedance corner frequency f_z is synonymous with increasing the natural frequency f_n of the closed-loop system, which is also equivalent to increasing K_f.

First, using second order system design techniques [49] on the characteristic equation in Equation 4.6 gives the natural frequency f_n and damping ζ of the system
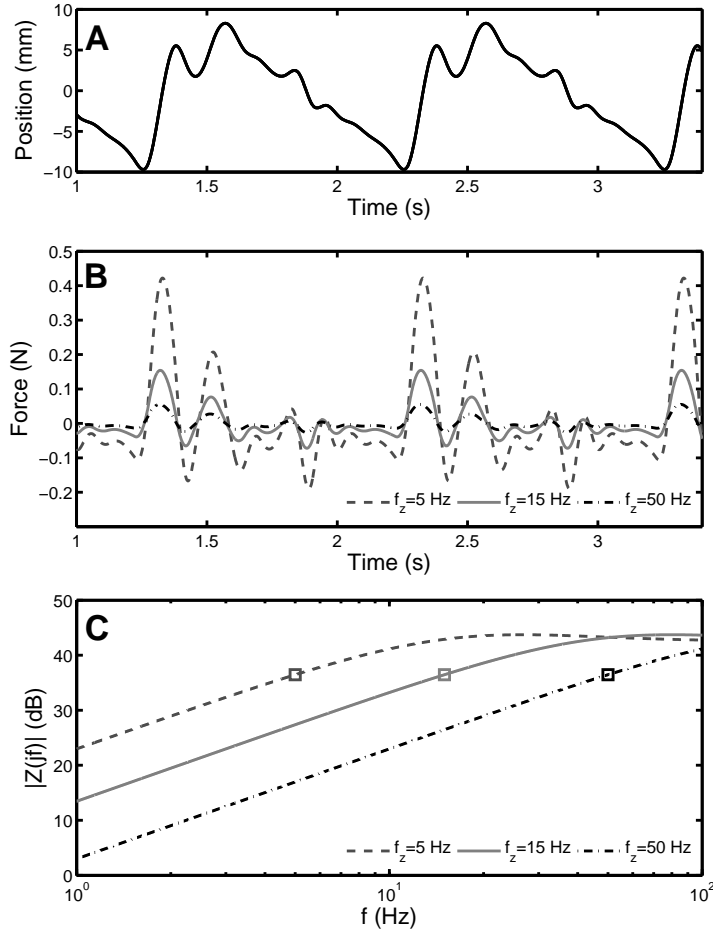
Figure 4.4: The effect of mitral valve annulus motion on contact forces. Human mitral valve annulus trajectory (A) and corresponding force disturbances for f_z of 5, 15, and 50 Hz (B). The magnitude plots of the impedance transfer function $|\boldsymbol{Z}(jf)|$ are shown with corner frequencies marked by squares (C). Gain settings are $K_f = 27.5$, $K_v = 45.9$ for $f_z = 5$ Hz; $K_f = 255.2$, $K_v = 173.8$ for $f_z = 10$ Hz; and $K_f = 2845.7$, $K_v = 621.4$ for $f_z = 50$ Hz. Mitral valve annulus motion data is repeated from Chapter 2.

as

$$f_n = \frac{1}{2\pi}\sqrt{\frac{k_e}{m}(1 + K_f)}, \tag{4.7}$$

$$\zeta = \frac{K_v + b}{4\pi m f_n}. \tag{4.8}$$

To avoid potentially dangerous overshoot, we set the system to be critically damped ($\zeta =$

1.0) and manipulate Equations 4.5, 4.7, and 4.8 to show that for any impedance trans-
fer function of the form

$$\boldsymbol{Z}(s) \propto \frac{s(s + 4\pi f_n)}{s^2 + 4\pi f_n s + (2\pi f_n)^2} \tag{4.9}$$

the natural frequency f_n is a function of the impedance corner frequency f_z by

$$f_n = \left(\frac{\sqrt{208} - 14}{6}\right)^{-\frac{1}{2}} f_z \approx 3.7698 f_z. \tag{4.10}$$

Hence, while a position regulator can follow a trajectory bandlimited to 15 Hz with
about the same closed-loop natural frequency, a force regulator must have a natural
frequency of approximately 57 Hz to follow the same motion. This indicates that the
force regulator inherently requires high bandwidth to compensate for target motion.

Figure 4.5 shows the system damping and impedance corner frequency over a
range of values for K_f and K_v. It is clear that there is a trade-off between the
two performance criteria: increasing K_f increases the corner frequency but decreases
damping; the opposite is true for K_v. Because of this trade-off, achieving suitable
disturbance rejection ($f_z \geq 15$ Hz) while maintaining damping ($\zeta \geq 1$) requires
large gains. From Equations 4.7–4.10 we calculate gain settings of $K_f = 255.2$ and
$K_v = 173.8$ to set the system to be critically damped with $f_z = 15$ Hz, assuming that
the rigid body model is appropriate at such high gains.

4.2   Bandwidth Contraints due to Robot Dynamics

In this section, we study the effect of high gains on robot performance. Extensive
prior work on force control has delineated a number of instabilities that can arise in
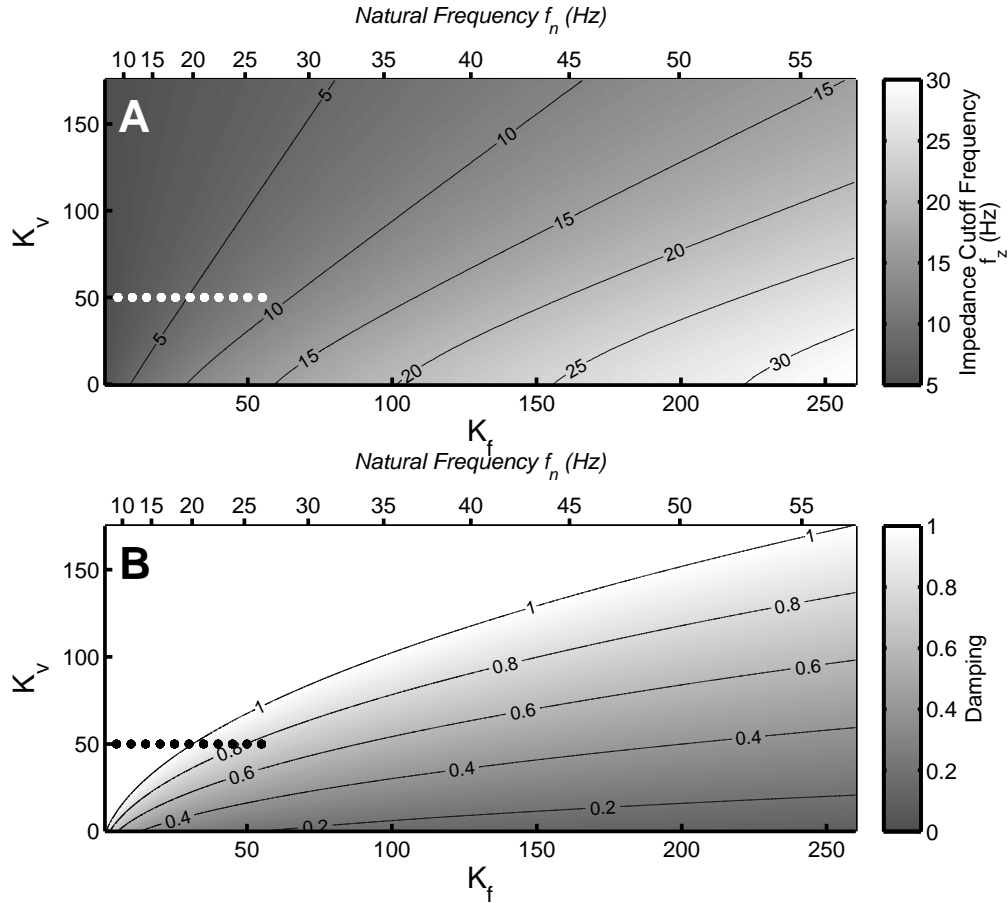
Figure 4.5: Impedance corner frequency f_z (A) and damping ζ (B) over different values of K_f and K_v using a rigid body model of the MCI. A trade-off exists between damping and disturbance rejection. The model suggests that simultaneously achieving good damping ($\zeta \geq 1$) and disturbance rejection ($f_z \geq 15$ Hz) can be obtained at high gains. The natural frequency f_n, which is related to K_f through Equation 4.7, is also shown. Dots indicate the gain test points used for laboratory tests in Section 4.2.2.

attempting to control forces using multiple degree of freedom robot arms in contact with hard surfaces [16, 17, 2, 13]. In particular, force controllers can excite structural modes in the manipulator, leading to high amplitude force transients at the end effector. These mechanisms do not pertain to this surgical application, where the end effectors tend to be long, rod-like instruments in order to reach patient anatomy

through small ports, and tissues are highly compliant.

It is well known, however, that axial motion of such long rods excites transverse vibrations [31]. The dynamics describing this motion are nonlinear and have time varying parameters, but for the purposes of developing effective force controllers it is not necessary to model these dynamics: we need only to determine the frequency at which they become significant so that reasonable bandwidth restrictions can be imposed on the rigid body model and closed-loop system analysis of the preceding section. While structural resonance can be used to enhance performance in some situations, it is typically avoided because inadvertent excitation of the resonance can destabilize the controller, reduce the positional accuracy of the instrument, and cause undue wear to the robot. In the present application, resonance can further cause injury to the patient from the transmission of vibrational energy to the tissue in contact with the robot.

In the following section, we analytically and empirically demonstrate that vibration precludes the use of the high gain force regulator suggested in Figure 4.5. We first demonstrate that vibration occurs at relatively low frequency for surgical robots with long instruments. Subsequently, we empirically demonstrate that these vibrations are significant in the motion compensation system and can lead to instability as K_f is increased until the natural frequency approaches the resonance of the instrument.

4.2.1 Gain Limit to Avoid Vibration

Consider a cylindrical rod of length l and radius r undergoing axial motion while compressed by a force f_e (Figure 4.6). At low velocities, the fundamental mode of
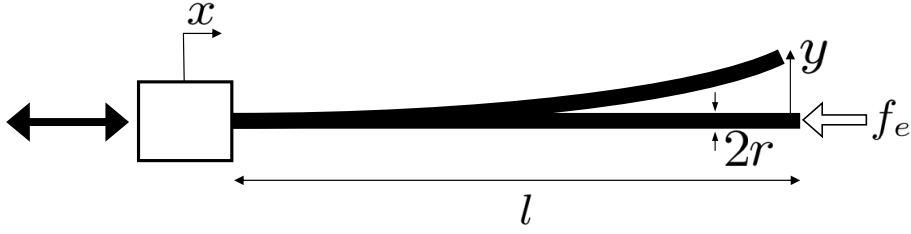
Figure 4.6: Axially oscillating cantilevered rod of length l and radius r. Lateral motion at the base of the rod (x) excites transverse vibrations (y) [31].

transverse vibration occurs at frequency

$$f_1 = \frac{3.5156}{4\pi} \sqrt{\frac{E}{\rho} \left(1 - f_e \frac{4l^2}{E\pi^3 r^4} \right)} \left(\frac{r}{l^2} \right), \qquad (4.11)$$

where E and ρ are respectively the Young's modulus and density of the material making up the rod [7]. At large velocities the fundamental frequency is time varying [31]; however, we omit this phenomena for ease of analysis. The compressive loads expected in heart surgery are significantly less than the Euler buckling load (i.e., $f_e << \frac{E\pi^3 r^4}{4l^2}$), so Equation 4.11 is well approximated by

$$f_1 \approx \frac{3.5156}{4\pi} \sqrt{\frac{E}{\rho}} \left(\frac{r}{l^2} \right), \qquad (4.12)$$

which is the fundamental vibration frequency of an unloaded cantilevered rod [71].

The closed-loop natural frequency of the system should be set lower than the first resonance (i.e., $f_n < f_1$) in order to avoid the effects of vibration. Combining Equations 4.7 and 4.12 provides a limit on the proportional gain

$$K_f^{\text{limit}} = \frac{m}{k_e} \left(\frac{3.5156^2 E}{4\rho} \frac{r^2}{l^4} \right) - 1. \qquad (4.13)$$

Choosing $K_f = K_f^{\text{limit}}$ would set the natural frequency equal to the resonance frequency, which is not desirable. In practice, the value of K_f should be chosen substan-

tially lower than K_f^{limit} so that the gain of the closed-loop system is small through the spectral extent of the resonance.

The MCI is mounted with a stainless steel 14 gauge blunt needle ($E = 200$ GPa, $\rho = 7900$ kg/m^3, $r = 1.1$ mm) with an inner stainless steel push rod used for anchor deployment in mitral valve annuloplasty [68, 65, 66]. Its length is $l = 22.8$ cm[1]. For simplicity we approximate the entire structure as a solid cylindrical rod. Assuming the same system parameters as before, Equations 4.12 and 4.13 predict that the fundamental resonance occurs at $f_1 = 27.6$ Hz and the limit on the proportional gain is $K_f^{\text{limit}} = 60.4$. Referring to the rigid body performance plots in Figure 4.5, it is clear that the controller gains cannot be set high enough to simultaneously avoid resonance and meet the criteria of a damped system with high bandwidth.

Because K_f^{limit} increases quadratically with r, increasing the radius of the instrument substantially would permit high gain without exciting vibration. However, for minimally invasive surgical procedures, the instrument width should be kept small in order to minimize the sizes of the ports into the thorax and heart. Clincal researchers have also found that the sizes of standard robotic instruments (2.5 mm $\leq r \leq 5.5$ mm) are a limiting factor in accessing and manipulating mitral valve anatomy [39, 19]. LaPietra *et al.* found that thinner robotic instruments ($r = 1.9$ mm) improved access in stopped-heart mitral valve annuloplasties performed in a canine model [39]. Figure 4.7 depicts f_1 and K_f^{limit} over a range of r for the system.

---

[1]Preliminary animal testing found this to be the minimum length necessary for the instrument to access the mitral valve during beating heart procedures in a porcine model. The instrument approach was from the left atrial appendage through the second intercostal space in a left thoracotomy.
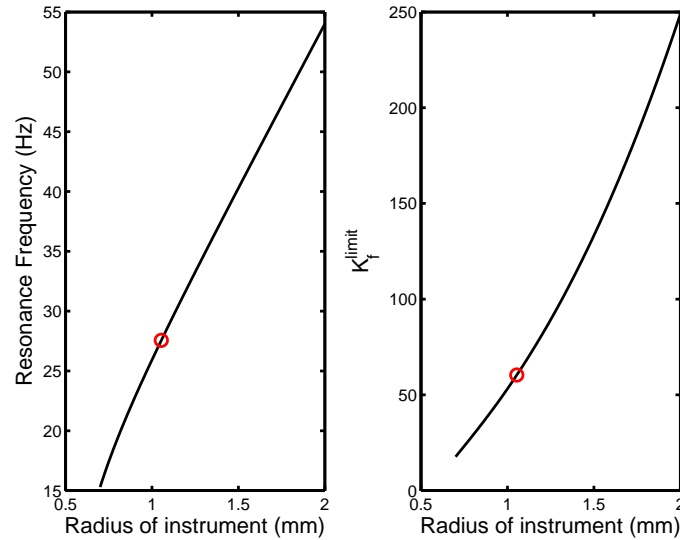
Figure 4.7: Transverse vibration limits the maximum allowable proportional gain K_f. The resonance frequency f_1 (A) and resulting upper limit K_f^{limit} (B) are shown over the radius of the instrument r. The values corresponding to a 14 gauge needle like that mounted on the MCI are indicated with circles. The instrument is assumed to be steel ($E = 200$ GPa, $\rho = 7900$ kg/m^3) with length $l = 22.8$ cm. All other parameters are the same as before.

4.2.2 Experimentally Observed Vibration and Instability

Although avoiding vibratory motion in a surgical robot is intuitively appealing, it remains unclear if such motion is severe enough to present a problem in beating heart surgery. Here we experimentally demonstrate that these vibrations can affect the accuracy of the instrument tip position and also lead to unstable behavior. We furthermore validate Equations 4.12 and 4.13 for predicting the fundamental resonance frequency and gain limit K_f^{limit}, respectively.

Characterization of Transverse Vibration Over Frequency

The MCI was positioned horizontally and clamped along its base to restrict vibrations to only the instrument shaft. The instrument was commanded to follow axial, sinusoidal motion inputs at frequencies between one and 100 Hz. The axial position of the actuator was measured by a high linearity potentiometer (CLP13-50, P3 America, San Diego, CA, USA) at 1 kHz. Transverse vibration of the instrument tip was imaged by a digital camera (EOS 20D, Canon, Tokyo, Japan) with 200 ms exposure time. Vibration amplitudes were measured by a scale placed in the image and oriented to the plane of motion. Figure 4.8A shows the setup with the MCI stationary.

Figure 4.8B–F depicts the transverse vibrations observed at 10, 20, 27, 30, and 40 Hz. Large transverse motions are apparent at 27 Hz. Figure 4.9 shows the magnitude of the transverse displacement normalized by the magnitude of the axial displacement over frequency. The resonance frequency occurs at 27 Hz, in agreement with the predicted value from Section 4.2.1. The resonance peaks to a value of 9.8 dB and its effect becomes small at approximately 22.2 Hz. Vibration for inputs with frequencies below 10 Hz and from 50–100 Hz were negligible.

Excitation of the observed resonance would not be safe for beating heart surgery. For context, the mitral valve annulus is a ring of smooth tissue with an approximate width of a few millimeters. Vibration while in contact with the annulus could cause the instrument to slip into the mitral valve or adjacent cardiac structures. Contact with tissue could dampen the vibratory motion but this would also transfer the vibrational energy to the patient anatomy and could cause significant injury.
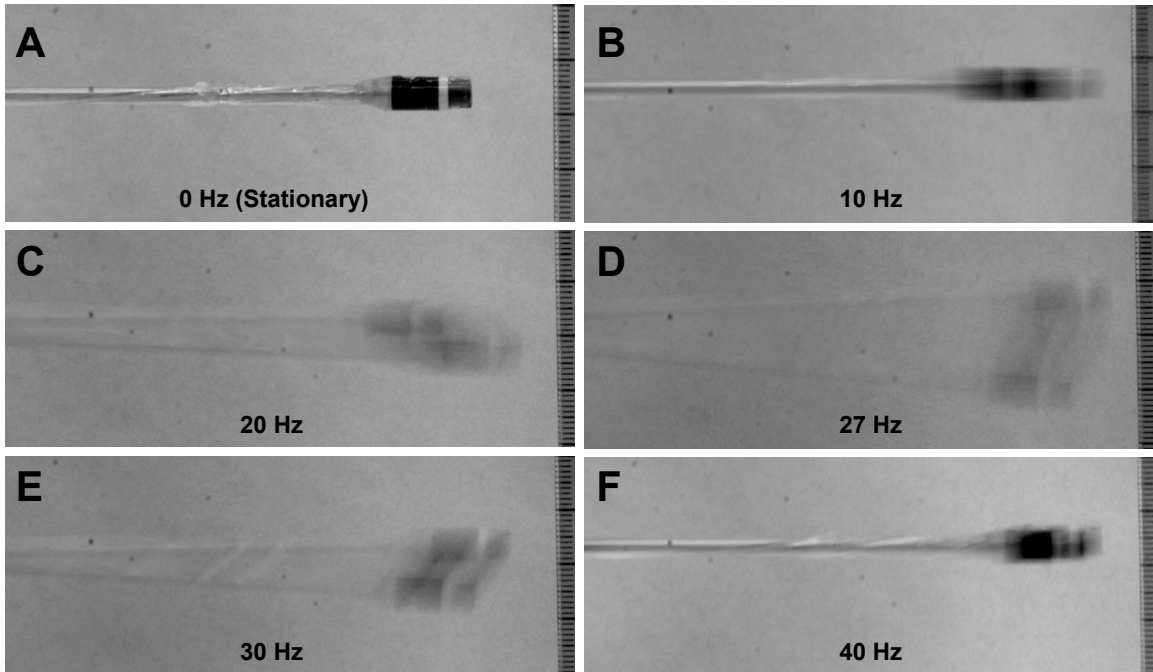
Figure 4.8: Instrument with force sensor at rest (A) and vibrating due to an axial, sinusoidal motion at 10 Hz (B), 20 Hz (C), 27 Hz (D), 30 Hz (E), and 40 Hz (F) imposed at the base of the instrument shaft. Transverse vibration is maximal at 27 Hz, the predicted resonance frequency from Section 4.2.1. Exposure times are 200 ms. Scale marks at right are in millimeter.

Force Regulator Instability at High Gain

In this experiment we study the effect of vibration on stability by testing increasing values of K_f that approach the predicted $K_f^{\text{limit}} = 60.4$ from Section 4.2.1. This is equivalent to testing the system at increasing natural frequencies that approach the 27 Hz resonance of the MCI.

As before, the MCI was positioned horizontally on a flat surface and clamped along its body to restrict vibrations to only the instrument shaft. The instrument tip was placed in series with a steel leaf spring with a stiffness matched to the approximate stiffness of the mitral valve annulus ($k_e = 133$ N/m). The desired force f_d was a unit
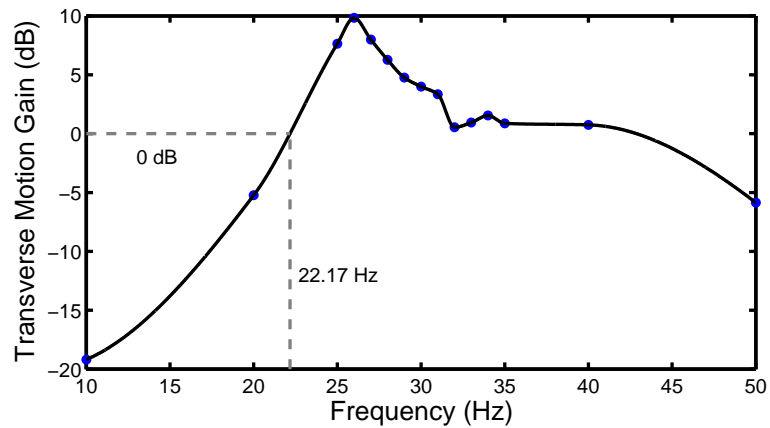
Figure 4.9: Magnitude of transverse displacement normalized by the magnitude of the axial displacement (y and x, respectively, as shown in Figure 4.6). As predicted in Section 4.2.1, the resonance occurs at 27 Hz. The estimated 0 dB frequency is marked.
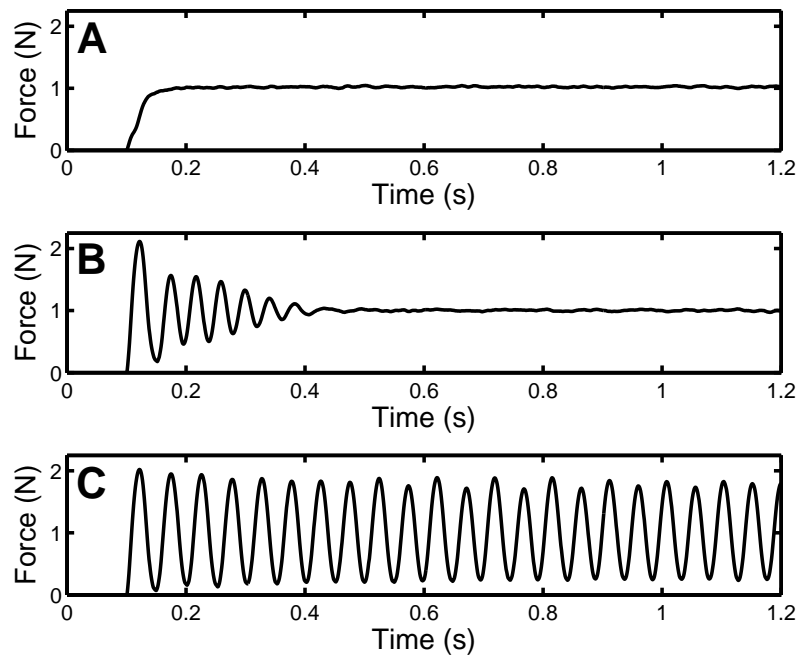
Figure 4.10: Stable and unstable step response examples: $K_f = 5$ and stable (A); $K_f = 40$ and stable but underdamped (B); $K_f = 50$ and unstable (C).
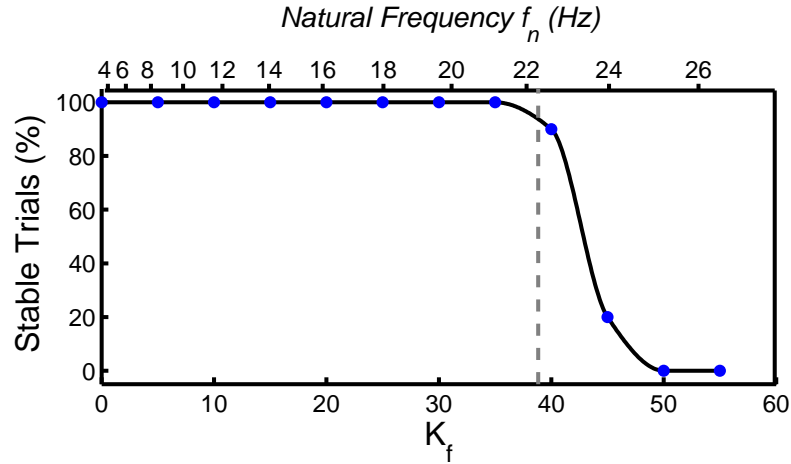
Figure 4.11: Stability over increasing proportional gain K_f. Percentage is taken over 10 trials for each value of K_f. The natural frequency f_n, which is related to K_f through Equation 4.7), is also shown. The 0 dB corner frequency of the resonance (Figure 4.9) is marked with a dashed line and coincides with the onset of instability in the controller.

step and the MCI was controlled by the force regulator law in Equation 4.2. Gain values for K_f ranged from zero to 55 in steps of five and K_v was fixed at 50. These gain values are marked in Figure 4.5 to illustrate their locations in the controller design space for a rigid robot. Ten trials were performed for each gain setting for a total of 120 trials. Controller performance was judged to be stable or unstable for each trial, with the latter criteria defined as exhibiting non-decaying oscillations in excess of 50% overshoot for more than one second after the unit step input.

Examples of stable and unstable trials are shown in Figure 4.10 for three choices of K_f. Figure 4.11 gives the percentage of stable trials over K_f. As expected, increasing the gain reduces damping and eventually leads to unstable behavior. Instability first arises for 10% of the trials at $K_f = 40$, which corresponds to a closed-loop natural frequency of $f_n = 22.6$ Hz and is nearly coincident with the location of the 0 dB

corner frequency for the observed resonance (Figure 4.9). Increasing K_f to 50 and above leads to 100% of the trials being unstable. This is less than the predicted upper bound of $K_f^{\text{limit}} = 60.4$ but is nonetheless expected because of the spectral width of the resonance seen in Figure 4.9. Overall, these results suggest that exciting vibrational modes in even a single degree of freedom robot can lead to an unstable, unsafe controller.

4.3 Force Control with Feed-Forward Target Motion

The preceding sections indicate that vibrational modes in surgical instruments prevent the high gain settings required for a force regulator to obtain both damping and good heart motion rejection. Rather than use a pure force error feedback control strategy, an alternative strategy employs feed-forward target motion information in the controller. Previous work has shown that this approach can improve force tracking when dealing with moving or uneven surfaces [56, 33]. This approach is well suited to beating heart applications because accurate predictions of heart motion can be obtained by exploiting its periodicity [62, 51, 24, 6, 21].

Consider the control law

$$f_a = f_d + K_f(f_d - f_e) + K_v(\hat{\dot{x}}_e - \dot{x}) + b\hat{\dot{x}}_e + m\hat{\ddot{x}}_e, \tag{4.14}$$

which is Equation 4.2 augmented with feed-forward estimates of the target velocity $\hat{\dot{x}}_e$ and acceleration $\hat{\ddot{x}}_e$. The contact force relationship in Equation 4.3 becomes

$$F_e(s) = \boldsymbol{T}(s)F_d(s) - \boldsymbol{Z}(s)\left(X_e(s) - \hat{X}_e(s)\right),$$

where $\boldsymbol{T}(s)$ and $\boldsymbol{Z}(s)$ are defined as before in Equations 4.4 and 4.5, respectively. Observe that the use of feed-forward terms $\hat{\dot{x}}_e$ and $\hat{\ddot{x}}_e$ enable the cancellation of the motion disturbance x_e without the need to greatly increase the natural frequency of the system. The controller can then be designed with a low closed-loop natural frequency to avoid the effects of vibration and other high order dynamics that lead to reduced damping and instability. The feed-forward bandwidth is set equal to the bandwidth of the heart motion disturbance, which is lower than the resonance frequency of the robot.

4.4   Tissue Motion Estimation with 3D Ultrasound

To obtain the motion terms needed in the feed-forward controller, we first determine the position of the tissue in 3D ultrasound using the real-time tissue segmentation algorithm from Chapter 3. The algorithm takes advantage of the high spatial coherence of the instrument, which appears as a bright and straight object in the volume, to designate the tissue target. Figure 4.12 depicts using this method to track a point on the mitral valve annulus in a beating porcine heart.

As in the previous chapters, we model the nearly uniaxial motion of the mitral valve annulus as a time-varying Fourier series with an offset and truncated to m harmonics (Equation 2.5). For clarity, we repeat the motion model using the notation of this chapter:

$$x_e(t) = c(t) + \sum_{i=1}^{m} r_i(t) \sin(\theta_i(t)),$$

where $c(t)$ is the offset, $r_i(t)$ are the harmonic amplitudes, and $\theta_i(t) \triangleq i \int_0^t \omega(\tau) d\tau + \phi_i(t)$, with heart rate $\omega(t)$ and harmonic phases $\phi_i(t)$. Prior to contact, measure-
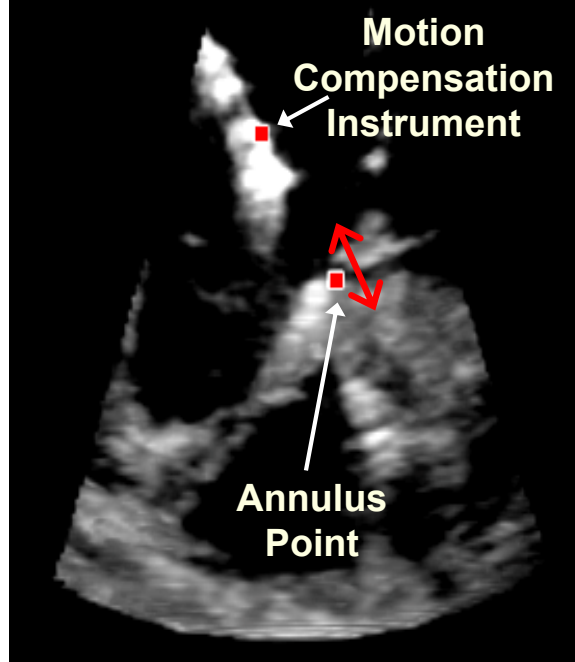
Figure 4.12: Slice through real-time 3D ultrasound volume showing tissue tracking. Squares denote the instrument with tip-mounted force sensor and the surgical target located on the mitral valve annulus.

ments from the tissue tracker are used to train an extended Kalman filter to provide estimates of the model parameters $\hat{c}(t)$, $\hat{r}_i(t)$, $\hat{\omega}(t)$, and $\hat{\theta}_i(t)$. These parameters are used to generate smooth feed-forward velocity and acceleration terms for the force controller of Equation 4.14 using the derivative equations

$$
\begin{aligned}
\hat{\dot{x}}_e(t) &= \sum_{i=1}^{m} \hat{r}_i(t) i\hat{\omega}(t) \cos(\hat{\theta}_i(t)), \\
\hat{\ddot{x}}_e(t) &= -\sum_{i=1}^{m} \hat{r}_i(t) (i\hat{\omega}(t))^2 \sin(\hat{\theta}_i(t)).
\end{aligned}
$$

After contact, updates to the filter are stopped because the robot interacts with the tissue, causing subsequent position measurements to no longer be representative of the feed-forward (i.e., desired) tissue motion trajectory.
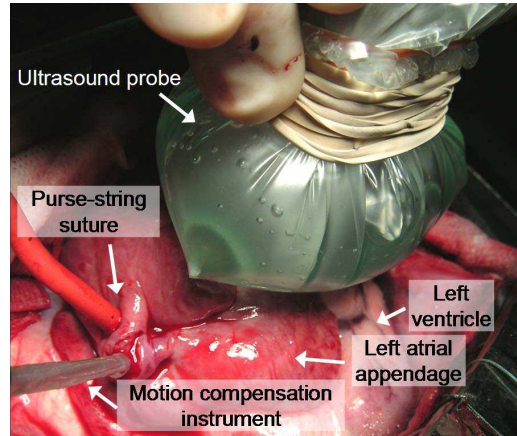
Figure 4.13: *In vivo* experiment setup.

4.5   *In Vivo* System Validation

4.5.1   Experimental Setup

In vivo validation of the system was performed in a beating heart Yorkshire pig model (Figure 4.13). The tip of the MCI was inserted into the left atrial appendage and secured by a purse-string suture. The 3D ultrasound probe (SONOS 7500, Philips Healthcare, Andover, MA, USA) was positioned epicardially on the free wall of the left ventricle to image the mitral valve and instrument. The surgeon was instructed to hold the instrument tip against the mitral valve annulus with a constant 2.5 N force for approximately 30 s. This task was performed under three conditions: manually (i.e., using a fixed instrument with no robot control), using the force regulator in Equation 4.2, and using the feed-forward force controller in Equation 4.14. Contact forces were visually displayed to the surgeon during the task and recorded for offline assessment. Three trials were attempted for each condition. The experimental protocol was approved by the Children's Hospital Boston Institutional Animal Care

and Use Committee. The animal received humane care in accordance with the 1996 *Guide for the Care and Use of Laboratory Animals*, recommended by the US National Institute of Health.

In all force controlled trials, the controller gains were designed for $\zeta = 1.05$, $f_n = 8$ Hz ($K_f = 4.1$ and $K_v = 10.5$) based on parameter values $m = 0.27$ kg, $b = 18.0$ Ns/m, and $k_e = 133.0$ N/m. The gains were left intentionally low to guarantee controller stability in the unstructured environment of the operating room where off-axis loading could result in instrument bending, as well as to account for uncertainty and variability in heart stiffness. The elastic properties of the heart can vary by a factor of three from patient to patient in normal human hearts and hearts afflicted with congestive cardiomyopathy are on average five times stiffer than the average healthy heart [42].

The force tracking system uses a dual CPU AMD Opteron 285 2.6 GHz PC with 4 GB of RAM to process the ultrasound data and control the MCI. The 3D ultrasound machine streams volumes at 28 Hz to the PC over a 1 Gb LAN using TCP/IP. A program written in C++ retrieves the ultrasound volumes and loads them onto a GPU (7800GT, nVidia Corp, Santa Clara, CA, USA) for real-time beating heart tissue segmentation. This provides tissue position measurements that are used to train the extended Kalman filter. After 5 s of initialization, the filter outputs estimates of the tissue velocity and acceleration. These are used in tandem with force measurements from a custom, tip-mounted optical force sensor (0.17 N RMS error, described in [74]) according to the control law in Equation 4.14 in a 1 kHz servo loop. The MCI is powered by a linear power amplifier (BOP36-1.5 M, Kepco, Flushing, NY, USA).
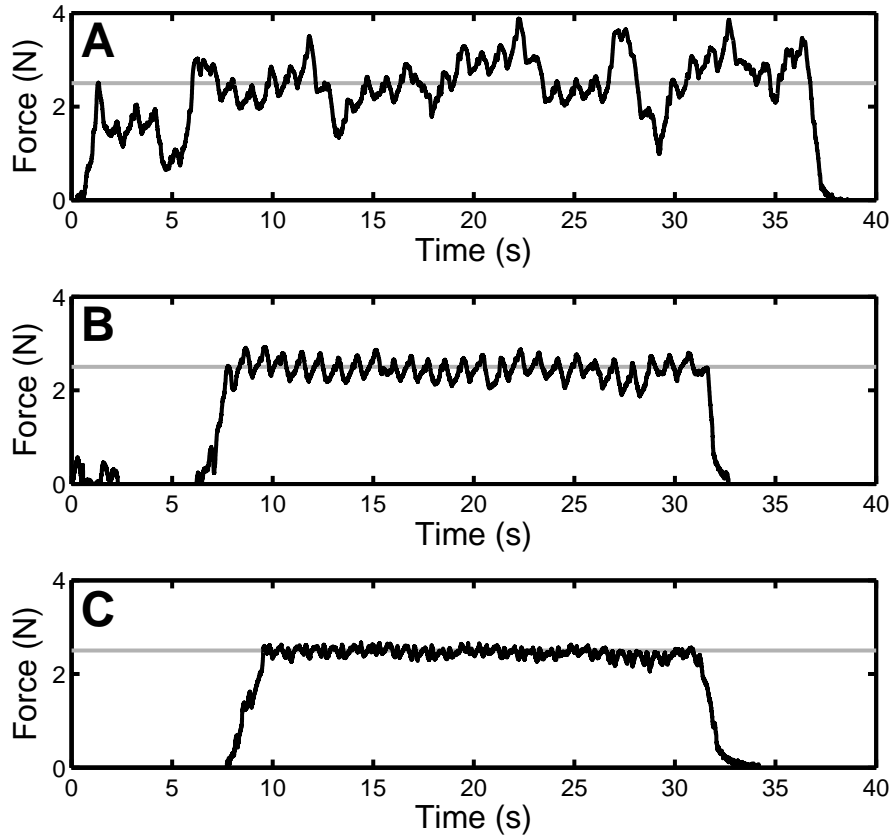
Figure 4.14: Example contact force records for manual (A), force regulator (B), and feed-forward force control (C) test conditions. The desired contact force of 2.5 N is indicated (horizontal line). Data was drawn from the trials with the lowest standard deviations.

4.5.2 Results

Figure 4.14 provides example force traces for the task executed manually, with the force regulator, and with the feed-forward force controller. Averaged across all trials, manual contact with the annulus yielded force standard deviations of 0.48 ± 0.06 N (mean $\pm$ std error). The force regulator reduced these deviations to 0.22 ± 0.01 N with clear statistical significance in a two-sided t-test ($p = 0.012$). The feed-
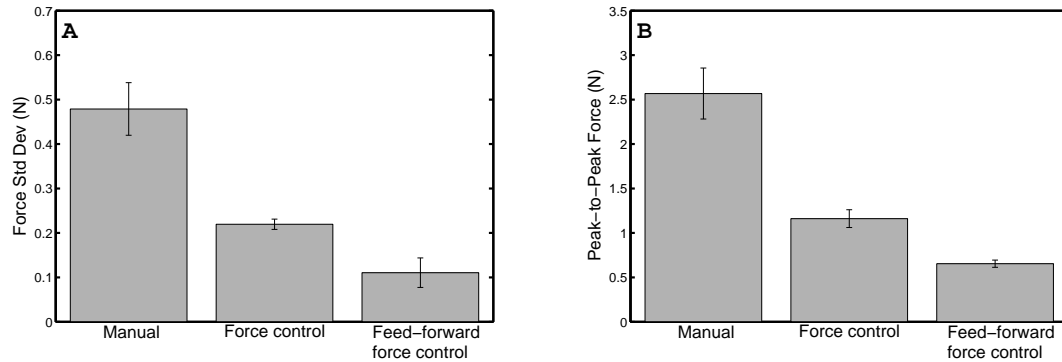
Figure 4.15: Disturbance rejection measured by standard deviation of forces (A) and peak-to-peak forces (B). Mean ± std error is shown.

forward force controller reduced the deviations to approximately 25% of the manual case (0.11 ± 0.02 N, $p = 0.017$). Statistical significance was also found between the force regulator and feed-forward controller conditions ($p = 0.009$). These results are summarized in Figure 4.15A. The third trial for the feed-forward force controller is omitted because the animal showed reduced cardiac viability at the end of the experiment. Performance was nearly equal to the standard force controller in this trial.

The force regulator and feed-forward force controller also reduced peak-to-peak forces (Figure 4.15B). Manual use of the instrument gave swings in the contact force of 2.57 ± 0.29 N. The force regulator and feed-forward force controller reduced these values to 1.16 ± 0.10 N and 0.65 ± 0.04 N, respectively. Statistical significance was found between all conditions at $p < 0.05$.

4.6   Discussion

The results from this *in vivo* experiment underscore the benefit of a force controlled robot in beating heart procedures. Without force control, placement of the instrument against the mitral valve annulus gave peak-to-peak force swings of 2.57 N, which is unacceptable compared to the desired 2.5 N force set point. The standard force regulator reduced this fluctuation by 50% and the feed-forward controller reduced it by another 50%. In the case of the feed-forward controller, the precision of the contact forces was 0.11 N. In all of the force controlled experiments, the surgeon expressed greater confidence in instrument manipulation against the beating mitral valve annulus, with the feed-forward controller subjectively better than the standard force regulator. These findings suggest that robotic force control may be an effective aid to the surgeon for beating heart mitral annuloplasty. We note, however, that a potential limitation of the current study is that manual tasks were done with a (nonactuated) motion compensation instrument, which is heavier than typical surgical tools.

The *in vivo* results also verify that safe, precise robotic force tracking is feasible inside of the beating heart through the use of feed-forward target motion information in the controller. This approach enables the robotic system to operate at the motion bandwidth of the heart while simultaneously ensuring damping and providing good disturbance rejection. In contrast, a purely force feedback controller would require a bandwidth approximately 3.8 times higher than the heart motion bandwidth to have the same performance. The analysis and laboratory experiments of this chapter indicate that force control at such high bandwidth excites transverse vibrations in

the robot that could lead to a variety of dangerous outcomes, including controller instability.

The difficulty in achieving a fast and stable force controller has been examined extensively by other researchers, typically in the industrial setting where large, multiple degree of freedom robots interact with stiff, nearly motionless surfaces. Their analyses found a number of fundamental sources for instability at high bandwidth such as sampling time [72], actuator bandwidth limitations [17], force measurement filtering [17], actuator and transmission dynamics [13], and flexible modes in the robot arm [16, 2, 13]. Recent *in vivo* force control experiments using a multiple degree of freedom endoscopic robot in contact with liver indicate that arm dynamics can limit controller bandwidth to the extent that it is not able to adequately reject slow respiratory motion [75, 9]. For our system and application, the dominant source of instability is from the flexible modes in the surgical instrument. This is somewhat surprising given the simplicity of the robot: basically a small, one degree of freedom actuator mounted with a stiff, nonarticulated rod as an end effector. However, the analysis and experiments of Section 4.2 confirm that these resonances should and do occur in the robot and are also likely to occur in the instruments mounted to standard surgical robots.

To overcome the bandwidth limitations imposed by vibration, we developed a system that exploits the quasiperiodicity in heart motion to generate feed-forward motion terms for the force controller. Similar approaches have been used for robotic position tracking of the beating heart. Independently, Ginhoux *et al.* [24] and Bebek and Cavusolgu [6] demonstrated that the use of model predictive control can increase

the effective tracking bandwidth and positioning accuracy of their multiple degree of freedom robots for coronary artery bypass graft procedures. The work in Chapters 2 and 3 showed that heart motion prediction could be used to compensate for the time delays and noise inherent in 3D ultrasound-guided, robotic intracardiac procedures. All of these studies have demonstrated the *in vivo* feasibility of accurately positioning a robotic instrument relative to a beating heart surgical target. This chapter addresses the successive problem of tracking the heart while applying precise contact forces for surgical manipulation. This is pursued from the perspective of force control, and the *in vivo* experiment shown here is the first demonstration of such an approach within the beating heart.

There are alternatives to the approach of feeding-forward target motion in order to avoid vibration at high bandwidth. For instance, one could attempt to structurally reinforce the surgical instrument to shift the resonance to higher frequencies, use preshaped command inputs to avoid excitation of the resonance [59], or redesign the robot to have a macro-mini actuation scheme so that fast actions are located closer to the instrument tip [76]. The plausibility of these approaches should be investigated further. However, a low bandwidth control approach circumvents not just vibration, but all issues that limit or destabilize the controller at high bandwidth.

Chapter 5

Conclusions and Future Work

This work investigated 3D ultrasound-guided robotic motion compensation as an assistive technology to intracardiac beating heart surgery. A number of engineering challenges were addressed to develop a viable system for *in vivo* experimentation: heart motion prediction to counter time delays in imaging and image processing, real-time tracking of surgical targets in noisy 3D ultrasound images, and safe force control schemes for the manipulation of tissue without exciting vibratory dynamics in the robot. Solutions were provided to these challenges in the form of a quasiperiodic extended Kalman filter (Chapter 2), a synergistic "flashlight" tracker (Chapter 3), and a force controller with feed-forward motion information (Chapter 4). Integrating these components into a system, we demonstrated that motion compensation is not only feasible, but also provides significant performance advantages in beating heart tasks. Although the focus of this work was on beating heart mitral valve annuloplasty, several general conclusions may be drawn that are not tied to a specific surgical procedure. This chapter discusses the insights provided by this thesis and elaborates

on potential directions for future research.

5.1 Conclusions

Performance Benefits. In every experiment conducted in this study, users expressed more confidence performing surgical tasks with motion compensation than without. This is not surprising given the level of performance increase conferred by motion compensation. The *in vitro* experiments of Chapters 2 and 3 show that complex tasks like path tracing and surgical anchor deployment are executed with higher accuracy, lower forces, and higher success rates by 50% or more when using a motion compensating instrument than when using a nonactuated instrument. *In vivo* experiments show that these benefits are maintained under the poor imaging and unstructured usage conditions in the operating room. Robotic position tracking accuracies of 1.0 mm and force tracking accuracies of 0.11 N were achieved in tasks performed in a porcine beating heart model using noisy, time-delayed 3D ultrasound for guidance. This constitutes a reduction in error of 70% and 75%, respectively, when compared to manual attempts at the same tasks. These experiments are the first to establish the benefits of motion compensation in an *in vivo* setting, and they highlight the potential for robotics to transform the practice of beating heart surgery. Even larger benefits are expected in the human heart, at least for mitral valve annuloplasty, because the annulus excursion is two to three times larger in humans than in the porcine model used in this work.

Synergistic, Underactuated System. The field of surgical robotics is currently dominated by the teleoperation concept of using a large, multiple degree of freedom (DOF) robot in a master-slave configuration. Previous work on motion compensation has worked in this paradigm, using multiple DOF, teleoperated manipulators to autonomously track fiducials [24] or sensors [6] affixed to the heart. As this work shows, this level of system complexity is not always necessary. Instead, designing simpler, smaller robotic systems for specific procedures could lead to better performance and remove potential problems that would occur as a result of using a general purpose manipulator.

Throughout this work it was shown that a simple, single DOF robot that is similar to a handheld endoscopic tool can be used to track and manipulate moving heart tissue. The surgeon and robot worked together in a synergistic system, with both assuming tasks that they are adept at performing. The robot provided the rapid actuation needed to account for the motion of the heart and the surgeon identified and aimed the robot toward the correct surgical site. This approach enabled the development of a relatively cheap and high performance system for mitral valve annuloplasty. Although current research trends in surgical robotics are toward general purpose, multiple DOF robots with high levels of autonomy, future work in motion compensation should evaluate the use of underactuation and semi-autonomy as a means of providing inexpensive, high performance robotic systems that cater to specific beating heart procedures.

Force Control for Manipulation. An interesting finding in this work is that a position controller is not well suited for manipulation tasks requiring precise, sustained

forces on moving cardiac structures. While it is generally accepted that force control is preferrable to position control for manipulation, this is in industrial situations where a stiff robot that is capable of exerting large torques interacts with a stiff environment. Any errors in position could lead to large forces that damage the environment. This is also a consideration in beating heart surgery, where the environment is tissue, but there is a more fundamental problem with position control in this setting: when a stiff robot contacts soft moving tissue, the target trajectory is modified. Specifically, the tissue target is displaced and undergoes less motion because of the compressive force applied by the robot. Positional tracking of the tissue during this interaction would not provide good motion compensation because the tissue location is forced by the robot.

A force controller is more appropriate during heart manipulation. However, standard force control approaches cannot safely attain the required closed-loop bandwidth to reject heart motion disturbances due to vibratory modes within the robot structure. These vibrations are a limitation even for single DOF systems driving long surgical instruments. As shown in Chapter 4, these bandwidth limitations can be overcome by incorporating feed-forward motion terms in the force control law. This enables the controller to operate at a low enough bandwidth to avoid resonances in the robot while still compensating for movements of the heart.

Heart Motion Modeling and Estimation. The key to much of the work in this thesis is that the motion of the heart is nearly periodic, and that it can be modeled as a time-varying Fourier series and estimated with an extended Kalman filter. This allows the prediction of heart motion into the near future to compensate for system latencies

that result from the use of 3D ultrasound. By adopting a modeling and estimation approach that explicitly accounts for randomness in the measurements and heart rate, this can be achieved with much higher accuracy than previously existing methods in the presence of high noise and heart rate variability. Furthermore, by virtue of using a motion model that is continuous in time, it is natural to obtain interpolations of target position from the relatively slow 3D ultrasound sampling rate (24–30 Hz) to the higher servo rate of the robot (1 kHz) and smooth estimates of target velocity and acceleration. The former is important for positional tracking of the heart with a robot, the latter is important for feed-forward force control of a robot against the heart.

Robot Guidance with 3D Ultrasound. This work demonstrates that 3D ultrasound is an effective imaging technology for the real-time guidance of a robot in motion compensated, intracardiac beating heart surgery. Previous work in robotic 3D ultrasound servoing was limited to 2 Hz [47] or suffered from a large 130 ms latency [46] due to delays in image acquisition, transfer, and processing. Such performance, while promising, is not adequate for motion compensation of the beating heart. By exploiting the periodicity of heart motion to overcome time delay, we showed that a robot can be servoed to follow moving heart structures in real-time (28 Hz) and with high accuracy. This opens up the possibility of using 3D ultrasound-guided robotics to develop new intracardiac beating heart procedures. Several potential surgical applications are covered in Section 5.2 of this chapter.

5.2   Future Directions

System Improvements.   A number of improvements can be pursued to increase the robustness, accuracy, and usability of the system developed here. First, the system could incorporate ECG to obtain a direct measure of heart rate. This would facilitate convergence and increase accuracy for the extended Kalman filter, which currently infers heart rate indirectly from target motion. Second, the system could use more sophisticated controllers. For positioning tasks, a model predictive controller or repetitive controller could remove the 0.14 mm RMS error that is incurred from using PID control (Chapter 2). Additionally, the feed-forward force control scheme in Chapter 4 assumes that the stiffness of the heart is constant and known, but it may be possible to estimate this value online [57] and allow it to vary over time [33, 34] to adjust to stiffness changes from the contraction and relaxation of the heart muscle. This would help to maximize the performance of the error feedback loop in the force controller.

Finally, user experiments suggest several shortcomings in the current robot: it is uncomfortable to use for extended periods of time due to its weight, inertial forces from its moving mass obscure haptic information to the user, and its straight end effector limits access to certain parts of the mitral valve annulus from a single entry point to the heart. Weight reduction in combination with a maneuverable support could improve the ergonomics of the instrument for prolonged use in the operating room. Moving the actuator off of the instrument or incorporating a counterbalancing mass to the instrument could restore force feedback to the user. The latter option would increase the overall mass of the instrument, though, and an analysis of overall

usability should be done to ascertain the relative benefits of each approach. To improve robot access inside the heart, the robot could be equipped with a set of interchangeable curved instruments that are shaped to reach different points on the mitral valve annulus from a single point on the left atrial appendage.

Robotic Enhancements to Surgery. In addition to compensating for fast heart motion, this work enables the development of several technologies that could ease or improve the execution of beating heart procedures. For instance, motion prediction and real-time tissue tracking could be used to render incoming 3D ultrasound volumes so that a stabilized view of the surgical site is presented to the surgeon. This approach in combination with motion compensation was shown to reduce task performance times under *in vitro* conditions with vision systems [64]. It may provide an additional accuracy benefit in 3D ultrasound-guided tasks by helping the surgeon interpret noisy 3D ultrasound images without having to mentally contend with target motion.

With the force tracking work in Chapter 4, precise but arbitrary force trajectories can now be applied to moving cardiac structures. This capability could make surgical macros – the automated execution of simple, repetitive tasks by the robot – possible on the beating heart. A simple example of this would be in surgical anchor deployment. Currently, the surgeon deploys anchors by hand after pressing the instrument against the tissue with a force of approximately 2.5 N. This task could be relegated to the robot, freeing the surgeon to focus solely on correct placement of the instrument on the anatomy. Automation could also enable more sophisticated surgical maneuvers, such as suturing, where a needle must be driven into, through, and out of tissue with a complicated force trajectory at the instrument tip.

Although the estimation and force tracking techniques presented in this thesis are described for a 1 DOF robot, they are readily extended to multiple DOF systems. Extra degrees of freedom in the robot may enhance surgical dexterity by enabling greater articulation of the instrument within the restricted space of the heart. This could be useful even for manipulating the mitral valve annulus, which has only a single DOF motion trajectory, by allowing the surgeon to approach the surgical target from a variety of incidence angles. Beating heart procedures on cardiac structures undergoing more complicated motion than the mitral valve annulus may also necessitate providing the surgeon with a multiple DOF motion compensation system.

Other Applications. Motion compensation has a number of promising applications in valve procedures other than annuloplasty. For instance, positional tracking of the mitral valve leaflets with a robot may allow the surgeon to grasp them as they move, a feat that is difficult to perform reliably by hand because of fast leaflet motion. This could enable beating heart leaflet modification procedures such as resection or edge-to-edge repair that are currently only performed on a stopped heart. Similarly, the deployment of stent-like prosthetic replacement valves is now done by rapidly pacing the ventricle in excess of 200 beats per minute to temporarily impair cardiac output and reduce valve motion while the replacement valve is correctly situated over the diseased valve. Positional synchronization of the valve delivery device with the diseased valve could enable this procedure to be done without pacing.

Motion compensation through feed-forward force tracking may also be amenable to other procedures inside and outside of the heart where there is significant and extended contact with moving tissue. Catheter ablation treatment for atrial fibril-

lation, for example, entails pressing the end of an instrument against the heart for several seconds to create an electrically inactive scar in the tissue. Beating heart coronary artery bypass graft requires handling small, delicate vessels as they are sewn to the moving heart. Additionally, the ability to apply arbitrary forces while following moving tissues raises the interesting potential of measuring the *in vivo* mechanical properties of organs with indentation testing.

Bibliography

[1] A. Afifi, V. A. Clark, and S. May. *Computer-Aided Multivariate Analysis*. Texts in Statistical Science. Chapman & Hall/CRC, 4 edition, 2004.

[2] C. An and J. Hollerbach. Dynamic stability issues in force control of manipulators. In *Proceedings of IEEE International Conference on Robotics and Automation (ICRA)*, volume 4, pages 890–896, Mar. 1987.

[3] R. Ascione, C. T. Lloyd, M. J. Underwood, A. A. Lotto, A. A. Pitsis, and G. D. Angelini. Economic outcome of off-pump coronary artery bypass surgery: a prospective randomized study. *Annals of Thoracic Surgery*, 68:2237–2242, 1999.

[4] W. Bachta, P. Renaud, L. Cuvillon, E. Laroche, A. Forgione, and J. Gangloff. Motion prediction for computer-assisted beating heart surgery. *IEEE Transactions on Biomedical Engineering*, 2009. In press.

[5] W. Bachta, P. Renaud, E. Laroche, J. Gangloff, and A. Forgione. Cardiolock: An active cardiac stabilizer. In *Proceedings of Medical Image Analysis and Computer Assisted Intervention (MICCAI)*, pages 78–85, 2007.

[6] O. Bebek and M. C. Cavusoglu. Intelligent control algorithms for robotic assisted beating heart surgery. *IEEE Transactions on Robotics*, 23(3):468–480, June 2007.

[7] A. Bokaian. Natural frequencies of beams under compressive axial loads. *Journal of Sound and Vibration*, 126(1):49–65, 1988.

[8] J. Butler, D. Parker, R. Pillai, S. Westaby, D. J. Shale, and G. M. Rocker. Effect of cardiopulmonary bypass on systemic release of neutrophil elastase and tumor necrosis factor. *Journal of Thoracic and Cardiovascular Surgery*, 105(1):25–30, 1993.

[9] B. Cagneau, N. Zemiti, D. Bellot, and G. Morel. Physiological motion compensation in robotized surgery using force feedback control. In *Proceedings of IEEE International Conference on Robotics and Automation (ICRA)*, pages 1881–1886, Apr 2007.

[10] J. W. Cannon, J. A. Stoll, I. S. Salgo, H. B. Knowles, R. D. Howe, P. E. Dupont, G. R. Marx, and P. J. del Nido. Real-time three-dimensional ultrasound for guiding surgical tasks. *Computer Aided Surgery*, 8(2):82–90, 2003.

[11] C. Chatfield. *The Analysis of Time Series: An Introduction*. Chapman and Hall, 4 edition, 1989.

[12] K. K. Chew and M. Tomizuka. Digital control of repetitive errors in disk drive systems. *IEEE Control Systems Magazine*, 10(1):16–20, 1990.

[13] E. Colgate and N. Hogan. An analysis of contact instability in terms of passive physicalequivalents. In *Proceedings of the IEEE International Conference on Robotics and Automation (ICRA)*, volume 1, pages 404–409, May 1989.

[14] B. Davies. A review of robotics in surgery. In *Proceedings of the Institution of Mechanical Engineers, Part H: Journal of Engineering in Medicine*, volume 214, pages 129–140, 2000.

[15] S. W. Downing, W. A. Herzog Jr., J. S. McLaughlin, and T. P. Gilbert. Beating-heart mitral valve surgery: Preliminary model and methodology. *Journal of Thoracic and Cardiovascular Surgery*, 123(6):1141–1146, 2002.

[16] S. D. Eppinger and W. P. Seering. On dynamic models of robot force control. In *Proceedings of the IEEE International Conference on Robotics and Automation (ICRA)*, volume 3, pages 29–34, Apr 1986.

[17] S. D. Eppinger and W. P. Seering. Understanding bandwidth limitations in robot force control. In *Proceedings of the IEEE International Conference on Robotics and Automation (ICRA)*, volume 4, pages 904–909, Mar 1987.

[18] V. Falk. Manual control and tracking – a human factor analysis relevant for beating heart surgery. *Annals of Thoracic Surgery*, 74:624–628, 2002.

[19] J. E. Felger, L. W. Nifong, and W. R. Chitwood, Jr. The evolution and early experience with robot-assisted mitral valve surgery. *Current Surgery*, 58(6):570–575, 2001.

[20] F. A. Flachskampf, S. Chandra, A. Gaddipatti, R. A. Levine, A. E. Weyman, W. Ameling, P. Hanrath, and J. D. Thomas. Analysis of shape and motion of the mitral annulus in subjects with and without cardiomyopathy by echocardiographic 3-dimensional reconstruction. *Journal of the American Society of Echocardiography*, 13(4):277–287, 2000.

[21] T. J. Franke, O. Bebek, and M. C. Cavusoglu. Improved prediction of heart motion using an adaptive filter for robot assisted beating heart surgery. In

Proceedings of IEEE Intelligent Robots and Systems (IROS), pages 509–515, San Diego, CA, USA, Oct. 2007.

[22] T. J. Franke, O. Bebek, and M. C. Cavusoglu. Prediction of heartbeat motion with a generalized adaptive filter. In *Proceedings of IEEE International Conference on Robotics and Automation (ICRA)*, pages 2916–2921, Pasadena, CA, USA, May 2008.

[23] B. Gersak. Aortic and mitral valve surgery on the beating heart is lowering cardiopulmonary bypass and aortic cross clamp time. *Heart Surgery Forum*, 5(2):182–186, 2002.

[24] R. Ginhoux, J. Gangloff, M. de Mathelin, L. Soler, M. M. A. Sanchez, and J. Marescaux. Active filtering of physiological motion in robotized surgery using predictive control. *IEEE Transactions on Robotics*, 21(1):27–79, 2005.

[25] A. Goldberger, L. Amaral, L. Glass, J. Hausdorff, P. Ivanov, R. Mark, J. Mietus, G. Moody, C.-K. Peng, and H. Stanley. PhysioBank, PhysioToolkit, and PhysioNet: Components of a new research resource for complex physiologic signals. *Circulation*, 101(23):e215–e220, 2000.

[26] J. Gorman III, K. Gupta, J. Streicher, R. Gorman, B. Jackson, M. Ratcliffe, D. Bogen, and L. E. Jr. Dynamic three-dimensional imaging of the mitral valve and left ventricle by rapid sonomicrometry array localization. *Journal of Thoracic and Cardiovascular Surgery*, 112(3):712–726, 1996.

[27] S. Hara, Y. Yamamoto, T. Omata, and M. Nakano. Repetitive control system: A new type servo system for periodic exogenous signals. *IEEE Transactions on Automatic Control*, 33(7):659–668, 1988.

[28] S. C. Ho, R. D. Hibberd, and B. L. Davies. Robot assisted knee surgery. *IEEE Engineering in Medicine and Biology Magazine*, 4(3):292–300, 1995.

[29] R. Horowitz. Learning control of robot manipulators. *Journal of Dynamic Systems, Measurement, and Control*, 115(2B):402–411, 1993.

[30] J. Huang, N. V. Vasiylev, Y. Suematsu, R. O. Cleveland, and P. E. Dupont. Imaging artifacts of medical instruments in ultrasound-guided interventions. *Journal of Ultrasound in Medicine*, 26:1303–1322, 2007.

[31] S. H. Hyun and H. H. Yoo. Dynamic modelling and stability analysis of axially oscillating cantilever beams. *Journal of Sound and Vibration*, 228(3):543–558, 1999.

[32] S. Jacobs, D. Holzhey, B. B. Kiaii, J. F. Onnasch, T. Walther, F. W. Mohr, and V. Falk. Limitations for manual and telemanipulator-assisted motion tracking – implications for endoscopic beating-heart surgery. *Annals of Thoracic Surgery*, 76:2029–2035, 2003.

[33] S. Jung, T. C. Hsia, and R. G. Bonitz. Force tracking impedance control for robot manipulators with an unknown environment: Theory, simulation, and experiment. *International Journal of Robotics Research*, 20(9):765–774, 2001.

[34] S. Jung, T. C. Hsia, and R. G. Bonitz. Force tracking impedance control of robot manipulators under unknown environment. *IEEE Transactions on Control Systems Technology*, 12(3):474–483, 2004.

[35] M. Kamigaki and N. Goldschlager. Echocardiographic analysis of mitral valve motion in atrial septal defect. *American Journal of Cardiology*, 30:343–348, 1972.

[36] C. Kempf, W. C. Messner, M. Tomizuka, and R. Horowitz. Comparison of four discrete-time repetitive control algorithms. *IEEE Control Systems Magazine*, 13(6):48–54, 1993.

[37] D. T. Kettler, R. D. Plowes, P. M. Novotny, N. V. Vasilyev, P. J. del Nido, and R. D. Howe. An active motion compensation instrument for beating heart mitral valve surgery. In *Proceedings of IEEE International Conference on Intelligent Robots and Systems (IROS)*, San Diego USA, Oct. 2007.

[38] M. Kitagawa, A. M. Okamura, B. T. Bethea, V. L. Gott, and W. A. Baumgartner. Analysis of suture manipulation forces for teleoperation with force feedback. In *Proceedings of Medical Image Computing and Computer-Assisted Intervention (MICCAI)*, pages 155–162, 2002.

[39] A. LaPietra, E. A. Grossi, C. C. Derivaux, R. M. Applebaum, C. D. Hanjis, G. H. Ribakove, A. C. Galloway, P. M. Buttenheim, B. M. Steinberg, A. T. Culliford, and S. B. Colvin. Robotic-assisted instruments enhance minimally invasive mitral valve surgery. *Annals of Thoracic Surgery*, 70:835–838, 2000.

[40] M. Lemma, A. Mangini, A. Redaelli, and F. Acocella. Do cardiac stabilizers really stabilize? experimental quantitative analysis of mechanical stabilization. *Interactive CardioVascular and Thoracic Surgery*, 4:222–226, 2005.

[41] M. J. Mack. Pro: beating-heart surgery for coronary revascularization: is it the most important development since the introduction of the heart-lung machine? *Annals of Thoracic Surgery*, 70:1774–1778, 2000.

[42] I. Mirsky and W. W. Parmley. Assessment of passive elastic stiffness for isolated heart muscle and the intact heart. *Circulation Research*, 33:233–243, 1973.

[43] J. M. Murkin, W. D. Boyd, S. Ganapathy, S. J. Adams, and R. C. Peterson. Beating heart surgery: why expect less central nervous system morbidity? *Annals of Thoracic Surgery*, 68:1498–1501, 1999.

[44] Y. Nakamura, K. Kishi, and H. Kawakami. Heartbeat synchronization for robotic cardiac surgery. In *Proceedings of IEEE International Conference on Robotics and Automation (ICRA)*, pages 2014–2019, May 2001.

[45] J. A. Noble. Ultrasound image segmentation: A survey. *IEEE Transactions on Medical Imaging*, 25(8):987–1010, 2006.

[46] P. Novotny. *Real-Time Processing of Three Dimensional Ultrasound for Intracardiac Surgery*. PhD thesis, Harvard University, 2007.

[47] P. M. Novotny, J. A. Stoll, P. E. Dupont, and R. D. Howe. Real-time 3d ultrasound-based servoing of a surgical instrument. In *Proceedings of IEEE International Conference on Robotics and Automation (ICRA)*, pages 2655–2660, 2007.

[48] P. M. Novotny, J. A. Stoll, N. V. Vasilyev, P. J. del Nido, T. E. Zickler, P. E. Dupont, and R. D. Howe. GPU based real-time instrument tracking with three-dimensional ultrasound. *Medical Image Analysis*, 11:458–464, 2007.

[49] K. Ogata. *Modern Control Engineering*. Prentice Hall, 4th edition, 2001.

[50] A. M. Okamura. Methods for haptic feedback in teleoperated robot-assisted surgery. *Industrial Robot*, 31(6):499–508, 2004.

[51] T. Ortmaier, M. Groger, D. Boehm, V. Falk, and G. Hirzinger. Motion estimation in beating heart surgery. *IEEE Transactions on Biomedical Engineering*, 52(10):1729–1740, October 2005.

[52] P. J. Parker and B. D. Anderson. Frequency tracking of nonsinusoidal periodic signals in noise. *Signal Processing*, 20:127–152, 1990.

[53] C. Riviere, R. Rader, and N. Thakor. Adaptive cancelling of physiological tremor for improved precision in microsurgery. *IEEE Transactions on Biomedical Engineering*, 45(7):839–846, 1998.

[54] G. W. Roach, M. Kanchuger, C. M. Mangano, M. Newman, N. Nussmeier, R. Wolman, A. Aggarwal, K. Marschall, S. H. Graham, C. Ley, G. Ozanne, D. T. Mangano, A. Herskowitz, V. Katseva, and R. Sears. Adverse cerebal outcomes after coronary bypass surgery. *New England Journal of Medicine*, 335(25):1857–1864, 1996.

[55] J. Rosen, B. Hannaford, M. P. MacFarlane, and M. N. Sinanan. Force controlled and teleoperated endoscopic grasper for minimally invasive surgery experimental performance evaluation. *IEEE Transactions on Biomedical Engineering*, 46(10):1212–1221, Oct 1999.

[56] J. D. Schutter. Improved force control laws for advanced tracking applications. In *Proceedings of the IEEE International Conference on Robotics and Automation*, 1988.

[57] H. Seraji and R. Colbaugh. Force tracking in impedance control. *International Journal of Robotics Research*, 16(1):97–117, 1997.

[58] B. Siciliano and L. Villani. *Robot Force Control*. Springer, 1st edition, 1999.

[59] N. C. Singer and W. P. Seering. Preshaping command inputs to reduce system vibration. *Journal of Dynamic Systems, Measurement, and Control*, 112(1):76–82, Mar. 1990.

[60] Y. Suematsu, J. F. Martinez, B. K. Wolf, G. R. Marx, J. A. Stoll, P. E. DuPont, R. D. Howe, J. K. Triedman, and P. J. del Nido. Three-dimensional echo-guided beating heart surgery without cardiopulmonary bypass: atrial septal defect closure in a swine model. *Journal of Thoracic and Cardiovascular Surgery*, 130:1348–1357, 2005.

[61] Y. Suematsu, G. Marx, J. Stoll, P. Dupont, R. Cleveland, R. Howe, J. Triedman, T. Mihaljevic, B. Mora, B. Savord, I. Salgo, and P. del Nido. Three-dimensional echocardiography-guided beating-heart surgery without cardiopulmonary bypass: A feasibility study. *Journal of Thoracic and Cardiovascular Surgery*, 128(4):571–578, 2004.

[62] A. Thakral, J. Wallace, D. Tomlin, N. Seth, and N. V. Thakor. Surgical motion adaptive robotic technology (S.M.A.R.T.): Taking the motion out of physiological motion. In *Proceedings of Medical Image Computing and Computer-Assisted Intervention (MICCAI)*, pages 317–325, Oct. 2001.

[63] S. Thorpe, D. Fize, and C. Marlot. Speed of processing in the human visual system. *Nature*, 381(6582):520–522, 1996.

[64] A. Trejos, S. Salcudean, F. Sassani, and S. Lichtenstein. On the feasibility of a moving support for surgery on the beating heart. In *Medical Image Computing and Computer-Assisted Intervention (MICCAI)*, pages 1088–1097, September 1999.

[65] N. V. Vasilyev, J. F. Martinez, F. P. Freudenthal, Y. Suematsu, G. R. Marx, and P. J. del Nido. Three-dimensional echo and videocardioscopy-guided atrial septal defect closure. *Annals of Thoracic Surgery*, 82(4):1322–1326, 2006.

[66] N. V. Vasilyev, I. Melnychenko, K. Kitahori, F. P. Freudenthal, A. Phillips, R. Kozlik-Feldmann, I. S. Salgo, P. J. del Nido, and E. A. Bacha. Beating-heart patch closure of muscular ventricular septal defects under real-time three-dimensional echocardiographic guidance: A preclinical study. *The Journal of Thoracic and Cardiovascular Surgery*, 135(3):603–609, 2008.

[67] C. R. Wagner and R. D. Howe. Mechanisms of performance enhancement with force feedback. In *Proceedings of First Joint EuroHaptics Conference and Symposium on Haptic Interfaces for Virtual Environment and Teleoperator Systems*, pages 21–29, Mar 2005.

[68] C. R. Wagner, D. P. Perrin, N. V. Vasilyev, P. J. del Nido, and R. D. Howe. Force feedback in a three-dimensional ultrasound-guided surgical task. In *Proceedings of 14th Symposium on Haptic Interfaces for Virtual Environments and Teleoperator Systems*, pages 43–48, Washington, D.C., USA, 2006. IEEE Computer Society Press.

[69] C. R. Wagner, N. Stylopoulos, P. G. Jackson, and R. D. Howe. The benefit of force feedback in surgery: Examination of blunt dissection. *Presence: Teleoperators and Virtual Environments*, 16(3):252–262, 2007.

[70] B. Wandt, L. Bojo, and B. Wranne. Influence of body size and age on mitral ring motion. *Clinical Physiology*, 17:635–646, 1997.

[71] W. Weaver, Jr., S. P. Timoshenko, and D. H. Young. *Vibration Problems in Engineering*. Wiley-Interscience, 5 edition, 1990.

[72] D. E. Whitney. Force feedback control of manipulator fine motions. *Journal of Dynamic Systems, Measurement and Control*, 99:91–97, 1977.

[73] D. J. Willams and M. Shah. A fast algorithm for active contours and curvature estimation. *Computer Vision Graphics and Image Processing: Image Understanding*, 55(1):14–26, Jan. 1992.

[74] S. G. Yuen, M. C. Yip, N. V. Vasilyev, D. P. Perrin, P. J. del Nido, and R. D. Howe. Robotic force stabilization for beating heart intracardiac surgery. In *Proceedings of Medical Image Computing and Computer-Assisted Intervention (MICCAI)*, Sept 2009.

[75] N. Zemiti, G. Morel, T. Ortmaier, and N. Bonnet. Mechatronic design of a new robot for force control in minimally invasive surgery. *IEEE/ASME Transactions on Mechatronics*, 12(2):143–153, Apr 2007.

[76] M. Zinn, O. Khatib, and B. Roth. A new actuation concept for human friendly robot design. In *Proceedings of IEEE International Conference on Robotics and Automation (ICRA)*, volume 1, pages 249–254, May 2004.